Brandenburgische Technische Universität Cottbus - Senftenberg

Brandenburg University of Technology Cottbus - Senftenberg

Faculty of Mechanical, Electrical Engineering and Industrial Engineering

Institute for Energy technology

Experimental investigation and CFD analysis of wind energy estimation considering building integrated ducts

Master thesis

To obtain the academic degree of a
Master of Science in Power Engineering (Brandenburg University of Technology) in the branch of
Sustainable Energy Supply

Submitted by: *Gazi Hasanuzzaman*
Bachelor of Science

Examiner: *Prof Dr. –Ing. Christoph Egbers*

Mentor: *Dipl. –Phys. Sebastian Merbold*
Dipl. –Ing. Emir Öngüner

BTU Cottbus-Senftenberg
Department of Aerodynamics and Fluid Mechanics

Giving out: Cottbus*, 10 August 2014*
Submission: Cottbus*, 10 December 2014*

https://doi.org/10.26127/BTUOpen-6192

Statement of authentication

The author of this paper declares that he has prepared the submitted work himself, unassisted and without using any other resources than those indicated. All the direct or indirect cited information from other sources (including the electronic sources) is duly acknowledged without exceptions. The material, in this or similar form, has not been previously submitted, either in full or in part, for other exams at this or any other academic institution.

Cottbus, 10.12.2014
place, date

Original signature

Acknowledgement

Foremost, I would like to express my sincere gratitude to my supervisor Prof. Dr. –Ing. Christoph Egbers for his invaluable support. I cannot express enough thanks to my advisors Dipl. –Phys. Sebastian Merbold and Dipl. –Ing. Emir Öngüner for their guidance, patience, motivation and enthusiasm. My completion of this thesis could not have been accomplished without the support and training of Dr.-Ing. Vasyl Motuz. Their guidance helped me in all the time of research and writing of this thesis.

I am deeply grateful to Ms Mareike Kunze from International office at Brandenburg University of Technology for the financial support. My STIBET-I scholarship provided by the Federal Foreign Office (AA) has supported me for the period of October 2014 to January 2015.

I owe my deepest gratitude to my beloved family, especially my mother Mrs Nasrin Akter, for her sleepless night in praying for my well being and success, my father Mr A.K.M. Asaduzzaman, for his unconditional love, support and advice behind every step I took since I was born till today. I solely dedicate this achievement to their contribution and everything else that I have accomplished in my life. My heartiest thanks goes to my dear and loving girlfriend Munni, whose continuous presence, inspiration and affection has given me the strength to endure my struggle when I needed it the most.

Last but not the least, my friend in need Sakeb Hasan Choudhury, my friend and mentor Bhuiyan Shameem Mahmood Ibne Hai and Kusum Barua, without them my quest of Germany would be incomplete. I would like to convey my gratitude from the deepest core of my heart to them for their help, presence and guidance.

Abstract

Wind energy is a growing concern over the present awareness of lethal impact of green house gas emission. This energy source has been proven a promising alternative to fossil fuel based energy. Increased onshore wind capacity and decreased amount of low roughness wind sites has inspired the wind energy researchers to explore the possibilities of wind energy from high roughness sites such as urban area. Moreover, exhausted grid capacity between the wind energy producer from remote area and the consumer at city is also a major constrain for wind energy expansion. Driven by such motivation, this thesis has explored possibilities of wind energy conversion from buildings where energy is needed the most. Urban topography is known to be highly turbulent region considering its roughness characteristics. Moreover, complexity of urban area requires higher understanding in terms of aerodynamics due to its difference in topography and shape. The aim of this thesis is to explore the possibility of wind energy yield from buildings and the appropriate design solution. There are several possibilities to integrate wind turbines with built structures. This study was focused on the possible wind energy yield from the building augmented duct and suitable duct design in achieving so. It specially deals with concentrator effect of rectangular building design on the augmented duct flow for an efficient duct design solution. Complex atmospheric boundary layer flow was simplified to basic aerodynamic flow along with model with four different duct geometry in the parallel flow. Three basic principles of aerodynamic research was followed to analyze the properties of these simplified qualities in parallel flow namely mathematical modelling, wind tunnel experiment and numerical analysis with a commercial CFD tool. Historical wind data was analyzed for a limited period of time based on the City region of Cottbus, Germany. The analysis has showed the influence of related site characteristics on the wind flow of this particular region and setting of the necessary topography parameters for wind data assessment for energy yield. For wind tunnel measurement, closed loop aerodynamic wind tunnel from Department of Aerodynamics and Fluid Mechanics of Brandenburg University of Technology was used. Later, Computational Fluid Dynamics (CFD) chapter describes the numerical analysis used to solve the similar flow from wind tunnel with the help of a commercial CFD solver. Results obtained from numerical flow simulation was verified by the wind tunnel results. Achieved advantages of both verification tools e.g wind tunnel measurement and CFD steps were exploited by pre-selecting the modelling tool according to the best practice guide line for an accurate result in the applied situation.

Wind energy yield from urban aerodynamics is a vast arena of experimental research. Within the time frame of the thesis period and available opportunities, a brief description about the wind energy assessment modelling approach from urban flow was outlined. There are several possibilities of wind energy yield from the built structure, but only building integrated duct was focused in this thesis. Time-averaged and global wind speed on the building integrated ducts, flow around the buildings was measured from wind tunnel and numerical analysis. Available wind

energy yield and turbulence present in the locations measured from the flow was calculated based on the wind tunnel data and summarized with the pros and cons of the particular geometry. Elliptical duct configuration was found to achieve maximum energy yield from the omnidirectional free stream flow. However, simple rectangular duct configuration was determined as most efficient and optimized considering its simplicity, financial feasibility and relative energy yield with other duct configuration. The thesis also showed that on roof configuration is also very promising for wind energy exploration from the omnidirectional free stream flow.

However, limitations of the experiment were identified in the last chapter of this thesis. Necessary recommendations were made based on available result for future development of the research approach. Scope and opportunities was mentioned. This investigation has proved that it is possible to extract limited amount of wind energy from building augmented ducts using concentrator effect of the building exterior. Thus, the thesis concluded that the wind energy yield from building augmented ducts using the concentrator effect of the building exterior is a promising renewable energy source.

Zusammenfassung

Windenergie gibt angesichts des gegenwärtigen Bewusstseins für die tödlichen Auswirkungen von Treibhausgasemissionen zunehmend Anlass zur Sorge. Die erhöhte Onshore-Windkapazität und die verringerte Anzahl von Windstandorten mit geringer Rauheit haben die Windenergieforscher dazu inspiriert, die Möglichkeiten der Windenergie von Standorten mit hoher Rauheit, wie z. B. städtischen Gebieten, zu untersuchen. Darüber hinaus ist auch die erschöpfte Netzkapazität zwischen dem Windenergieerzeuger in abgelegenen Gebieten und dem Verbraucher in der Stadt ein großes Hindernis für den Ausbau der Windenergie. Angetrieben von einer solchen Motivation hat diese Arbeit Möglichkeiten der Windenergieumwandlung von Gebäuden untersucht, in denen die Energie am meisten benötigt wird. Die städtische Topographie ist aufgrund ihrer Rauheitseigenschaften als hochturbulente Region bekannt. Darüber hinaus erfordert die Komplexität des städtischen Gebiets aufgrund seiner unterschiedlichen Topographie und Form ein besseres Verständnis in Bezug auf die Aerodynamik. Das Ziel dieser Diplomarbeit ist es, die Möglichkeit der Windenergieausbeute von Gebäuden und die geeignete Designlösung zu untersuchen.

Des Zeitrahmens der Arbeit und der verfügbaren Möglichkeiten wurde eine kurze Beschreibung des Modellierungsansatzes für die Windenergiebewertung aus dem urbanen Fluss skizziert. Es gibt mehrere Möglichkeiten der Windenergieausbeute aus der gebauten Struktur, aber in dieser Arbeit wurde nur der gebäudeintegrierte Kanal fokussiert. Die zeitlich gemittelte und globale Windgeschwindigkeit auf den gebäudeintegrierten Kanälen, die Strömung um die Gebäude herum wurde aus dem Windkanal und der numerischen Analyse gemessen. Verfügbare Windenergieerträge und vorhandene Turbulenzen an den aus der Strömung gemessenen Stellen wurden auf Basis der Windkanaldaten berechnet und mit den Vor- und Nachteilen der jeweiligen Geometrie zusammengefasst. Es wurde festgestellt, dass eine elliptische Kanalkonfiguration eine maximale Energieausbeute aus dem omnidirektionalen freien Stromfluss erzielt. Jedoch wurde eine einfache rechteckige Kanalkonfiguration als die effizienteste und optimierte unter Berücksichtigung ihrer Einfachheit, finanziellen Machbarkeit und relativen Energieausbeute mit anderen Kanalkonfigurationen bestimmt. Die Diplomarbeit zeigte auch, dass die Auf-Dach-Konfiguration auch für die Windenergieerkundung aus der omnidirektionalen freien Strömung sehr vielversprechend ist.

Notwendige Empfehlungen wurden basierend auf verfügbaren Ergebnissen für die zukünftige Entwicklung des Forschungsansatzes gegeben. Umfang und Möglichkeiten wurde genannt. Diese Untersuchung hat bewiesen, dass es möglich ist, eine begrenzte Menge an Windenergie aus gebäudegestützten Kanälen zu extrahieren, indem der Konzentratoreffekt der Gebäudehülle genutzt wird.

Table of contents Page

Final word count 21,597

List of Figures Page

List of Tables Page

List of Formula	Equation No	Page
$P = \frac{1}{2}\rho A v^3$	[Eq-1.1]	5
$\frac{\bar{u}}{u_r} = \left(\frac{Z}{Z_r}\right)^{\alpha}$	[Eq-2.1]	10
v(m/s)=0.836× $B^{3/2}$	[Eq-2.2]	11
z_0=0.5 $\frac{H \cdot S}{A_H}$	[Eq-2.3]	16
$u_{cor} = u \cdot \left(1 - R_2 \cdot R_1 \cdot (1 - P)\right)$	[Eq-2.4]	18
$R_2 = \left(1 + 0 \cdot 2\frac{x}{L}\right)^{-1}$ for $\frac{L}{x} \geq 0 \cdot 3$ and $R_2 = 2\frac{L}{x}$ for $\frac{L}{x} \leq 0 \cdot 3$	[Eq-2.5]	18
$f(u) = \frac{k}{A}\left(\frac{u}{A}\right)^{k-1} e^{-\left(\frac{u}{A}\right)^k}$	[Eq-2.6]	19
$d_f = \frac{\lambda}{2Sin(\theta/2)}$	[Eq-3.1]	25
$t = 1/f_D$	[Eq-3.2]	25
$v = d_f \cdot f_D$	[Eq-3.3]	25
Re = $\frac{\rho v \mathrm{D}}{u}$	[Eq-4.1]	36
$H_D = 2ab/a + b = 0.5454\, m$	[Eq-4.2]	36
$Ma = \frac{v}{c}$	[Eq-4.3]	36
$\lambda_{\mathrm{Tu}} = T_m/T_p = \frac{3\,s}{600s} = 0.005$	[Eq-4.4]	37
$\lambda_{\mathrm{Td}} = T_m/T_p = \frac{30\,s}{600s} = 0.05$	[Eq-4.5]	37
$\lambda_u = u_m/u_p = \lambda_l/\lambda_t$	[Eq-4.6]	38
$\overline{\mathrm{u}} = \sqrt{(\overline{\mathrm{u}}_x + \overline{\mathrm{u}}_y)}$	[Eq-4.8]	48
$u_x(t) = \overline{u}_x + u_x'(t)$ and $u_y(t) = \overline{u}_y + u_y'(t)$	[Eq-4.8]	48
I≡ $\frac{\sqrt{u'^2_x + u'^2_y}}{\bar{u}}$	[Eq-4.9]	48
$\frac{\partial u_i}{\partial x_i}$ = 0	[Eq-5.1]	67
$\frac{\partial u_i}{\partial t} + u_j \frac{\partial u_i}{\partial t} = -\frac{1}{\rho}\frac{\partial P}{\partial x_i} + \frac{\partial}{\partial x_j}(2\upsilon S_{ij})$	[Eq-5.2]	67
$S_{ij} = \frac{1}{2}(\frac{\partial u_i}{\partial x_j} + \frac{\partial u_j}{\partial x_i})$	[Eq-5.3]	67
$\frac{\partial \theta}{\partial t} + u_j \frac{\partial \theta}{\partial x_j} = \frac{1}{\rho C_p}\frac{\partial}{\partial x_j}(k\frac{\partial \theta}{\partial x_j})$	[Eq-5.4]	67

$\frac{\partial C}{\partial t} + u_j \frac{\partial C}{\partial x_j} = \frac{\partial}{\partial x_j}\left(D \frac{\partial C}{\partial x_j}\right)$	[Eq-5.5]	67
$\frac{\partial U_i}{\partial x_i} = 0$	[Eq-5.6]	68
$\frac{\partial U_i}{\partial t} + U_j \frac{\partial U_i}{\partial t} = -\frac{1}{\rho}\frac{\partial P}{\partial x_i} + \frac{\partial}{\partial x_j}\left(2\upsilon \frac{\partial U_i}{\partial t} s_{ij} - \overline{u_j' u_i'}\right)$	[Eq-5.7]	68
$S_{ij} = \frac{1}{2}\left(\frac{\partial U_i}{\partial x_j} + \frac{\partial U_j}{\partial x_i}\right)$	[Eq-5.8]	68
$\frac{\partial \Theta}{\partial t} + U_j \frac{\partial \Theta}{\partial x_j} = \frac{1}{\rho C_p}\frac{\partial}{\partial x_j}\left(k \frac{\partial \Theta}{\partial x_j} - \overline{u_j' \theta'}\right)$	[Eq-5.9]	68
$\frac{\partial \mathrm{C}}{\partial t} + U_j \frac{\partial \mathrm{C}}{\partial x_j} = \frac{\partial}{\partial x_j}\left(D \frac{\partial \mathrm{C}}{\partial x_j} - \overline{u_j' C'}\right)$	[Eq-5.10]	68
$-\overline{u_i' u_j'} = 2\nu_t S_{ij} - \frac{2}{3}\mathrm{k}\delta_{ij}$	[Eq-5.11]	68
$S_{ij} = \frac{1}{2}\left(\frac{\partial U_i}{\partial x_j} + \frac{\partial U_j}{\partial x_i}\right)$	[Eq-5.12]	68
$\mathrm{k} = \frac{1}{2}\overline{u_i' u_j'}$	[Eq-5.13]	68
$\delta_{ij} = \begin{cases} 1\, for & i = j \\ 0 for & i = j \end{cases}$	[Eq-5.14]	68
$\frac{\partial}{\partial x}(\rho k) + \frac{\partial}{\partial x_i}(\rho k u_i) = \frac{\partial}{\partial x_i}\left(\Gamma_k \frac{\partial k}{\partial x_j} + \widetilde{G_k} - Y_k + S_k\right)$	[Eq-5.15]	69
$\frac{\partial}{\partial x}(\rho \omega) + \frac{\partial}{\partial x_j}(\rho \omega u_j) = \frac{\partial}{\partial x_j}\left(\Gamma_\omega \frac{\partial \omega}{\partial x_j}\right) + G_\omega - Y_\omega + D_\omega + S_\omega$	[Eq-5.16]	69
$y^+ = \frac{\rho y u_\tau}{\mu}$	[Eq-5.17]	71
$u_\tau = \sqrt{\frac{\tau_w}{\rho}}$,	[Eq-5.18]	71
$u^+ = \frac{U_T}{u_\tau}$	[Eq-5.19]	71
$\alpha^* = \alpha_\infty^*\left(\frac{\alpha_0^* + Re_t/R_k}{1 + Re_t/R_k}\right)$	[Eq-5.20]	72
$Re_t = \frac{\rho k}{\mu \omega}$	[Eq-5.21]	72
$R_k = 6$	[Eq-5.22]	72
$\alpha_0^* = \frac{\beta_i}{3}$	[Eq-5.23]	72
$\beta_i = 0.072$	[Eq-5.24]	72
$\alpha^* = \alpha_\infty^* = 1$	[Eq-5.25]	72
$\int_S \rho \phi v.n\, dS = \int_S \Gamma\, grad\phi.n\, ds + \int_\Omega q_\phi\, d\Omega$	[Eq-5.26]	76
$TI = 0 \cdot 16(Re)^{-1/8} = 0.035\ \%$	[Eq-5.27]	80

$k=\frac{3}{2}(\bar{u}\,I)^2$ =0.047198 m^2/s^2	[Eq-5.28]	80
$\frac{\bar{\delta}}{L} \approx \frac{1}{\sqrt{Re}}$	[Eq-5.29]	80
$\omega = \frac{\sqrt{k}}{\ell C_\mu^{1/2}}$=11.3 s^{-1}	[Eq-5.31]	80
$v_2\,(z_2) = v_1(z_1)\frac{\ln\frac{z_2}{z_0}}{\ln\frac{z_1}{z_0}}$	[Eq-6.1]	94

List of Symbols

All dimensions of quantities used in this thesis are according to the System International (SI).

P	Theoretical power of the flow	(Watt)
ρ	Density of air	(kg/m^3)
v	Velocity	(m/s)
A	Cross sectional area of the duct	(m^2)
$\bar{u}$	Mean velocity at z height	(m/s)
u_r	Reference velocity at height Z_r	(m/s)
α	Empirically derived coefficient for neutral stability exponent	-
Z_r	Height of the anemometer used by the weather site	m
v	Equivalent wind speed at 10 m height above sea surface	m/s
B	Beaufort number	(Bft).
H	Height of roughness element	m
S	Cross sectional area facing the wind	m^2
A_H	Horizontal area per roughness element	m^2
R_1	Empirical parameter	(%)
R_2	Empirical parameter	-
k	Form of distribution to indicate the wind climate	-
f_0	Frequency intensity of brag cell beam	Hz
f_{shift}	Frequency intensity of brag cell beam	Hz
d_f	The fringe distance	m
f_D	Doppler frequency	Hz
U_{pos}	Velocity	m/s
U_{neg}	Velocity	m/s
f_{pos}	Signal frequency	Hz
f_{neg}	Signal frequency	Hz
f_{shift}	Frequency shift	Hz
λ_T	Temporal scale	-
λ_U	Velocity scale	-
ν	Dynamic viscosity of air	kg/m.s,
a	width of the wind tunnel test section	m
b	height of the wind tunnel test section	m
c	Speed of sound in air	m/s
λ_{U_u}	Upstream velocity scale	-
λ_{U_d}	Downstream velocity scale	-
Z_0	Aerodynamic roughness length	m
δ	Boundary layer thickness	m
$\overline{u}_x$	longitudinal component of the instantaneous velocity	m/s
$\overline{u}_y$	vertical component of the instantaneous velocity	m/s
u_x'	longitudinal component of turbulent velocity fluctuation	m/s

u_y'	vertical component of turbulent velocity fluctuation	m/s
I_x	Longitudinal component of turbulence intensity	%
I_y	Vertical component of turbulence intensity	%
U_{mean}	Mean velocity	m/s
u_i	Instantaneous velocity	m/s
x_i	Instantaneous position	-
p	Instantaneous pressure	Pa
θ	Instantaneous temperature	Celcius
t	Time	Second
ν	Molecular kinematic viscosity	m^2/s
Cp	Specific heat capacity	J/kg.K
K	thermal conductivity	W/m.K
Sij	Strain rate tensor	-
C	Instantaneous concentration	g/s
D	Molecular diffusion co-efficient	m^2/s
$-\overline{u_i'u_j'}$	Reynolds stress as function of velocity gradient	-
ν_t	Turbulent viscosity	-
S_{ij}	Mean strain rate	s^{-1}
k	turbulent kinetic energy	m^2/s^2
δ_{ij}	Kronecker delta	-
y^+	Dimensionless wall unit	-
u_τ	Friction velocity	m/s
α^*	Turbulent viscosity by co-efficient	-
ϕ	Rate of change of property within the control volume	kg/m^3
S	Surface	m^2
q_ϕ	Source or sink of ϕ	-
$\rho\phi v.n$	Convective terms of flux vector in the direction normal to control volume	
$\Gamma\, grad\phi.n$	Diffusive terms of flux vector in the direction normal to control volume	
ω	Specific dissipation rate	s^{-1}
TI	Turbulent intensity	%
ℓ	turbulence length scale	m
D_H	Hydraulic diameter of the domain	m
$v_2\,(z_2)$	Average wind velocity at height z_2	m/s
$v_1(z_1)$	Reference velocity in reference height at z_1	m/s
λ_L	Length scale	-
H	Building height	m
BR_L	Blockage ratio for length	-
BL_H	Blockage ratio for height	-
μ	Dynamic viscosity	$N\ s/m^2$

List of Abbreviations

GHG	Green House Gas
LDA	Laser Doppler Anemometry
CTA	Constant Temperature Anemometry
CFD	Computational Fluid Dynamics
CAD	Computer Aided Design
BTU	Brandenburg University of Technology
ABL	Atmospheric Boundary Layer
IEC	International Electro-technical Commission
M-0	Model-0
M-1	Model-1
M-2	Model-2
M-3	Model-3
M-4	Model-4
2D	Two dimensional
3D	Three dimensional
SST	Shear Stress Transport
RNG	Reynolds Normalization Group
AOA	Angle of Attack
BIWT	Building Integrated Wind Turbine
ESDU	Engineering Sciences Data Unit

1. Introduction

1.1. Urban wind energy

Energy remains an unresolved problem for the twenty first century. Demand is increasing and resources are being exhausted. Increased amount of power generation from fossil fuel resulting in higher Green House Gas (GHG) emission is a major concern in climate change. Adverse impact of GHG does not only deteriorate the human health but also adversely influence the water resources, ecosystems, food security and coastal systems. Several studies has showed that increased share of power generation from renewable energy sources can reduce significantly the present rate of GHG emission [1]. Moreover, finite reserve of usable fossil fuel (coal, oil, gas) price is increasing rapidly. To an extent, power production scenario is quite different for Germany where growing public opinion against nuclear power generation and subsequent phasing out of nuclear power plants by 2022 has boosted power production from coal (hard coal, lignite) and oil [2]. One of the indication of such is that more than half of Germany's electricity was generated from coal in the first half of 2013 [2]. This coal dependence has resulted in increased GHG emission in Germany and around the world. On the contrary, wind energy has immense potential in emulating the gap between growing energy demand and energy price as the cost of wind energy is free. In recent years, rapid growth in wind power capacity is observed in German power market. **Figure-1.1** indicates a steep rise in installed wind power capacity from the year of 1999-2013. Total installed capacity is classified into different color groups indicating installed offshore and onshore wind farms, wind farms for repowering (Changing low capacity turbines into large one) and offshore farms not yet connected to the grid. Total installed wind energy capacity till 31 December 2013 was 34,660 MW which is a very good indication of higher wind energy share in the total energy market [3]. However, the argument about the energy crisis still persist as wind energy is a very unreliable renewable source. Even low energy density from renewable sources (wind, solar and biomass) is a concern in determining the solution to this energy crisis. Often wind farms are installed far away from the location where electricity is required. Insufficient transmission capacity between the generator and consumer is a growing concern for wind power generation for countries such as Germany in the context of renewable energy expansion. The fact that has to be taken into account that the wind farms are located far away from the consumers where wind resource is available. Thus the concept of decentralized energy supply emerge as the solution of this exhausted grid capacity. For years decentralized energy was supplied through solar systems and biomass generation due to the criteria of easier technological availability and cheap installation process. Despite being one of the largest user of wind energy in the world, Germany requires much effort in developing the wind energy growth in the distribution level [3]. In this regard, distribution level indicate the electricity supply at the consumer level. Number of

researchers are working to find out new technologies to solve the existing problem both in the generation and transmission sector. Moreover, exhaustive focus is implied on the innovation of more efficient small wind turbines. Several kinds of wind turbine designs are available for this purpose such as a three-bladed helix shaped H-Darrieus turbine called Turby, drag driven wind turbine of Savonius type called W4-C, horizontal axis wind turbine (HAWT) type Fortis, DongQ and Rivertrade. These are all small wind turbines which can be used to extract wind energy from urban resources (Buildings). However, to obtain necessary conclusion about the suitability of such choices, exhaustive research and analysis about the wind data of the region has to be conducted [3].

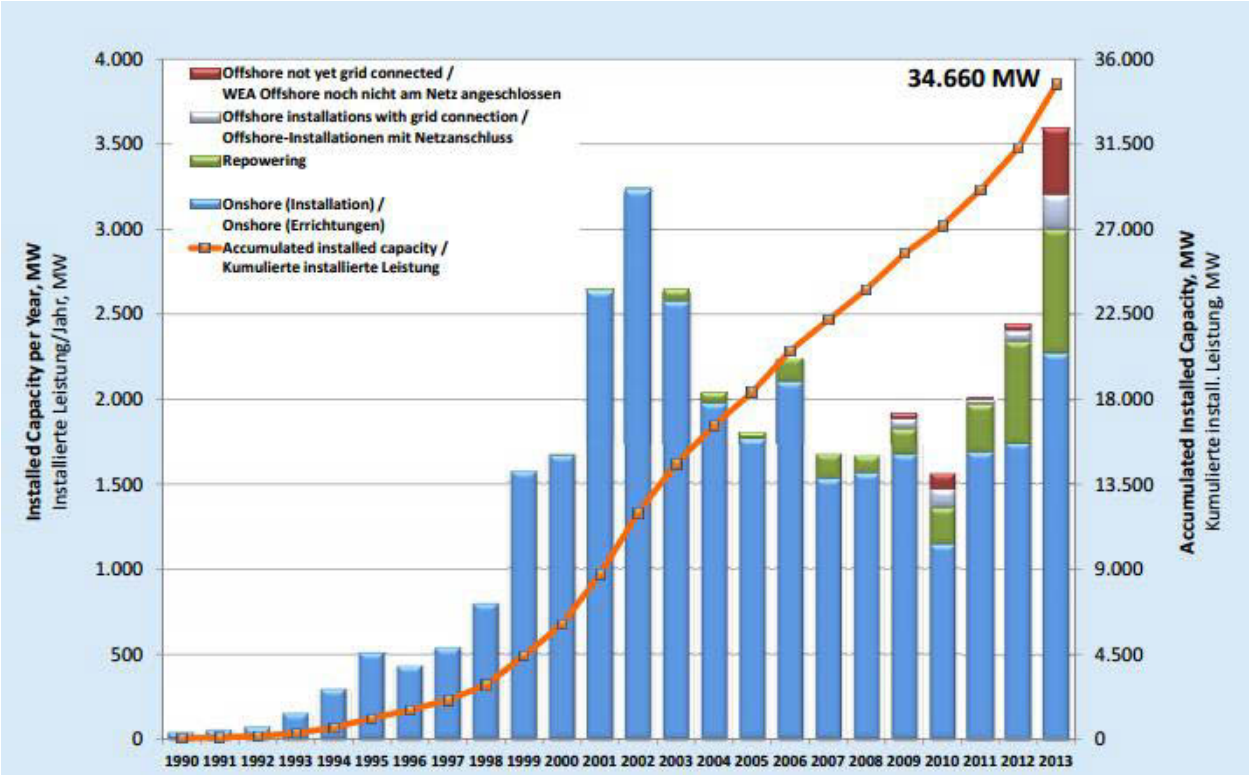

Figure-1.1. Development of the yearly and accumulated installed wind power capacity in Germany. Source: [3].

According to Dondi et al (2002) distributed generation can be defined as a generator with small capacity close to its load that is not part of a centralized generation system [4]. No energy source is cheaper then the energy from wind. Beside electricity demand for industrial use, buildings remain one of the largest consumer of the electricity. From the statistical representation of data from German Federal Ministry for Internal Affairs and Energy (**Figure-1.2**), buildings consume 28.9% of the total energy supply [5].

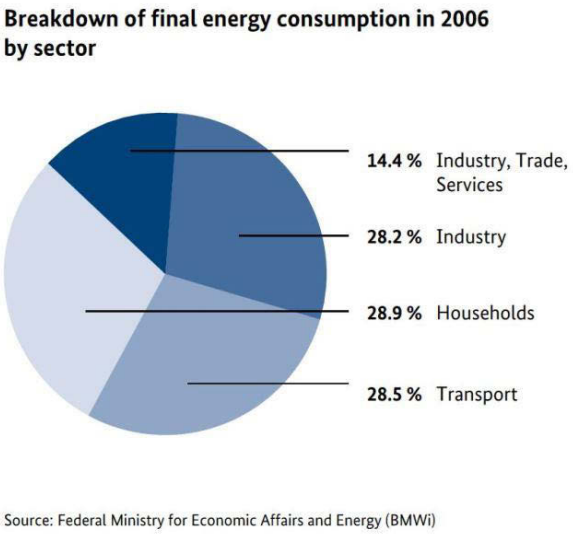

Figure-1.2. Energy consumption from building oriented consumer. Source: [4].

The building sector energy consumption can be classified into several requirements such as space heating, water heating, cooking, air conditioning, computers, electronics and lighting. Energy requirement for different purposes in percentile is illustrated in **Figure-1.3** [5].

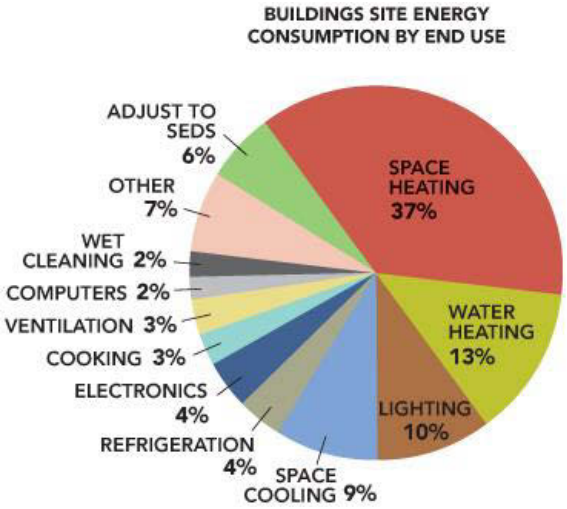

Figure-1.3. Building energy consumption for different purposes at end user. Source: [4].

It is a cheaper option to utilize the buildings to act as a concentrator of the wind flow which can magnify the flow velocity. Buildings can be used as an alternative to the expensive full size tower required to install for wind turbines. The modified architecture, even to some extent the existing building shapes have concentrator effect to the flow. Some examples of such utilization of modified building structure can be found from **Figure-1.4** [6].

Figure-1.4. Left-Right: Bahrain World Trade Center (Bahrain),The Castle (UK), Pearl River Tower (China), The Cor (USA). Source: [6].

1.2. Research methodology

The intention of this research is not only driven by the positive environmental concern of the wind energy but also the present trend to expand the decentralized power supply integrated with buildings. Researches showed that [6] wind energy in built environment was proven effective with a potential wind speed analysis for a certain region. This is one of the possible source of energy from buildings. However, the question remains for the possibility of exploring the energy from the wind. Urban terrain has higher roughness factor then the plain land or water surface (Offshore). Even in the same urban area, terrain varies to its topography from place to place. Different urban topography has different impact on the wind flow. Thus, it is necessary to obtain wind impact information on the basis of individual urban terrain where the wind energy to be explored.

Wind energy extraction from building is very area specific. According to researches [6], potential locations of the building was classified into three different locations e.g.

- Close to the sharp edges of the building
- Roof of the building
- Duct through the building (Building integrated duct)

In this research possibilities of building integrated ducts for wind energy resource was explored by the means of experimental methods. Existing building characterization was ascertained for 10 storey rectangular shaped buildings. The building models were manufactured with different duct geometries. Details of the building modeling approximation were discussed in Chapter-4. For experimental data, wind flow data of the varying impact of different duct geometries were obtained both through wind tunnel experiment and partly from computational fluid mechanics. The research question which was subjected to this thesis was possibility of wind energy extraction from building integrated duct. If possible which geometry of the building integrated duct is best suitable for wind energy exploration. The limitation imposed to this research are as follows.

- Models are single building models of conventional shape (rectangular) in the aerodynamic wind flow (Chapter-4).
- Angle of attack at 0˚ for wind flow to the duct axis.
- Wind flow velocity at 5 m/s.
- Duct geometry was confined within 4 different shapes (Chapter-4, model geometry).

Theoretically available wind power or the extractable energy from the wind flow is obtained from the following equation.

$$P = \frac{1}{2}\rho A v^3 \qquad \text{[Eq-1.1]}$$

where, P is the theoretical power of the flow (Watt), ρ is the density of air (kg/m^3), v is the velocity obtained from the flow (m/s), A is the cross sectional area of the duct (m^2). Thus, a slight variation in the flow velocity can alter the energy yield significantly. Through out this research, necessary data obtaining and analysis was conducted on the basis of flow velocity and turbulence present in the flow for different models.

Experimental methodology used for this research was divided into three main task. Urban terrain of the city of Cottbus was decided as the target region for wind energy exploration. At the first level, A range of wind data for a limited period was collected in this regard. The data include the velocity and related angle of the wind flow in a measuring site inside the city. This data string was analyzed following the wind resource data assessment procedure and the analysis was represented graphically. Second task was to determine an optimized velocity and angle for the wind tunnel test. However, wind tunnel testing is a complex measurement technique. The data measurement at the wind tunnel was limited to a certain angle of attack (0˚) for the wind flow and a specific velocity range (5 m/s). Target location of the data measurement positions around the model was selected based on the concept that results can be compared to ascertain the best duct geometry. According to the **Equation-1.1**, target variable for the experiment is velocity. Velocity with its longitudinal and vertical components were measured with Laser Doppler Anemometry (LDA) measurement technique. Velocity profile and turbulence intensity based on longitudinal and vertical component along the measuring positions was generated and graphically represented. Obtained velocity data from wind tunnel was used to calculate theoretical wind power available at ducts. Results were used to identify the best possible duct geometry. Third task is the modeling of flow with the help of numerical method. To do so, a commercial CFD solver was used. After necessary consultation through scientific journals for best practice guidelines in the field of numerical analysis of building aerodynamics, CFD modeling was designed. CFD modeling was performed following three different steps. These steps can be described as follows.

- Scaling and drawing of CAD geometry.
- Grid generation and obtaining a mesh independent solution
- Solving the fluid domain with numerical solver.

Details of the numerical technique is described in Chapter-5 of this paper. Similar velocity data was recorded at the same location as the wind tunnel measurement and graphically represented afterwards. Complete flow field data can be obtained from CFD simulation. Nevertheless, reliability of the wind tunnel data can not be ignored compared to the CFD data. Necessary validation and verification was made to determine the authenticity of the numerically simulated data.

2. Historical Wind Record Analysis

In this chapter, some descriptions about how to analyze the historical wind data record are discussed which illustrate the period of the wind data recorded, location of the data measuring site and how the data was interpreted, specifically for the city of Cottbus. This chapter also includes the theory of wind record analysis, transformation of that data into necessary information to be used in exploiting urban wind energy and finally, theory of topographical characteristics.

2.1. Wind velocity data source

Wind velocity and direction data was recorded at the CEBRA Research Centre, which is a research institute affiliated to the Brandenburg Technical University (BTU), Cottbus. Before proceeding towards data analysis, some informations about the measuring site is important to be discussed. Cottbus is a East German city located 125 km Southwest of Berlin [8]. Exact latitude and longitude of the city is 51˚45'27" and 14˚19'43" respectively. Cottbus has approximately 164.3 km^2 area [8]. Elevation of this city from sea level is 80 m [9]. Location of the wind data measuring site can be identified from the **Figure-2.1** [10].

Figure-2.1. Location of the measuring site Cottbus, Germany. Source: [10].

The data included mean velocity of the wind, averaged for ten minutes duration taken at ten meters height [11]. Wind direction was measured considering North 0˚, East 90˚, South 180˚ and West 270˚ based on the averaged value for one hour. Duration of the data record time range between first of January 2012 till thirty first of December 2012. The data from the above mentioned source provide the wind speed and direction to the nearest 0.1 m/s and 1˚ respectively. A total of 52,705 data was analysed for this experiment.

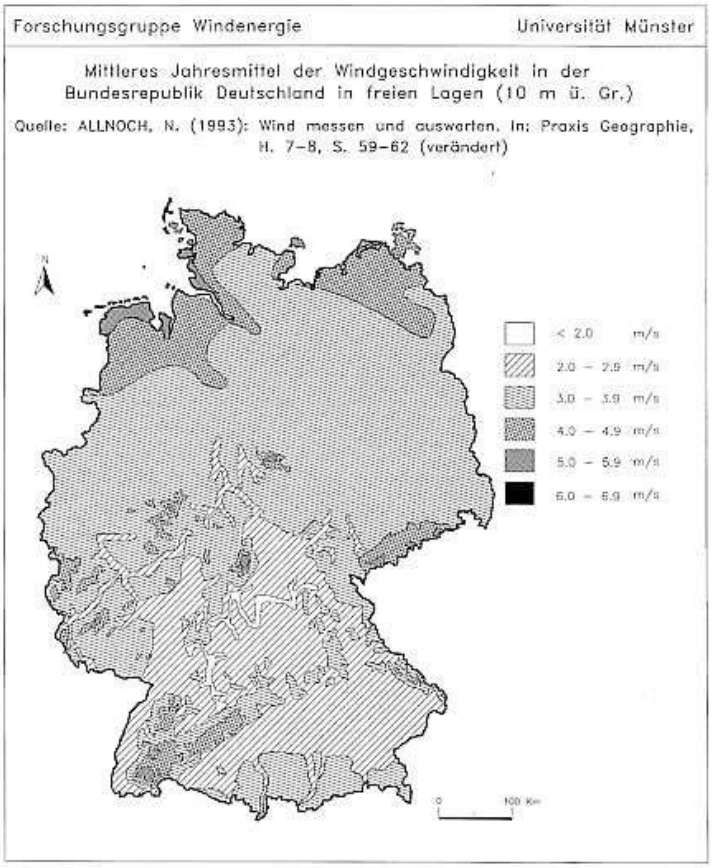

Figure-2.2. Average wind velocity of Germany. Source: [12].

According to **Figure-2.2**, average wind velocity obtained for this region varies from 3 m/s to 3.9 m/s [12]. This data was validated with the annual average wind velocity for the year of 2012 [11] and the obtained annual average velocity obtained from the data source is 3.488 m/s. This average wind velocity for the year of 2012 in the city terrain of Cottbus remain within the range of 3.0-3.9 m/s (From **Figure-2.2**). However, wind velocity varies from time to time which require updated data to analyze the trend. Necessity to analyze updated data is a prime requirement in the research of wind energy from urban environment [13]. As introduced above, the wind data used in this experiment was obtained from sites inside the city suburb of Cottbus [11]. Since wind is affected by nearby local obstacles, the environment close to the weather site and anemometers which was used to measure the wind data should be considered. The method about transformation of the wind data is discussed in the Section-2.2 of this chapter. The result

from the experiment is compared with power-law and gives some characteristic parameters for the atmospheric boundary layer around the models in wind tunnel (Chapter-4, section-4.9).

2.2. Atmospheric Boundary Layer

Atmospheric boundary layer is the lowest part of the atmosphere and behaviour is directly influenced by the Earths' Surface. The depth of the boundary layer ranges from a few hundred meters to several kilometres depending upon wind turbulence, terrain roughness and angle of latitude [20]. In 5 km height in undisturbed layer of geostropic wind there, there is no influence of roughness. Between these layers increases the wind velocity in height. Wind energy is a concern within the boundary of this atmospheric boundary layer. Different levels of turbulence can be visualized from the **Figure-2.3**.

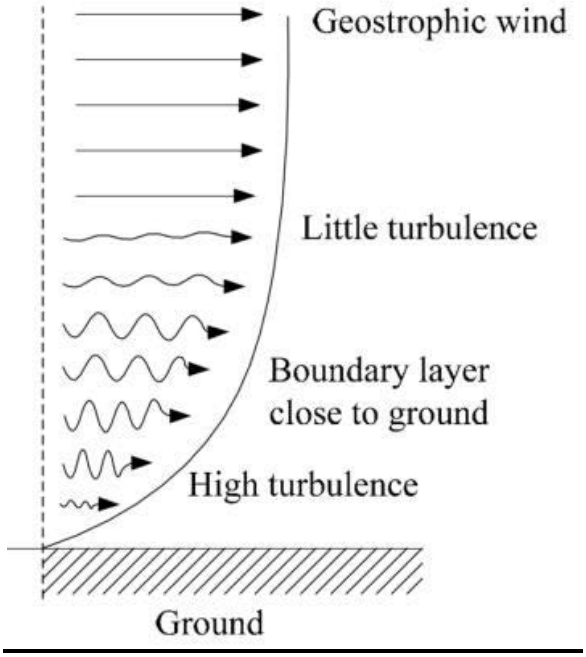

Figure-2.3. Different layers in atmospheric boundary layer. Source: [15]

2.3. Transformation of wind record

In order to estimate the wind energy available at certain terrain location, the historical wind record of the location (In this case Cottbus, Germany) is needed. Wind data for this location was obtained for one year duration as mentioned above [11]. This chapter includes the transformation of the wind data into usable parameters in wind engineering such as Weibull distribution (Section-2.5), hourly mean wind speed and wind rose (Section-2.6). Transformation of the wind record was done in two parts [13], one consists of the wind velocity data and another concerns with the direction of the wind.

2.3.1. Transformation of wind velocity

In the first step, the wind velocity record is extended to a gradient height. This gradient height might be different for different atmosphere stabilities. In urban areas turbulence has significant variation 140 m height from the ground [14]. On the other hand, some literatures have suggested a turbulent urban boundary layer which can vertically stretch up to 2 to 5H of gradient height, where H is the urban canopy layer (**Figure-2.4**) [15]. In that case the maximum variation of the turbulence is approximated from 60 m – 150 m height for buildings group of 30 m. This gradient height differs according to different roughness class. However, wind velocity conversion of the site is extended up to the height of 30 m as target building groups for this experiments were 30 m high. As mentioned before that the wind data was recorded at 10 m gradient height, there are two different methods for the conversion of this data into the velocity data at 30 m gradient height. This methods are the power law proposed by Deaves and Harris [16] and logarithmic law proposed by Ote [17]. For the boundary layer height below 150 m from the ground, log-law function shows better results for urban region [13]. On the contrary, power-law can predict more accurately the boundary layer profile for height more then 150 m from the ground [19].

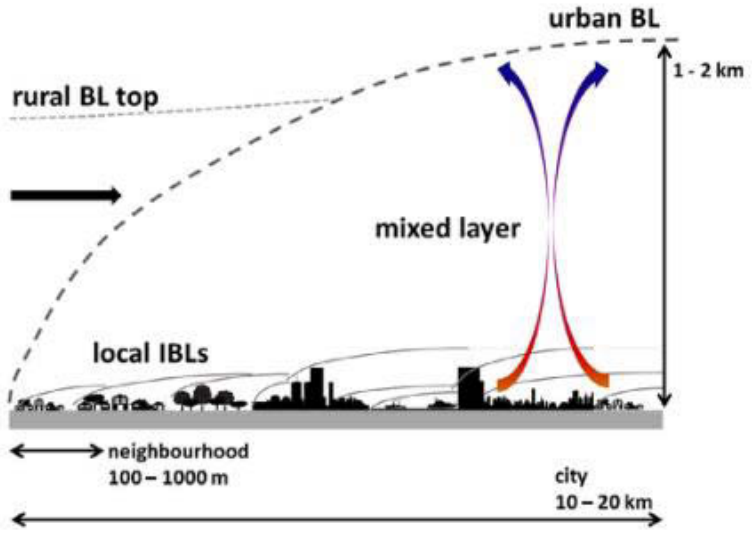

Figure-2.4. Schematic diagram of daytime convective urban boundary layer with wind flowing from left to right. Dashed lines indicate top of rural and urban boundary layers; solid lines indicate local internal boundary layers. Approximate order of magnitude is given by, e.g., 100–1000 m. Source: [15]

Power-law can be described from the **Equation-2.1**

$$\frac{\bar{u}}{u_r} = \left(\frac{Z}{Z_r}\right)^{\alpha} \quad \text{[Eq-2.1]}$$

Where, $\bar{u}$ is the mean velocity at z height, u_r is the reference velocity at height Z_r, α is the empirically derived coefficient for neutral stability exponent, Z_r is the height of the anemometer used by the weather site (In this case 10 m from the ground). The exponent value of the power-law, α is different for different roughness levels, and the relationship between roughness and α could be obtained from ESDU 72026 [18]. In this research the value of α was taken as 0.14. These velocity results are used to determine the velocity range applied in the wind tunnel experiment (see Chapter-4).

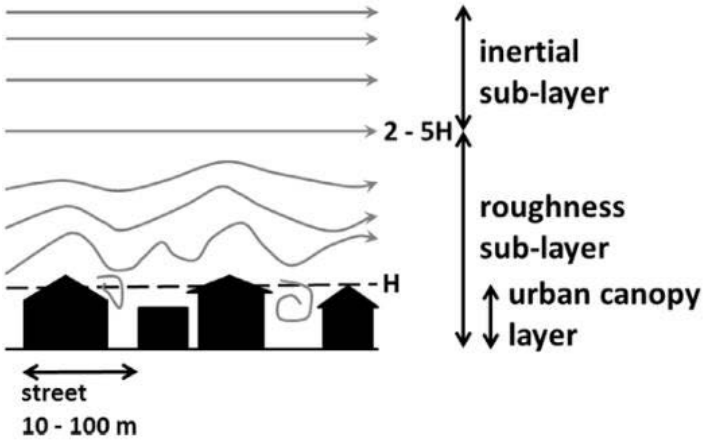

Figure-2.5. Schematic diagram of roughness and inertial sub-layers. Grey arrows indicate streamlines. Dashed line indicates mean building height (H). Source: [15]

Another scale used to describe the wind velocity class is the Beaufort scale. The Beaufort scale is an empirical measure that relates wind speed to observed conditions at sea or on land. Its full name is the Beaufort wind force scale, although it is a measure of wind speed and not of force in the scientific sense [21]. This scale was created in 1805 by Sir Francis Beaufort. The initial scale of thirteen classes (zero to twelve) did not reference wind speed numbers but related qualitative wind conditions effects on the conditions on land and sea [21]. Wind speed on the Beaufort scale is based on the empirical formula which is given as **Equation-2.2** [21]:

$$v = 0.836 \times B^{3/2} \quad \text{[Eq-2.2]}$$

Where v is the equivalent wind speed (in m/s) at 10 m height above sea surface and B is the Beaufort number (Bft). According to the **Equation-2.2** and **Figure-2.6**, wind velocity used in this research for wind tunnel experiment (5 m/s) is classified accordingly which fall into the wind speed class of 3 Bft [28].

There is another wind speed classification, known as IEC wind scale for the classification of wind farm locations. This is more frequently used in wind energy industry then the Beaufort

scale. IEC wind scale is reciprocal to Beaufort where low number means high wind velocity. They are mainly defined by the average annual wind speed measured at the turbines hub height, the speed of extreme gusts that could occur over 50 years, and how much turbulence there is at the wind site. The three wind classes for wind turbines are defined by an International Electro-technical Commission standard (IEC), and correspond to high, medium and low wind [24]. This scale [26] (**Figure-2.7**) will be very useful in the further research in this project with the energy obtained from the duct integrated wind turbine.

BEAUFORT SCALE

Force		Anemometer reading mph	kmh	m/s	knts	Description	
0		0-1	<1	<0.3	0-1	Calm; smoke rises vertically.	Calm
1		1-3	1-5	0.3-1.5	1-3	Direction of wind shown by smoke drift, but not by wind vane.	Light air
2		4-7	6-11	1.5-3.3	4-6	Wind felt on face; leaves rustle; ordinary vanes moved.	Light Breeze
3		8-12	12-19	3.3-5.5	7-10	Leaves and small twigs in constant motion; wind extends light flag.	Gentle Breeze
4		13-18	20-28	5.5-8.0	11-16	Raises dust and loose paper; small branches are moved.	Moderate Breeze
5		19-24	29-38	8.0-10.8	17-21	Small trees in leaf begin to sway; crested wavelets form on inland waters.	Fresh Breeze
6		25-31	39-49	10.8-13.9	22-27	Large branches in motion; whistling heard in telegraph.	Strong Breeze
7		32-38	50-61	13.9-17.2	28-33	Whole trees in motion; inconvenience felt when walking.	Near Gale
8		39-46	62-74	17.2-20.7	34-40	Breaks twigs off trees; generally impedes progress.	Gale
9		47-54	75-88	20.7-24.5	41-47	Slight structural damage occurs (chimney-pots and slates removed).	Severe Gale
10		55-63	89-102	24.5-28.4	48-55	Seldom experienced inland; trees uprooted; considerable structural damage occurs.	Storm
11		64-72	103-117	28.4-32.6	56-63	Very rarely experienced; accompanied by wide-spread damage.	Violent Storm
12		73-83	≥118	≥32.6	64-71		Hurricane

Figure-2.6. Wind speed classification in Beaufort scale. Source: [2].

IEC Wind Turbine Classes								
Wind Speed Parameters for Wind Turbine Classes								
	I		II	III	IV			
Reference Wind Speed, U_{ref} (m/s)	50		42.5	37.5	30			
Annual Average Wind Speed U_{ave} (m/s)	10		8.5	7.5	6			
50-year Return Gust Speed, 1.4 U_{ref} (m/s)	70		59.5	52.5	42			
1-year Return Gust Speed, 1.05 U_{ref} (m/s)	52.5		44.6	39.4	31.5			
Notes: 10-minute averages, hub height wind speed. Air density: 1.225 kg/m3.								
Turbulence Intensity Classes	I		II		III		III	IV
	A	B	A	B	A	B	A	B
I_{15} (Turbulence Intensity at 15 m/s)	18%	16%	18%	16%	18%	16%	18%	16%
a	2	3	2	3	2	3	2	3
I_u (Turbulence Intensity)	0.210	0.180	0.226	0.191	0.240	0.200	0.270	0.220
I_u (Turbulence Intensity) = $I_{15}(a=15/U_{ave})/(a+1)$								
Source: IEC 61400-1; cited in Wind Energy Handbook, Tony Burton, et al, John Wiley & Sons UK), 2001, ISBN: 0-471-48997-2, p. 210.								
Caution: Verify with current IEC 61400-1 for all parameters and criteria.								

Table-2.1. IEC wind turbine class. Source: [25].

2.3.2. Transformation of wind direction

Direction of wind is an important parameter in analysing the wind data. Different topographical location has different direction of wind throughout the year. Wind flow directions which have more frequency of high velocity of wind flow, is considered important particularly for the extraction of the wind energy. Different regions exhibit different frequency of high velocity windfall. It is a trend in local architectural practice in urban design to maintain orientation of the living space in medium height building (<30 m height and low height building >10 m) to construct the buildings facing towards the wind direction where maximum wind flow frequency is obtained. This is done to maintain the maximum natural ventilation. Analysed wind data in this research was measured with the average angle of wind direction for 10 minutes considering flow from North as 0˚, East as 90˚, South 180˚ and West as 270˚. Direction of the wind for the region of Cottbus will be discussed later with the help of wind rose diagram.

2.3.3. Monthly average wind speed for the year 2012

The wind at a given site usually varies frequently in direction and its speed may change rapidly under gusting conditions. Recorded wind speed data are generally available in time series format. Each data recording represents an instantaneous wind speed and typical representative example of the result is provided by **Figure-2.7** An average of the 10 minute wind speed pattern can be derived from these records. The monthly average wind speed distribution exhibits seasonal trends with similar behaviour for the site studied. Wind speed data for the year of 2012 was averaged for each month. This data is represented in the **Figure-2.8.** The trend indicates higher average wind speed during winter of 2012. This data does not represent the qualitative wind energy scenario but the quantitative wind speed assessment for the whole year of the 2012. To asses the wind energy, wind energy probability distribution is the qualitative representation.

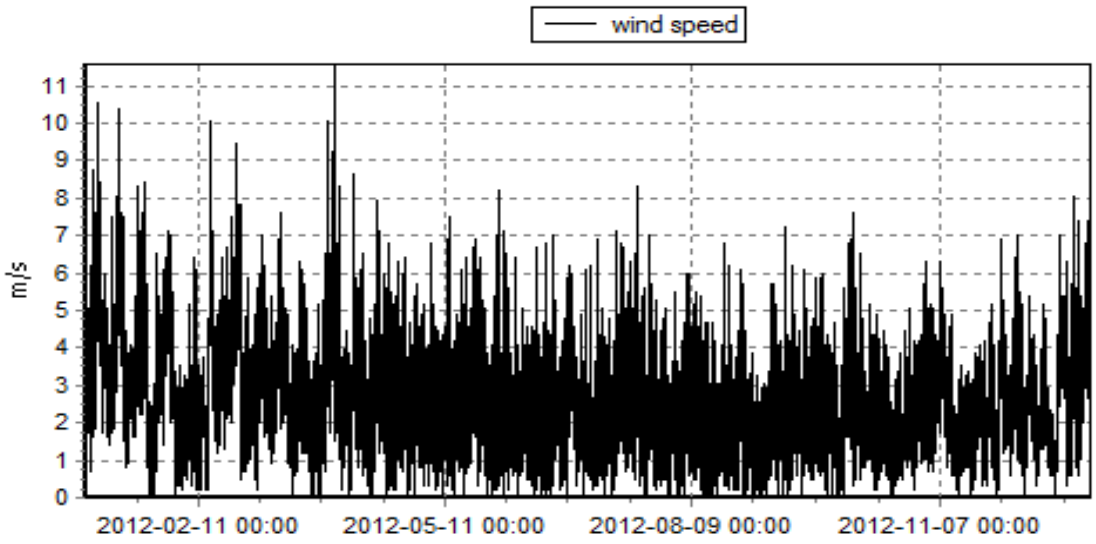

Figure-2.7. 10 minutes Average wind speed at 10m height for the year of 2012 at Cottbus. Source: own representation from the data [11].

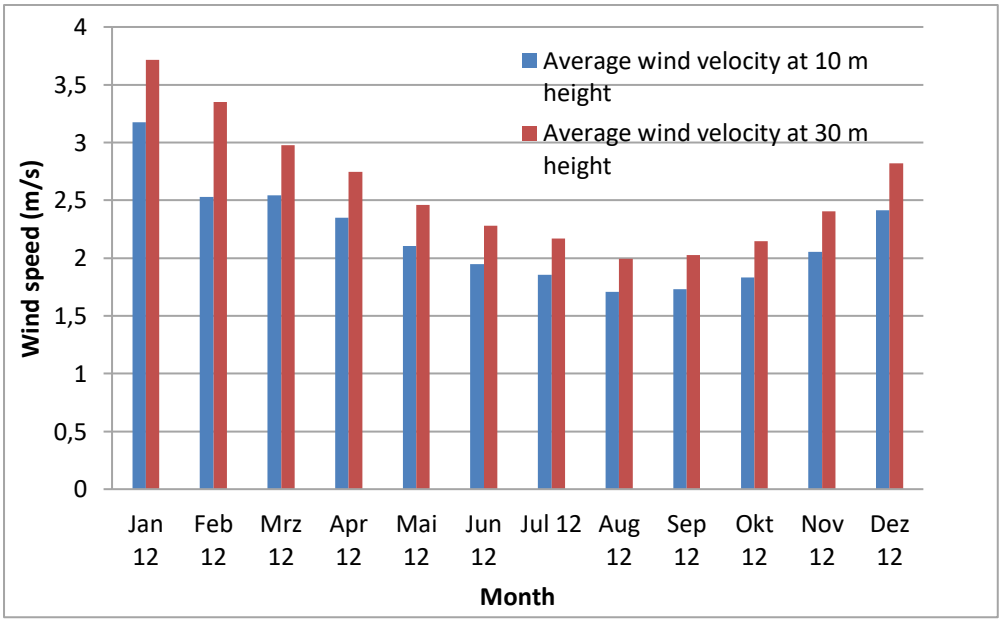

Figure-2.8. Variation of the monthly average wind speed at 10 m and 30 m height for the year of 2012 at the site CEBRA Research Centre, Cottbus. Source: own representation.

2.4. Topographical characteristic

There are 3 main topographical characteristics that influences the wind flow namely roughness, porosity, shelter and orography [23]. In estimating wind energy resource, these parameters

posses significant importance in describing the topographical characteristics. These parameters will be used for further analysis in wind power generation from urban environment. For each of these topographical impact on the urban flow, there is one or more parameters to show the level of the impact on the wind flow [13].

2.4.1. Roughness

Obstacles have a great influence to the wind. Woods, natural cover and Buildings reduce the velocity of the wind. Water and flat terrain have only small influence to the flow. Roughness is used for description of these influences. Size and frequency of wind speed distribution affect the roughness. Tall buildings with considerably higher density in suburbs and city centre slowed down the wind flow over the area. A length scale is used to describe the roughness class of the topography namely " roughness length(z_0)" [28].

$$z_0 = 0.5 \frac{H \cdot S}{A_H} \qquad \text{[Eq-2.3]}$$

Where, H is the height of roughness element, S is the cross sectional area facing the wind and A_H is the horizontal area per roughness element.

According to **Table-2.2.** roughness class 3.488 [28] is applicable to the corresponding flow (5 m/s) of this research which has a Roughness length of 0.55 m (**Equation-2.3**).

Roughness classes	Roughness length z_0[m]	Energy index (%)	Types of surfaces
0	0.0002	100	Water areas: lakes and sea
0.5	0.002	73	Open plain with clean surface
1.0	0.03	52	Open agricultural plain similar buildings
1.5	0.055	45	Agricultural plain with similar buildings and hedges of 8 m height in a distance of more than 1 km
2.0	0.1	39	Agricultural plain with similar buildings and hedges of 8 m height in a distance of more than 500 m
2.5	0.2	31	Agricultural plain with many buildings and hedges of 8 m height in a distance of 250m
3.0	0.4	24	Villages small towns, Agricultural plain with similar buildings and high hedges, woods very rough and bumpy terrain.
3.5	0.6	18	Larger cities with high buildings
4	1.6	13	Major cities with sky scrapers

Table-2.2. Roughness class for different terrain surface. Source: [27]

2.4.2. Porosity

The porosity of the obstacle is a topographical characteristics which shows how dense the windbreaks are [13]. The setting of this parameter could be changed with the class of the windbreaks, i.e. building could be set equal to 0 and trees could be set as 0.5, while for a house row with space between them of one third the length of a building is set as 0.33. Table 2-3 shows the setting of this parameter for different appearances [13].

Appearance	Porosity of the obstacle
Solid (Wall)	0
Very dense	≦0.35
Dense	0.35-0.50
Open	0.50-1.00

Table-2.3. Setting of obstacle porosity. Source: [23]

2.4.3. Shelter

The area behind the obstacles like building, trees or else with different porosity, the velocity of the wind is reduced. This relative effect of different type of obstacles on the flow velocity reduction is expressed as the shelter [29]. Various factors determine the shelter impact on the flow velocity such as distance from the obstacle to the site, the height of the obstacle, the height of the point at the measuring site, the length of the obstacle and the porosity of the obstacle (Chapter-2,section-2.4.2). Factors effecting relationship between obstacle and site can be comprehended from the **Figure-2.9** [13] .

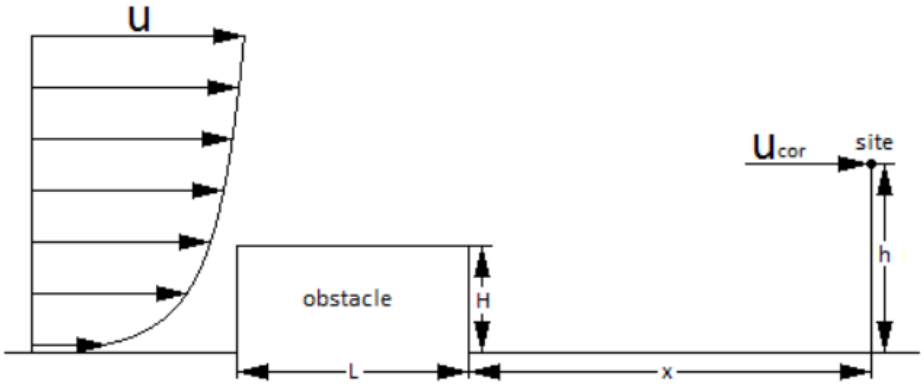

Figure-2.9. Effecting factors between obstacle and the site. Source: [13].

From **Figure-2.9**, x is the distance from the obstacle to the site, H is the height of the obstacle, h is the height of the point at the site (in this case 10 m), L is the length of the obstacle and u_{cor} is the mean wind velocity at the site which is affected by the shelter.

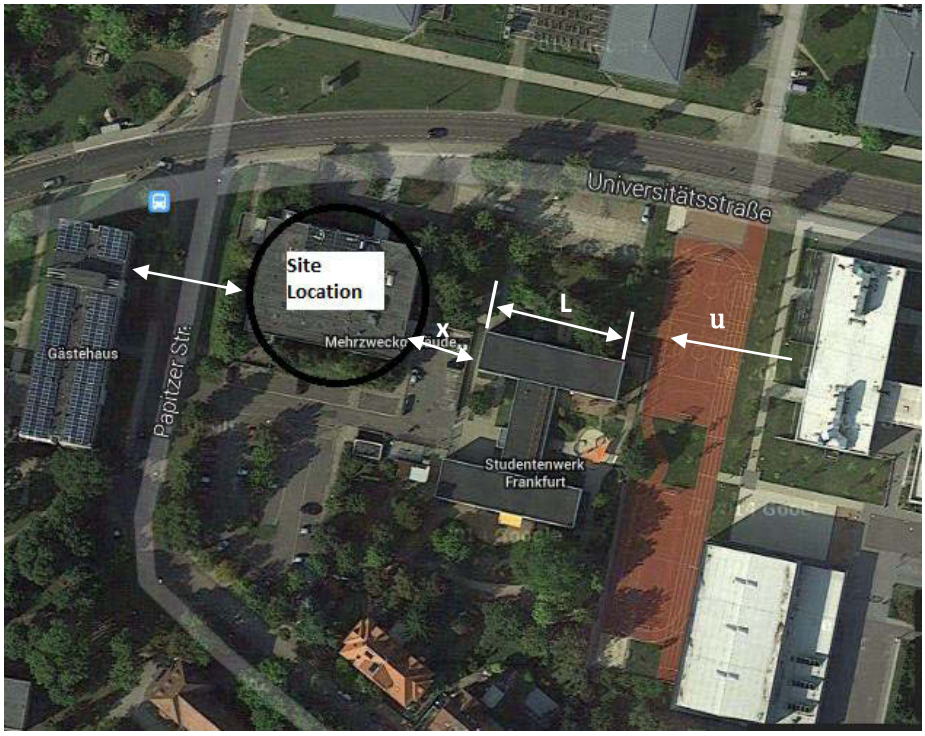

Figure-2.10. Location of the measuring site from the nearest obstacles (measuring site, Cottbus). Source: based on [10]

Figure-2.10 represent the location of the measuring site at Cottbus and the comparative distance from the nearest shelter for the flow from the west. Mean wind velocity at the site.

Mean wind velocity at the measuring site effected by the nearest shelter (u_{cor}) can be calculated from the **Equation-2.4** [29].

$$u_{cor}=u\cdot\left(1-R_2\cdot R_1\cdot(1-P)\right) \quad \text{[Eq-2.4]}$$

Where, R_1 and R_2 are two empirical parameters obtained from the location of the site from the obstacle [29]. R_1 is expressed in percentage which can be obtained from **Figure-2.11**. R_2 is obtained by **Equation-2.5** [29].

$$R_2=\left(1+0\cdot 2\frac{x}{L}\right)^{-1} for\ \frac{L}{x}\geq 0\cdot 3 \text{ and } R_2=2\frac{L}{x}\ for\ \frac{L}{x}\leq 0\cdot 3 \quad \text{[Eq-2.5]}$$

For example, in this experiment, at mean wind velocity, u=5 m/s, R_1~95% approximately (**Figure-2.11**), R_2=0.89 (**Equation-2.5**, where $\frac{L}{x}>0\cdot 3$) and P=0 (Table-2.3). Calculated u_{cor} will be 0.77 m/s for the measuring site (Approximate measurement of the relative shelter parameters from the upstream flow from west, **Figure-2.9** and **Figure-2.10**). Nearest obstacle to the measuring site will record u_{cor}≈0.77 m/s for a corresponding free stream velocity (u) value of 5 m/s from west (270˚) at 30 m height for the roughness class of 3.488 (Section-2.4.1) with an obstacle porosity (P) value of zero.

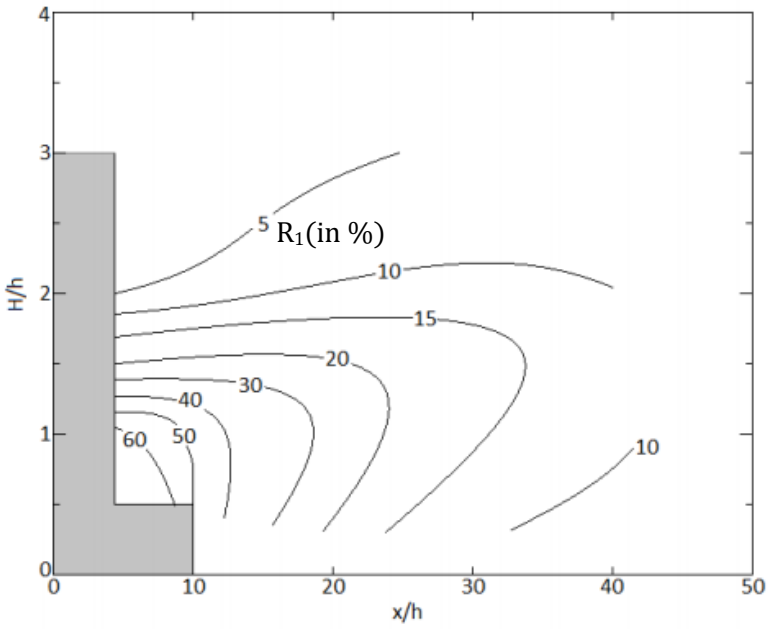

Figure-2.11. Empirical parameter (R_1) for near obstacle site position. Source: [29].

2.4.4. Orography

Orography is a topographical characteristic which can be defined as the topographical impact on the wind flow due to the landform around the site e.g hills, cliffs etc. In this experiment this topographical characteristic was not considered [30].

2.5. Weibull Distribution

Weibull distribution expresses how often the wind blows how strongly. The energy contained in the wind at the site can be expressed with the Weibull Distribution. For further measurement of the wind energy potential at the site, Weibull parameters will be necessary. At 30 m height, converted mean wind velocity data with a 10 minute interval at the site is statistically analysed. Then the wind speed data is classified into wind speed class of 0.5 m/s variation. The frequency of the annual hourly mean wind velocity are distributed according to the Weibull distribution [31]. The frequency of the wind velocity u follows the following **Equation-2.6** [31].

$$f(u)=\frac{k}{A}\left(\frac{u}{A}\right)^{k-1} e^{-\left(\frac{u}{A}\right)^{k}} \qquad \text{[Eq-2.6]}$$

Where, k describe the form of distribution and indicate the wind climate (in central Europe k≈2) [23], A indicate the characteristic wind speed of the time series which is proportional to mean wind speed and u represent the average wind speed of the wind class. Weibull distribution curve with the value of k≈2 is known as “Rayleigh distribution” [23]. This is a very common way to describe the frequency of the wind speed (**Figure-2.12**).

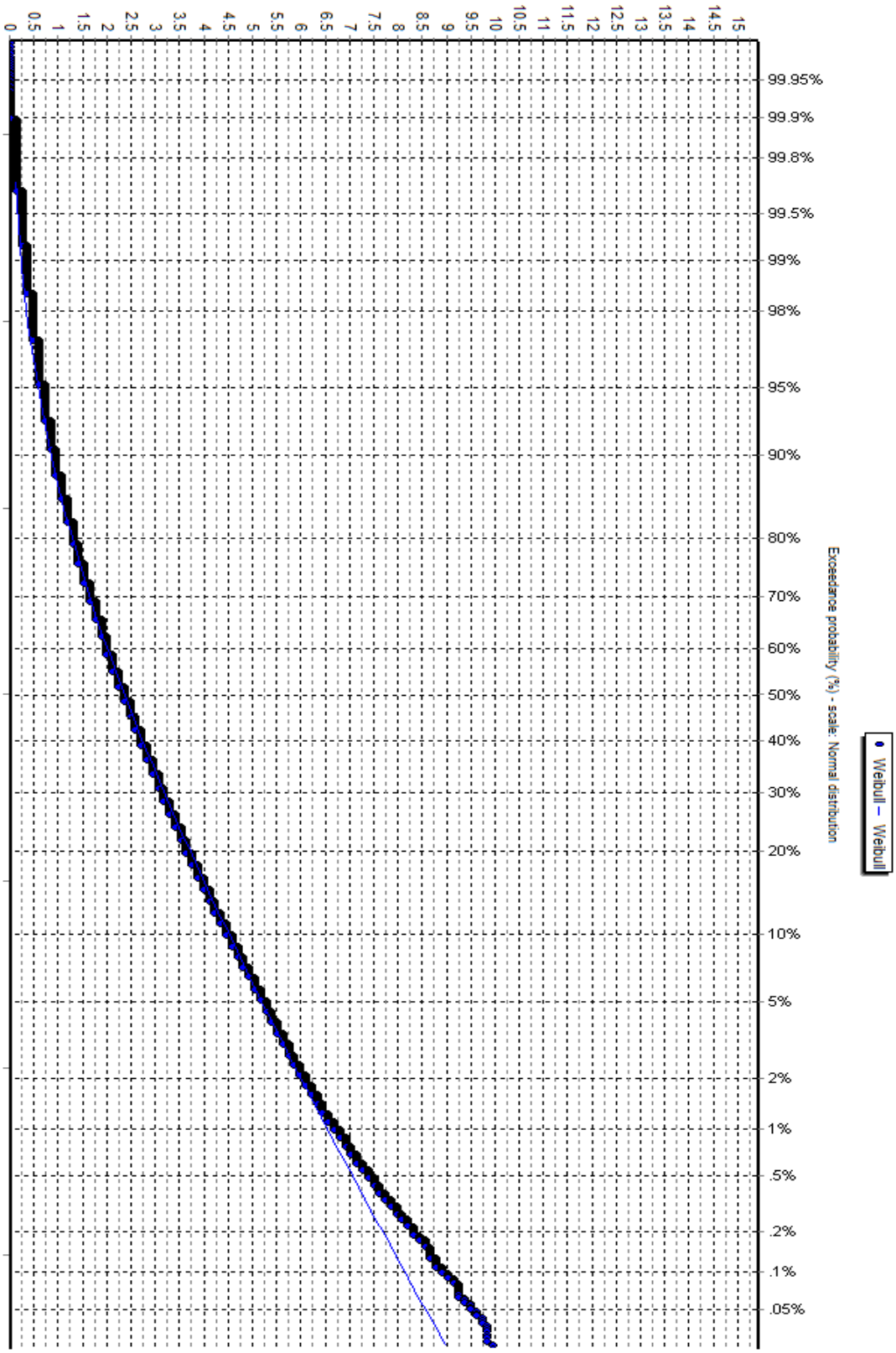

Figure-2.12. Cumulative frequency of 30 m height 10 minute mean wind velocity in the suburb of Cottbus(year 2012). Source: own representation

In **Figure-2.12**, the series value in X axis is the cumulative frequency of mean wind velocity equal or lower then corresponding mean velocity values in X axis. This indicates percentage values in the upper X axis shows the frequency of the wind velocity not more then each velocity in Y axis. The values in the **Figure-2.12** is valid only for the city terrain of the measuring site (Cottbus). The target velocity at the site for this experiment is 5 m/s. From **Figure-2.12**, 7.5% of the total period of the year 2012, 5 m/s wind speed was available for 657 hours out of 8760 hours (365 x 24 hours)at the site. This data will be used for the calculation of the wind turbine parameters (cut in speed, cut-out speed, maximum power etc) in the further research.

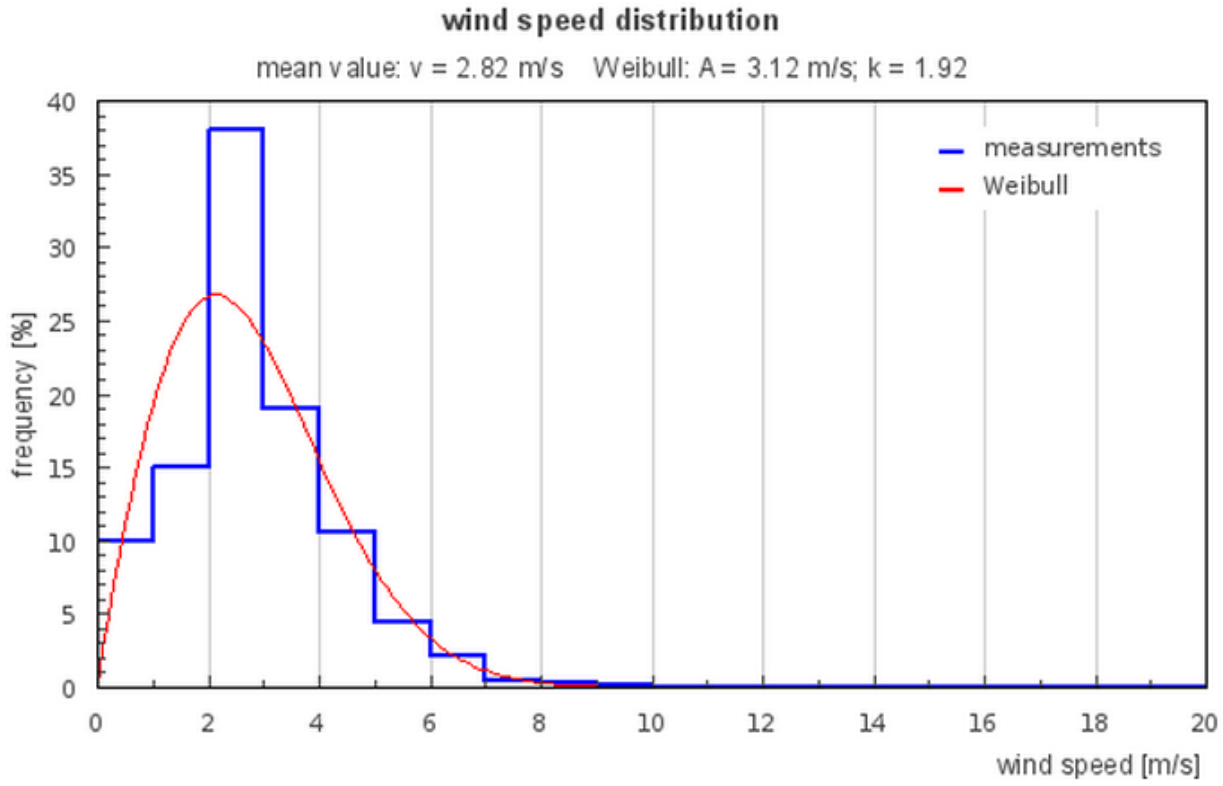

Figure-2.13. Probability density function (Weibull-Rayleigh distribution at k≈1.92) of 30 m height 10 minute mean wind velocity in the site (City terrain Cottbus, year around data 2012). Source: own representation.

Figure-2.13 shows the Weibull distribution curve. This figure represent the calculated k and A value from the data of the year 2012. The frequency ranges were determined from **Figure-2.12**. Along X axis velocity ranges are plotted with an interval of 1 m/s and along Y axis frequency distribution of each velocity classes for the whole year is plotted. k is obtained as 0.12 and A is 3.12 m/s from the calculation from **Equation-2.6**.

2.6. Wind rose

Wind rose diagram is a very necessary tool to describe the wind speed frequency distribution and possible energy yield from the location. The wind rose only describe the relative distribution of wind directions, it is not the actual level of the mean wind speed [31]. To indicate the information about the distributions of wind speeds, and the frequency of the varying wind directions wind rose describe the situation on the basis of wind speed and wind directions data from the source [11]. Data obtained from the site include direction and velocity of the wind for 10 minutes. The velocity record at 10 m height was converted to the velocity record at 30 m height using the power law equation (Section-2.3.1, **Equation-2.1**). **Figure-2.14** was divided into 16 sectors each for 22.5˚ of horizon around the measuring site. The outer circle was divided into 16 circles with 16 different progressively varying diameter with a fixed interval between the diameter of each circle. Each circle represent a varying speed group of 0.5 m/s. Incoming wind direction of the wind on the compass was set North at 0˚ of the horizon with a progressive changes of 45˚ clockwise for each angular section around 360 ˚(Section-2.3.2, wind direction). The wind speed is classified in to 8 different wind classes and the relative frequency from each direction of the horizon is represented with 16 different direction. The target wind speed class which is the concern for this experiment is 5 m/s. This wind speed class is available from all direction of the site through out the year of 2012.

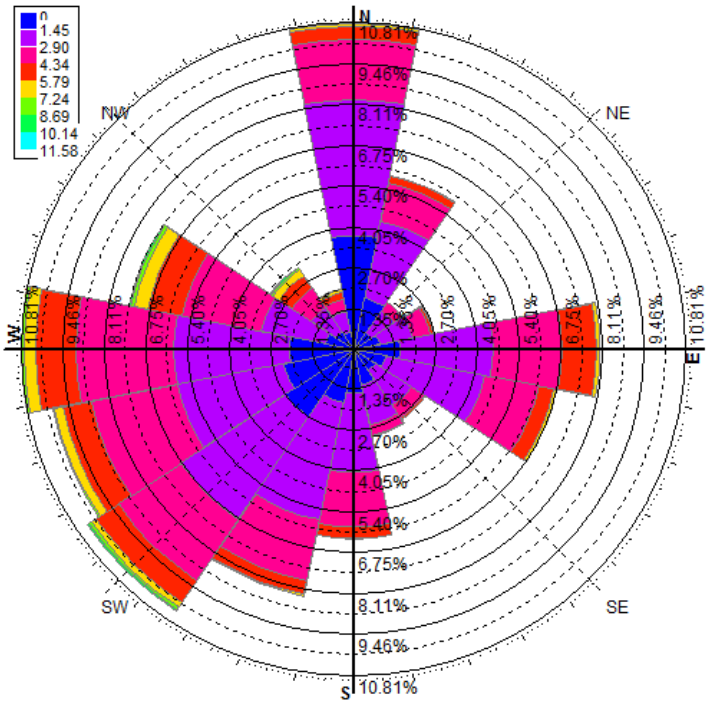

Figure-2.14. Wind frequency distribution representation with wind rose diagram (city terrain data for Cottbus, 2012). Source: own representation.

3. Laser Doppler Anemometry

3.1. Measurement Principle of Laser Doppler Anemometry (LDA)

Laser Doppler Anemometry is a non intrusive measurement technique. This technique is particularly useful for the velocity measurement where non intrusion is a prior condition. In this experiment, measuring wind velocity at different locations around the model with the presence of high turbulence of the flow, LDA was very suitable. The non intrusive nature, high special and temporal resolution and accuracy and ability of the reserved flow has attributed LDA as the very best and optimized measurement technique distinctly for this experiment. High directional sensitivity and high data acquisition rate has been an additional criteria to obtain accurate measurements in the intended locations. The wind tunnel test section allowed us to conduct measurement with optical access through the transparent glass wall vertically positioned outward. **Figure-3.1** represent the schematic diagram of the LDA technique [34].

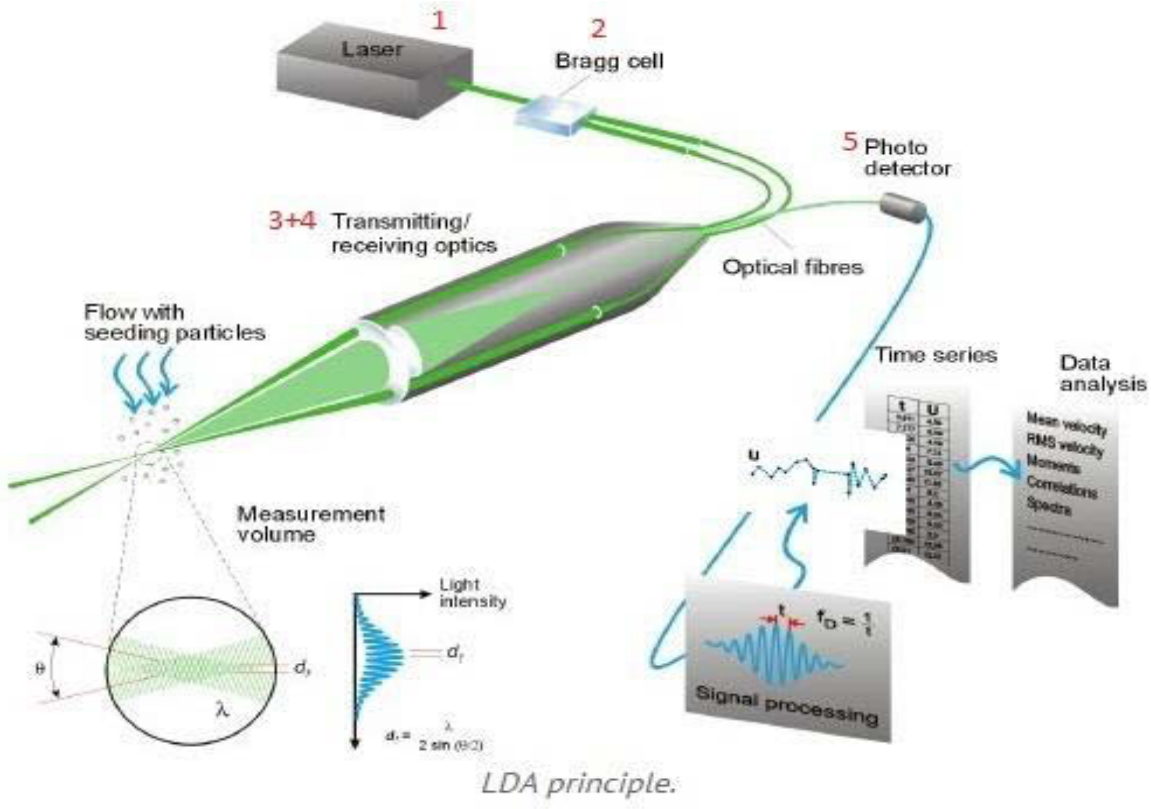

Figure-3.1. Schematic of LDA. Source: [34]

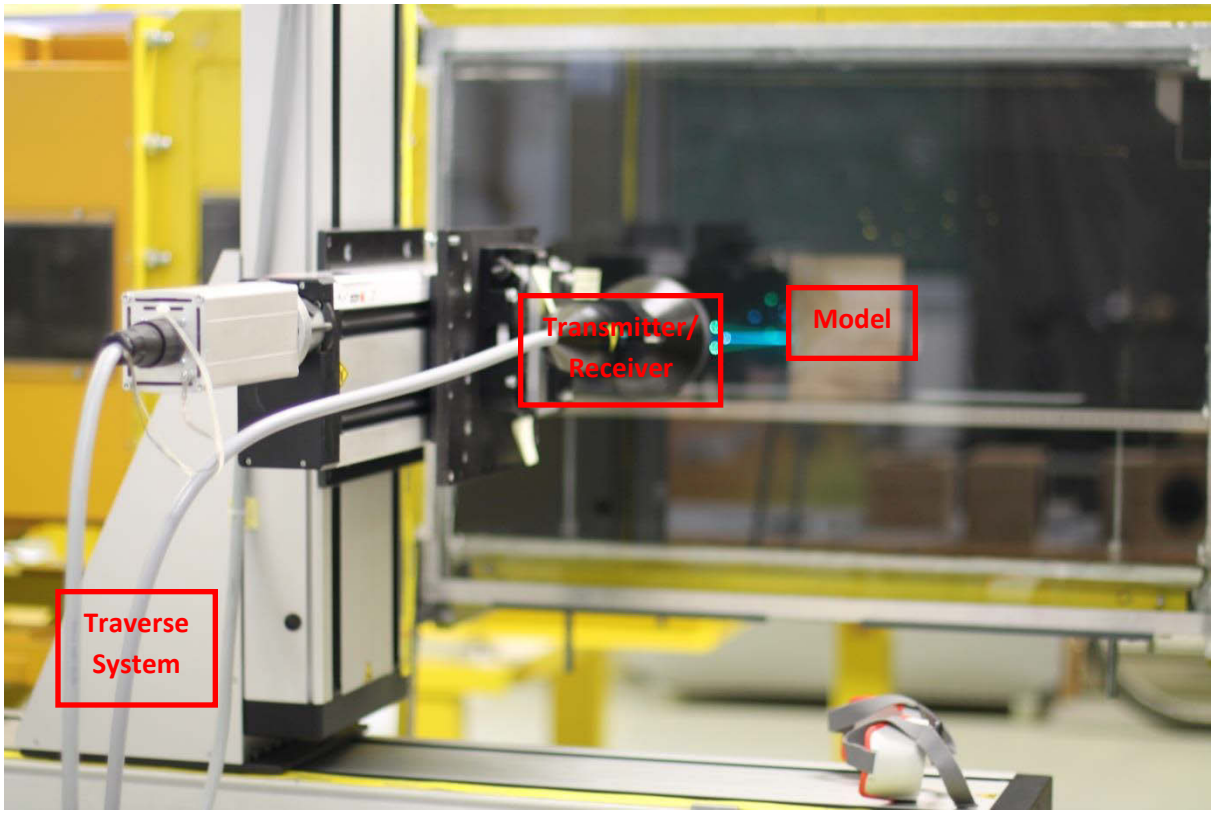

Figure-3.2. Photograph of measurement technique at the experimental setup. Source: own representation.

Basic configuration of the LDA setup used for this experiment are as follows

- A continuous wave laser.
- A brag cell.
- Transmitting optics which includes beam splitter and focusing lens.
- Receiving optics which consists of a focusing lens, an interference filter.
- Photo detector with a signal detector and signal conditioner.
- A traverse system with 3 dimensional motion for precise positioning of the transmitting and receiving optics [34].

3.1.1. Brag cell

A brag cell (**Figure-3.1** (2))is a vibrating piezo crystal attached with a glass crystal which creates acoustical waves through vibration. This acoustic wave works like an optical grid. Brag cell is also used as a beam splitter. The output of the brag cell is to produce 2 beams of equal intensity which can be described as f_0 and f_{shift} respectively [34].

3.1.2. The probe volume

Interference between the laser beams causes the light intensity to be modulated. This interference of modulated light intensity produces a parallel planes of high light intensity, this area of interference is also known as “Fringe”. Fringe is a pattern of alternating light and dark plane. It is usually few millimetre long. The fringe distance (d_f) (see **Figure-3.1**) is defined as the function of wavelength of the laser light and the angle between the beams which can be represented as following.

$$d_f = \frac{\lambda}{2Sin(\theta/2)} \qquad \text{[Eq-3.1]}$$

Flow velocity information comes from light scattered by tiny "seeding" particles generated from a device known as particle generator. The particles move through the probe volume which scatters light proportional to the local light intensity. When the scattered light received in the receiving optics, the scattered light contains a Doppler shift. This shift in the received frequency is known as Doppler frequency (f_D). f_D is proportional to the velocity component perpendicular to the bisector of the two laser beams, which corresponds to the x axis shown in the probe volume (**Figure-3.1**). The scattered light is collected by a receiver lens and focused on a photo-detector. An interference filter mounted before the photo-detector passes only the required wavelength to the photo-detector. The filter removes unexpected noise from ambient light and from other wavelengths [34].

3.1.3. Signal processing

The fluctuation of the light reflected from the seeding particle at the probe volume when received by the photo detector is converted to the electrical signal. This fluctuation in light intensity is known as “Doppler burst”. Due to the intensity profile of the laser beams, this Doppler burst profile is sinusoidal with a Gaussian envelope. The Doppler bursts are filtered and amplified in the BSA signal processor. Signal processor determines f_D for each particle. The frequency analysis of the incoming signal is done using the robust Fast Fourier Transform algorithm. The fringe spacing (d_f) provides information about the distance traveled by the particle. The Doppler frequency (f_D) provides information about the time [34].

$$t = 1/f_D \qquad \text{[Eq-3.2]}$$

Since, velocity is the ratio of distance and time. The Doppler frequency (f_D) is proportional to the flow velocity at measurement point [34] the expression for velocity thus becomes:

$$\text{Velocity, } v = d_f \cdot f_D \qquad \text{[Eq-3.3]}$$

3.1.4. Determination of the sign of the flow direction

Bragg cell is responsible to obtain frequency shift which in turn move the fringe pattern at constant velocity. U_{pos} and U_{neg} generate signal frequency f_{pos} and f_{neg} respectively. LDA system

can not measure zero velocity or positive and negative flow direction directly unless the frequency shift (f_{shift}) obtained from the intersection of the line joining corresponding (U_{pos}, f_{pos}) and (U_{neg}, f_{neg}) points (**Figure-3.3**) [35].

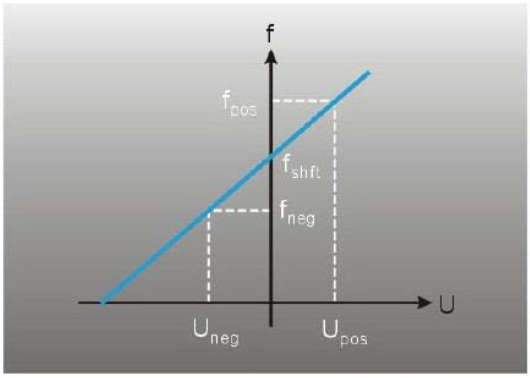

Figure-3.3. Determination of the sign of the flow direction. Source: [34].

3.1.5. Traverse System

An automatic traverse system was used to the LDA measurement system for the positioning of the LDA probe in the flow accurately. The traverse system was configured in such a way so that the grid position input can be given prior to the measurement. The traverse can be moved in 3 dimensional axial movement, X,Y,Z respectively (See **Figure-3.1**).

3.1.6. Particle Generator

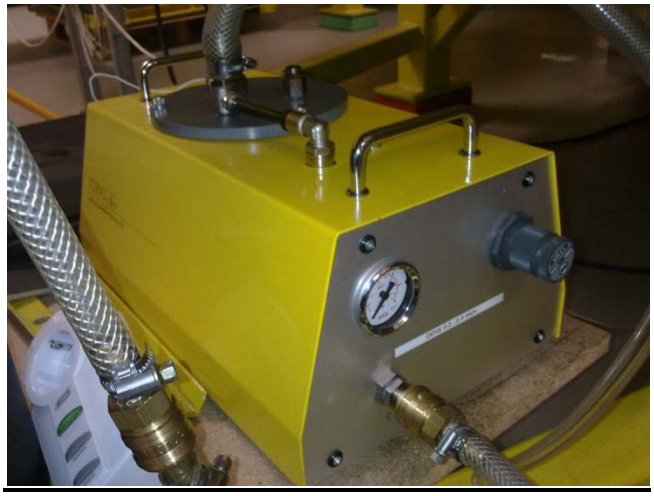

Figure-3.4. Particle generator. Source: own representation.

Particle generator (**Figure-3.4**) is a device operated pneumatically to generate micron sized particles responsible for flashing lights from the measurement location in the flow.

4. Wind Tunnel Experiment

This chapter illustrates a brief description of the wind tunnel used for the experiment and its different components, model scale, description about the assumptions made and similarity parameters, experimental setup, model geometry, model layout and location of the model in the tunnel, description of the measurement locations around the model and the necessity to measure in such location, flow visualization technique used and the obtained flow visualization photographs with a summery of the flow visualization deductions of different models, calculation method for measuring data, free stream flow quality and turbulence intensity profile in the wind tunnel used for this experiment, deviation of real scale atmospheric boundary layer from the real scale atmospheric boundary layer, measurement and result at different locations around the model with applied velocity, finally the energy obtained from the flow and the result analysis considering the obtained result of velocity and turbulence data.

4.1. Wind tunnel Experiments

Building integrated wind turbines are certainly site specific. Different regions around the world has different wind potential. The fact which can not be ignored that the urban architectural trend of the buildings in a specific region is unique then other region. Though there is a certain similarity in the trend of regional architecture over the whole country but it is a common practice in general that building sitting is set to the orientation towards the maximum wind velocity distribution and availability around the year. Due to the limitation of the size of the wind tunnel used for this experiment, the selection of the model dimension was simplified. The test section of the wind tunnel is 1.8 m long, 0.6 m in width and 0.5 m in height.

4.2. Wind tunnel description

The closed loop aerodynamic wind tunnel at the Department of Aerodynamics and Fluid mechanics of Brandenburg Technical University was used for this experiment to obtain velocity at different locations of the models with different duct geometries. While using Laser Doppler Anemometry (LDA) as a measurement technique, closed loop wind tunnel is more advantageous then an open flow wind tunnel. The flow is undisturbed from indoor flow conditions and other external influences for closed loop flow. Even the flow quality is better due to (corner) turning vanes at corners and screens. Continuous recycling of the seeding particles in a closed loop was quite appropriate for the measurement technique (LDA) used. Moreover, less noise was an additional advantage. The flow pattern in this wind tunnel was uniform and of less turbulence which was approximately 0.5%.

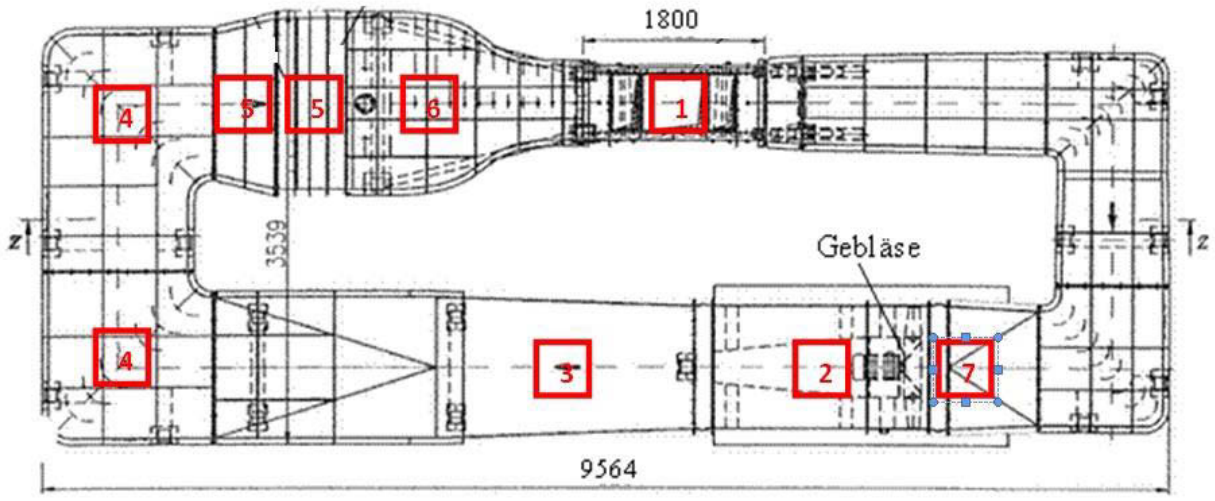

Figure-4.1. Schematic diagram of closed loop aerodynamic wind tunnel at the Department of Aerodynamics and Fluid Mechanics at Brandenburg Technical University. Source: based on [36]

4.2.1. A closed loop wind tunnel is comprised of several sections. In the **Figure-4.1**, significant sections of the wind tunnel is shown with red numbers. Purpose and function of these sections are as follows:

1 Test section: 1.8 m long, 0.6 m width and 0.5 m high test section of this wind tunnel is used to generate appropriate aerodynamic profiles of mean velocity, turbulence intensity and turbulence spectra. The model subjected to actual investigation is placed in this section.

2 Fan and flow straighteners: Flow inside the tunnel is generated with a induced draft fan and the flow straighteners behind the fan removes the swirl in the flow.

3 Diffuser: This transition from smaller cross section to larger cross section reduces pressure loss in the flow.

4 Corner vanes: Purpose of the corner vanes is to change the direction of the flow with an angle of 90˚ with minimum possible pressure loss.

5 Wide angle diffuser and settling chamber: Purpose of the wide angle diffuser is to create a transition of the flow to larger cross section in order to avoid pressure losses in the subsequent components of the settling chamber. The settling chamber contains screens and honeycomb. The purpose of the settling chamber is to reduce difference in transverse and vertical turbulence intensity along the whole cross sectional area of the test section.

6 Turbulence screens and contraction: Turbulence screens reduces the fluctuation in longitudinal velocity/longitudinal turbulence intensity along the cross section. This turbulence intensity reduction occurred further in the contraction section. Moreover, this contraction section helps to align the flow and increase the wind speed due to reduction of the area.

7 Safety screen: Is a mechanism in front of the fan designed to prevent damage to the fan in case of model failure [37].

4.3. Model scale

Cross section of the test section allowed us to limit the size of the model up to 10% of the cross section. According to the best practice guidelines for building simulation in wind tunnel, the blockage ratio should remain within 3-5% of the wind tunnel cross section [37]. Blockage ratio is defined as the ration between the cross sectional area of the model to the cross sectional area of the wind tunnel test section [36].

$BR = A_{model} / A_{windtunnel}$

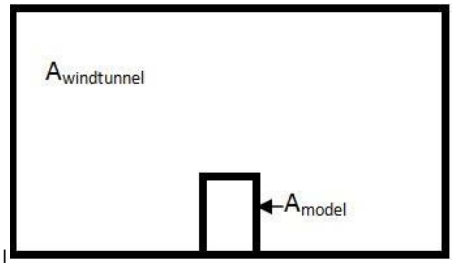

Figure-4.2. Schematic of blockage ratio. Source: own representation.

Unfortunately, the complexity we faced during the experiment for this particular wind tunnel is that the area of the test section is very small compared to an appropriate wind tunnel used for building aerodynamics . Assuming that keeping the model area below or equal to 5% of the test section will definitely lead us to erroneous result due to the smaller size of the models and measurement devices (While using LDA for measurement) . The setting of the scale should consider both obtaining accurate measurement and reduce the wall influence over the flow. However, we decided to manufacture a model which will be appropriately large enough to obtain an accurate measurements in this wind tunnel. Despite measurements with large size models, the influence of the wind tunnel wall over the flow could not be avoided as per the standard measurement technique. The optimization between the limitation of test section area and minimum wall influence over the flow was decided at 10% blockage ratio. To observe the impact of wind over a full scale 30 storey building, we have considered a 1:200 model to be analysed in the wind tunnel. This scale shows the relationship between the model and real buildings which is also known as length scale (λ_L). We have chosen models with the same exteriors with 0.2 m x

0.125 m x 0.15 m of dimensions with four different types of internal duct geometry. In real case, wind impact on a building depends on the type of topography and related roughness class which is discussed in Chapter-2.

Figure-4.3. Comparison between wind tunnel model and real scale building. Source: own representation.

4.4. Model size

Wind velocity profiles and related turbulence at 4 different types of duct geometries were considered to be measured as a part of the approximation to determine the best possible duct geometries to obtain maximum wind power in the duct. According to the wind velocity result analysis inside the duct, wind turbine location preference inside the duct will be decided (Scope for future measurement). Brief description of these 5 models are explained below.

4.4.1 Model-0 (M-0)

To compare the wind effect on other 4 models, a reference measurement is required to obtain from a bluff body model with similar dimension. M-0 was measured for a standard comparison with the other models having ducts.

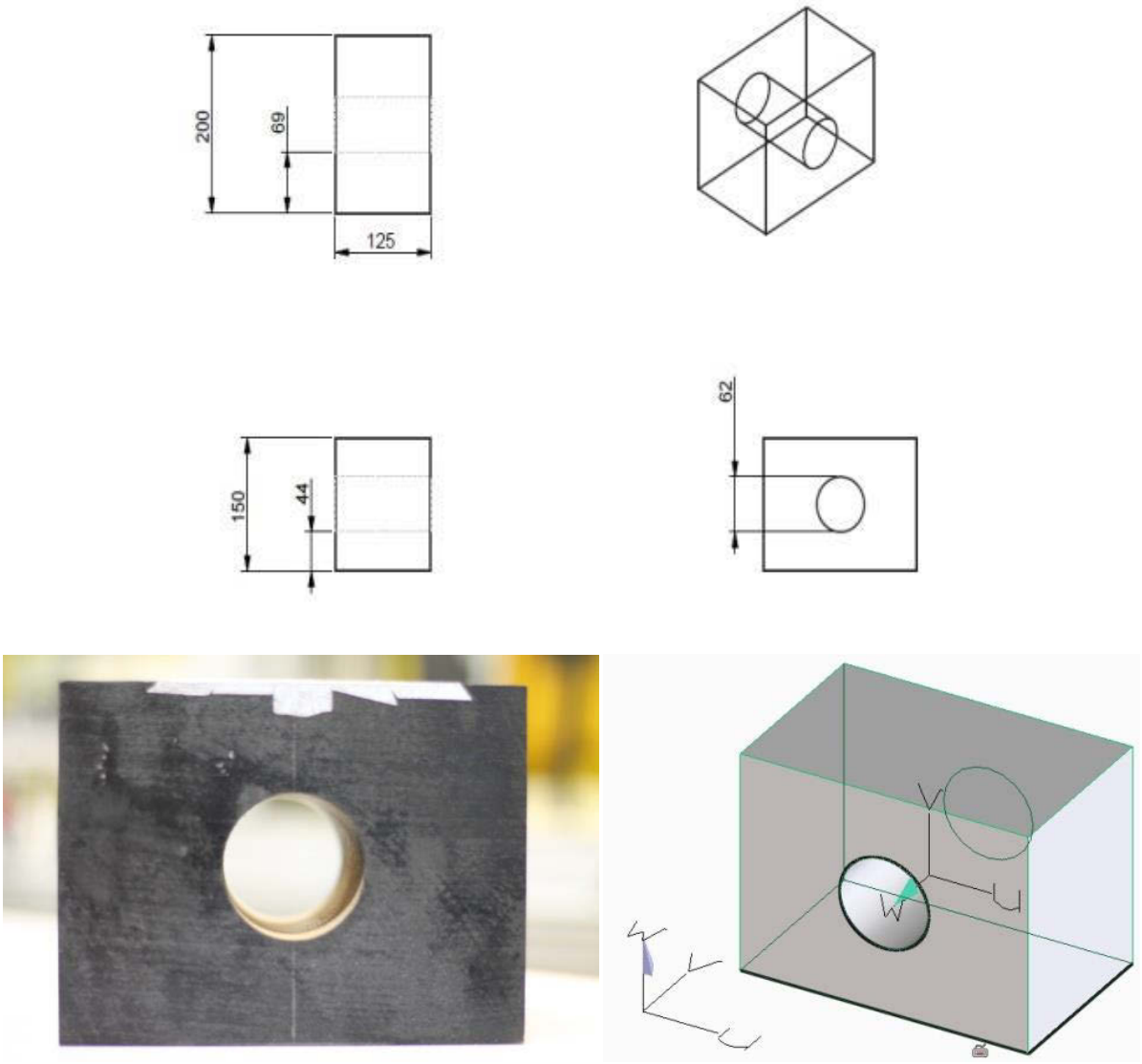

Figure-4.4. Schematic representation of M-1 geometry. Source: own representation.

4.4.2. Model-1 (M-1)

Integrated duct is a simple circular geometry with uniform diameter of 0.062 m . Thus, a constant area of 3.02 x 10^{-3} m^2 remain over the whole length of the duct from inlet to outlet. (**Figure-4.4**)

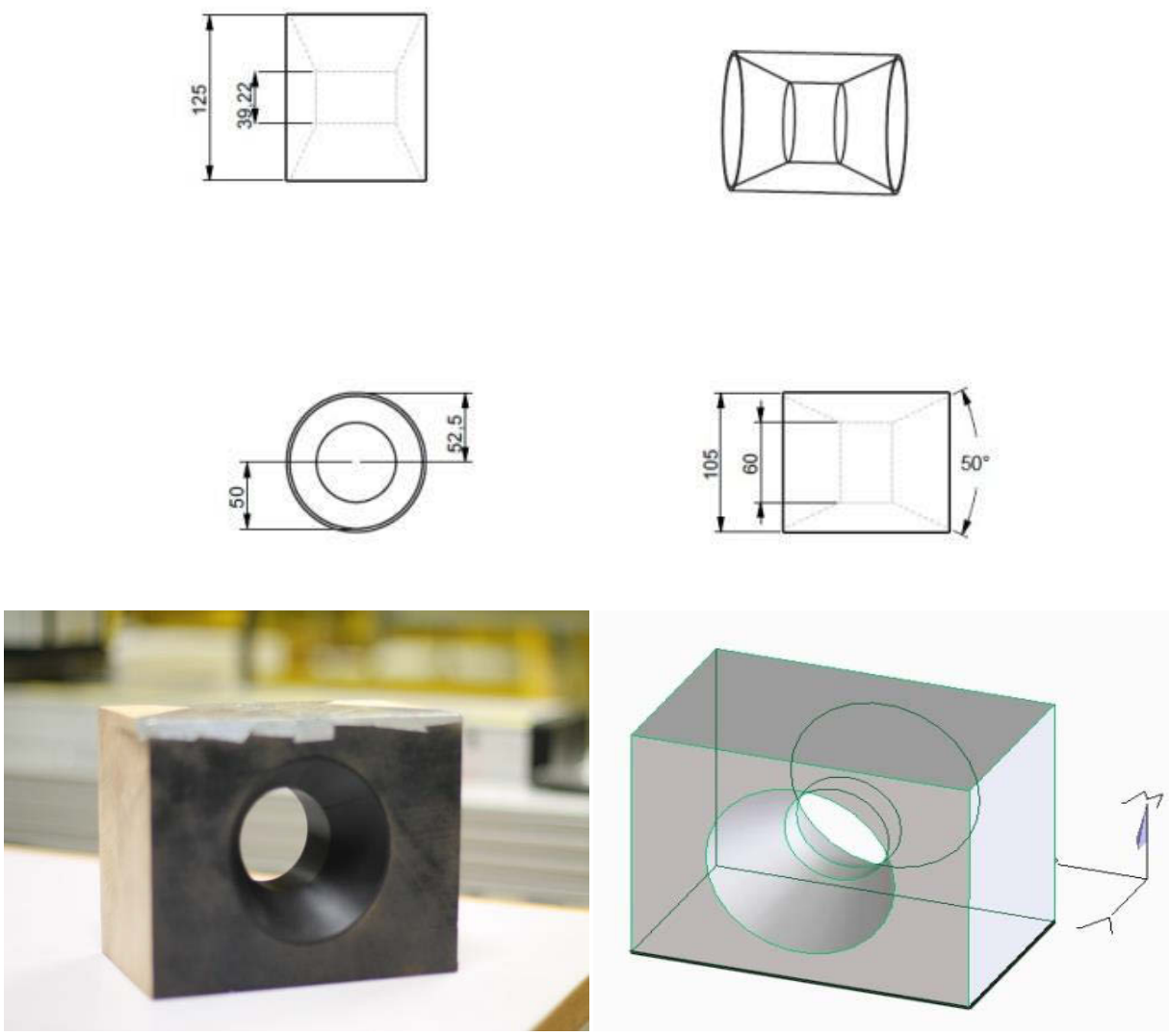

Figure-4.5. Schematic representation of M-2 geometry. Source: own representation.

4.4.3. Model-2 (M-2)

It is a model with varying diameter duct geometry. The inlet and outlet is of a funnel shaped duct where inlet and outlet of the duct gradually merge from 0.105 m to a constant diameter of 0.060 m at the middle. Thus, a gradual reduction in the area of 7.854 x 10^{-3} m^2 from both inlet and outlet to an area of 2.83 x 10^{-3} m^2 at the middle for 0.03922 mm length along the duct. (**Figure-4.5**)

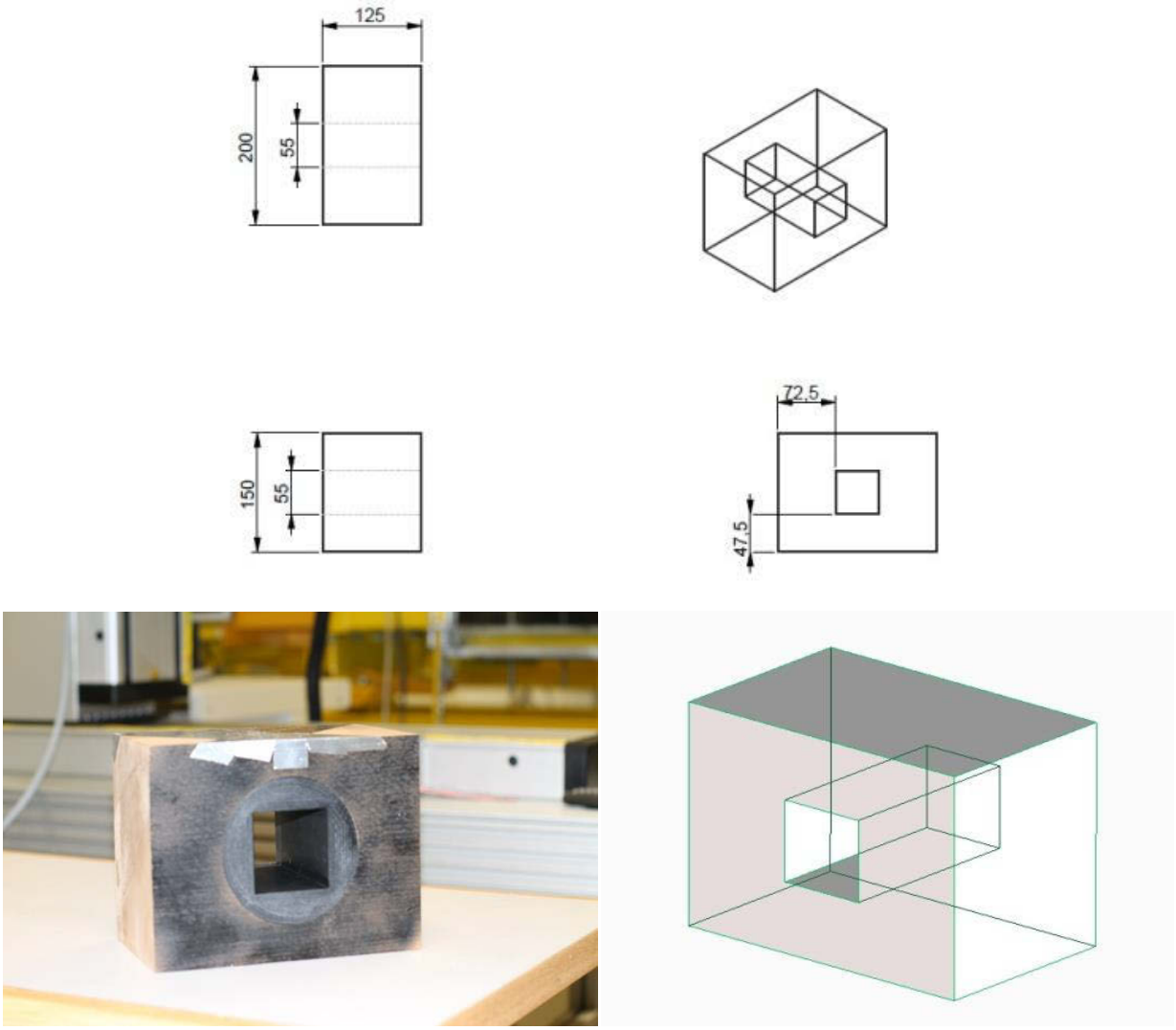

Figure-4.6. Schematic representation of M-3 geometry. Source: own representation.

4.4.4. Model-3 (M-3)

It is a model with simple rectangular duct geometry with a constant profile along the whole length of the duct. All the arms of the rectangle is of equal length which is 0.055 m. Thus, a constant area of 3.025 x 10^{-3} m^2 remains along the whole length of the duct. The area of the cross section of the M-1 is equal to the area of model-2. (**Figure-4.6**)

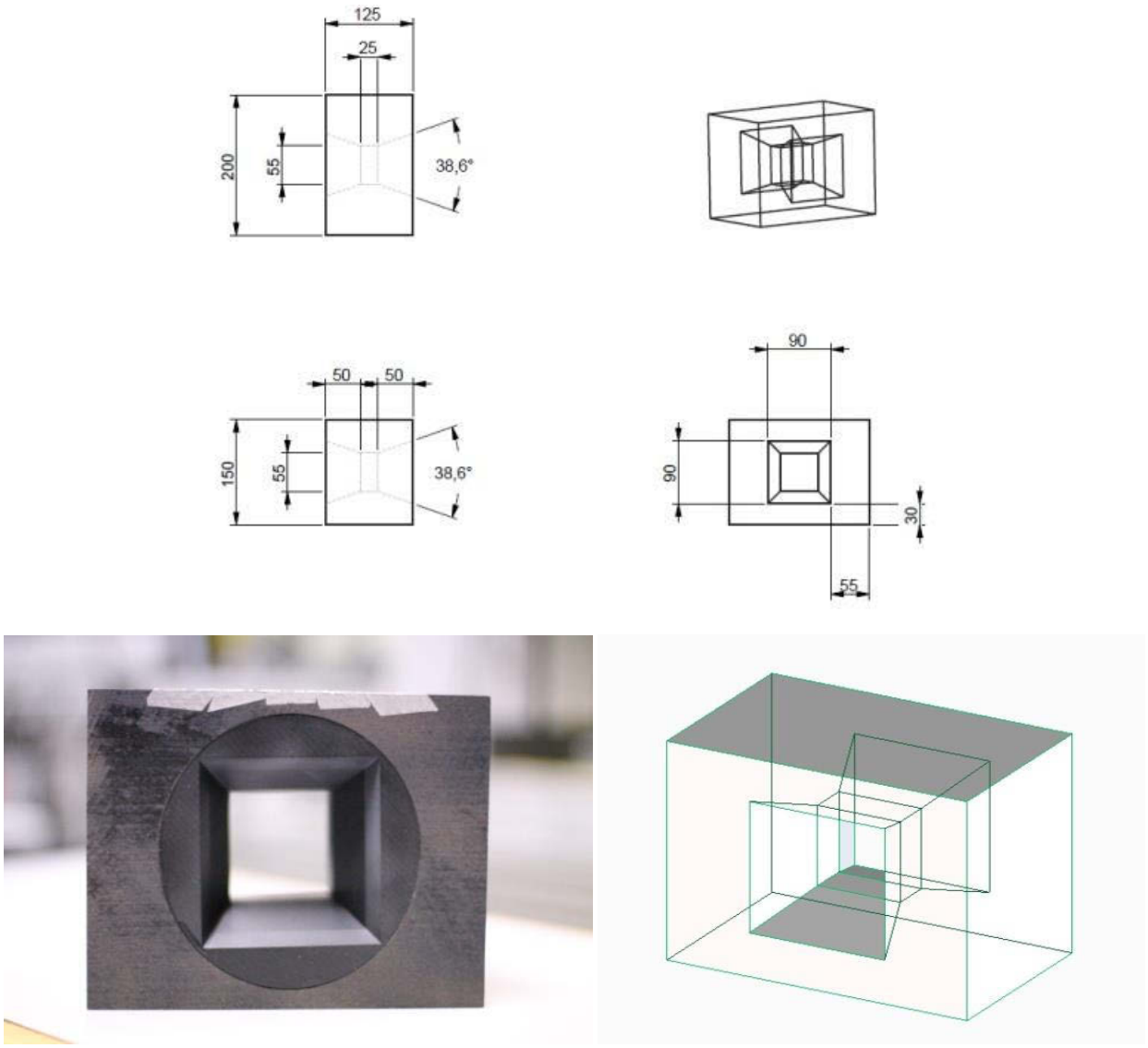

Figure-4.7. Schematic representation of M-4 geometry. Source: own representation.

4.4.5. Model-4 (M-4)

This is a model with a duct geometry of varying area from a larger rectangle with similar arms to a lower rectangular area. The profile was kept with the constant ratio of area reduction. This rectangular funnel shaped area reduces from both the inlet and outlet area of 8.1×10^{-3} m^2 to a constant area of 3.025×10^{-3} m^2 at the middle. At the middle this area remain same for 25 mm length along the duct. (**Figure-4.7**)

4.5. Similarity parameters and assumptions

To obtain an appropriate measurement from a wind tunnel experiment, certain conditions have to be complied. There are several parameters that relates the model in the wind tunnel into real scenario such as matching geometric similarity- which concerns matching scale of the real buildings and the models, kinematic similarity-which concerns position, velocity and acceleration of the real flow and applied flow and dynamic similarity which is , in fact this experiment is not related due to static models. Similarity parameters required for a wind tunnel measurement are as follows.

- Geometric similarity-proper scaling of buildings and topographic features.
- Matching Reynolds number.
- Matching Froude number.
- Matching Mach number.
- Rossby number.
- Kinematic simulation of air flow, flow velocity distribution and turbulence.
- Zero pressure gradient.
- Effect of temperature gradient.
- Temporal scale (λ_T).
- Velocity scale (λ_U).

4.5.1. Geometric similarity-Proper scaling of buildings and topographic features

Matching geometric features is one of the prime requirements for wind tunnel testing. Geometric similarity features for this experiment has already been described in the model scale section of this chapter.

4.5.2. Matching Reynolds number

In this experiment it is not possible to simulate similar Reynolds number value of the flow as the real scale flow. The value of density (ρ) and viscosity (υ) is same as the real scale flow (In this case, ρ =1.185 kg/m^3). We have used a 1:200 scale model, as such to simulate similar Reynolds number in the wind tunnel flow we have to apply a flow which has a velocity 200 times higher then the actual velocity. This is quite impossible. However, this difference between Reynolds number in wind tunnel and in real scale building does not effect the experimental result [37]. In this regard one could mention the famous quote from Plate and Cermak (1963), “Matching Reynolds number is not often possible. But exact matching is often not needed if the models have sharp edges e.g point of flow separation are fixed. And also when minimum Reynolds number Threshold value is exceeded, typically in the order of 10000” [38]. That is

distortion of the flow is considered negligible for Re >10^4. Reynolds number of the flow is very important in determining the type and dimension of the boundary layer and of the separation points at the model sharp edges. Reynolds number for this experiment remained same for all models. Assuming same value for ρ and μ as through out the experiment, Reynolds number obtained is as follows

$$\mathrm{Re} = \frac{\rho v \mathrm{D}}{u} \qquad \text{[Eq-4.1]}$$

Density of air, ρ = 1.185 kg/m^3

Dynamic viscosity of air, ν = 1.7894 x 10^{-5} kg/m.s,

Inlet velocity, u = 5 m/s

and height of the test section as hydraulic dia, $H_D = 2ab/a + b = 0.5454\ m$ [Eq-4.2]

(width, a = 0.6 m and height, b = 0.5 m of test section of the wind tunnel)

the Reynolds number for the flow in wind tunnel is obtained as Re≈$1.8 \cdot 10^5$. As the building models used for this experiment have sharp edges where the flow separation take place same as the real scale buildings. Moreover, higher value of Reynolds number indicates turbulent flow around the models In bluff body aerodynamics, sharp corners tend to cause immediate flow separation independently of the Reynolds number of the flow, thus, bluff bodies Reynolds number simulation can be relaxed. we can neglect simulating similar Reynolds number as distortion of the flow and changes in boundary layer parameters are of very negligible amount.

4.5.3. Matching Froude number

It is required only when the model motion and aerodynamic forces like drag and lift of the model is required. In this experiment similitude of Froude number is not required.

4.5.4. Matching Mach number (Ma)

Ma is an important parameter to simulate real scale flow into wind tunnel. Ma is defined as the ratio of the flow speed to the speed of the sound. Ma can be expressed as

$$Ma = \frac{v}{c} \qquad \text{[Eq-4.3]}$$

where v stands for the applied wind speed and c is the speed of sound in air. In this experiment Mach number is same both in real scale flow and in wind tunnel flow. However, for low velocity testing matching Mach number is often not required [38].

4.5.5. Rossby number

Rossby number concerns the effect of rotation of earth on the wind. Matching Rossby number similarity is often not possible in wind tunnel simulation [38].

4.5.6. Kinematic similarity

Matching kinematic similarity of airflow, velocity distribution and turbulence is another similarity parameter of the wind tunnel simulation. It is better to measure velocity distribution at wind tunnel simulation up to 130% of the height of the model but it is more preferred to measure up to the ceiling of the test section [38]. As stated previously that the wind tunnel used for this measurement is an aerodynamic wind tunnel where the measurements were taken in aerodynamic flow. Measurements were taken up to 130% of the model but the results were represented to the model height.

4.5.7. Zero pressure gradient

Simulating zero pressure gradient found in the real world in wind tunnel condition can not be satisfied by the fact that the flow profile in the tunnel is aerodynamic. Additionally, assuming neutral stratification of the real world, temperature gradient in the wind tunnel is assumed to be zero due to turbulent flow (Re >3000).

4.5.8. Effect of temperature gradient

Effect of temperature gradient is one of the similarity parameters in wind tunnel simulation. However, if the flow is sufficiently turbulent, deviation in the real scale temperature gradient and in wind tunnel can be considered negligible [38]. Due to high turbulent flow in this experiment, we can assume that there is sufficient mixing in the flow. As such, temperature gradient deviation can be considered negligible.

4.5.9. Temporal scale (λ_{Tu})

There are certain deviation in the upstream and downstream data measurement. In this experiment each location at the upstream were measured based on data obtained for 3 second where as the downstream locations were measured on data obtained for 30 seconds. This is such as the upstream flow is less influenced due to turbulence but downstream flow is not. From the flow visualization section of this chapter, the visible distribution of the streamlines in the flow field at upstream location virtually had no fluctuation. Assuming negligible fluctuation at the upstream flow, two different temporal scale were taken for the upstream and downstream location. Temporal scale for upstream measurement (λ_{Tu}) is as:

$$\lambda_{Tu} = T_m/T_p = \frac{3\,s}{600s} = 0.005 \qquad \text{[Eq-4.4]}$$

Temporal scale for downstream flow:

$$\lambda_{Td} = T_m/T_p = \frac{30\,s}{600s} = 0.05 \qquad \text{[Eq-4.5]}$$

4.5.10. Velocity scale (λ_u)

According to the definition of velocity, $u = \frac{l}{t}$, for this experiment velocity scale (λ_u) can be defined as:

$$\lambda_u = u_m/u_p = \lambda_l/\lambda_t \quad \text{[Eq-4.6]}$$

As stated in the model scale section of this chapter, length scale (λ_l) for this experiment is 1:200. There are two different velocity scale as stated before for upstream and downstream locations are as follows:

Upstream velocity scale, $\lambda_{U_u} = 1$ and Downstream velocity scale, $\lambda_{U_d} = 0.1$.

4.6. Model layout and measurement location

Determination of the appropriate design of the duct geometry depends on the data obtained about the velocity distribution in certain locations around the building. To generate wind energy from building integrated ducts, most important decisive factor is the velocity obtained and the level of turbulence in the ducts. LDA Measurement technique used in this experiment allowed us to measure only the locations outside the models. Models were placed 0.5375 m away from the upstream flow in the test section. Models were placed at 0˚ angle of attack (AOA) with the longitudinal axis along the length of the test section to measure an upstream flow of 5 m/s. Duct centreline was placed at the centre of the test section width which allowed us 0.2 m of free space at both sides of the model and 0.35 m free space over the top of the model. Due to this position the applied air flow influence over the model had enough space to be measured.

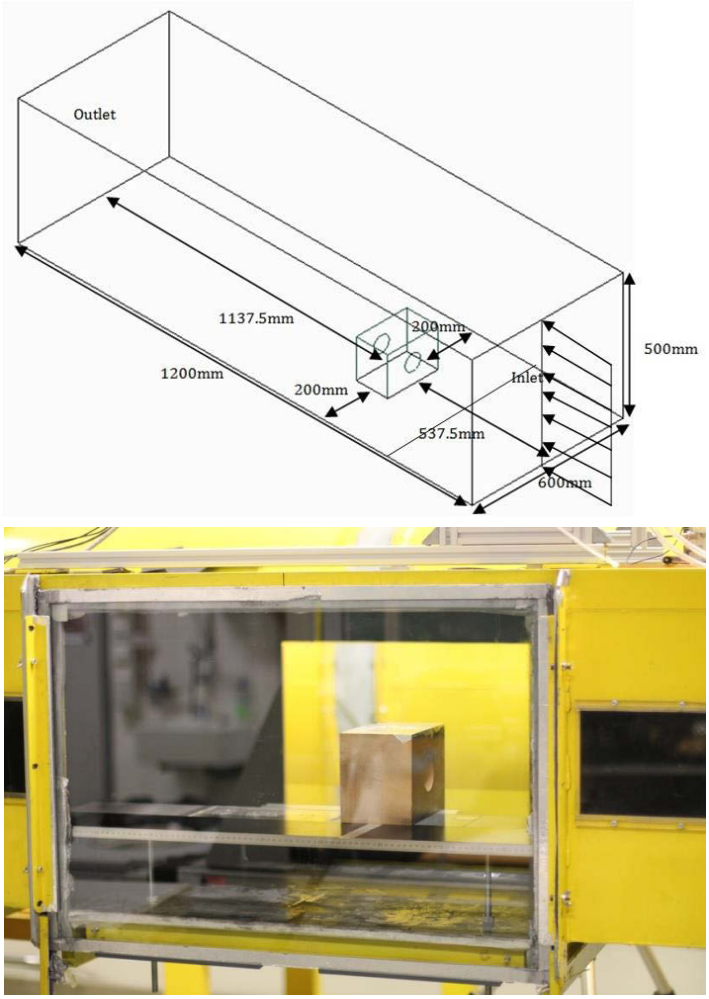

Figure-4.8. Model location at wind tunnel test section. Schematic (Top) and Photograph (Bottom). Source: own representation.

Determination of the flow velocity as a physical parameter at the inlet and outlet of the duct is very important in calculating the power output obtained from the flow in the duct. For ultimate comparison between different geometries of the duct in obtaining maximum power output from the applied flow, inlet velocity is the prime variable. Theoretically, wind power available in the flow can be obtained from the **Equation-1.1**.

$$P = \frac{1}{2}\rho A v^3 \qquad \text{[Eq-1.1]}$$

where, P is the theoretical power of the flow (Watt), ρ is the density of air (kg/m^3), v is the velocity obtained from the flow (m/s), A is the cross sectional area of the duct (m^2)

Assuming that the value of air density (ρ) remain same for the measurement value for all ducts which is in this case 0.184 kg/m^3, Cross sectional area for M-1 and M-3, M-2 and M-4 is same. The only variable that varies according to different geometry is velocity. In order to compare M-1 with M-3 and M-2 with M-4, we have selected certain regions around each model. To compare

obtained results with a bluff body of similar dimension, M-0 was used in this experiment as a benchmark. To asses wind resource in wind tunnel simulation, we need to measure wind impact on the model with a large range of predetermined model angle to the wind direction and wind velocity. However, due to time constrains for all necessary measurements required for a concrete analysis, we have kept a constant velocity of upstream flow of 5 m/s and 0˚ angle with the duct axis to the wind direction (**Figure-4.8**). As mentioned previously, data obtaining time for the inlet and outlet locations were 3 second and 30 second respectively. For all the upstream measurement location, 3,000 and for downstream locations 15,000 particles were measured to obtain wind data. There was 3 approach for the determination of the velocity.

- Location-1- A 2D vertical line located at the centre of the inlet and outlet for M-1,M-2,M-3 and M-4. (**Figure-4.9**)
- Location-2-A 2D plane parallel to inlet and outlet of M-1 and M-3.(**Figure-4.10**)
- Location-3-A 2D plane parallel to the flow direction at the longitudinal centre of the model.(**Figure-4.11**)

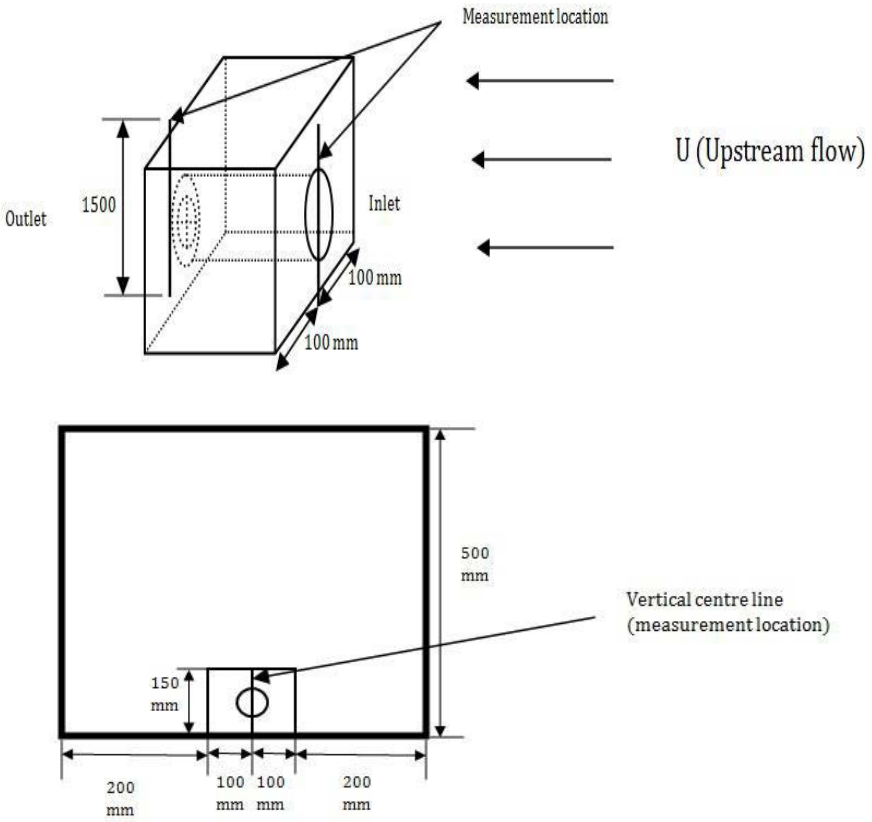

Figure-4.9. Schematic of measurement location-1 at the wind tunnel. 3D isometric (top) front view (bottom) Source: own representation

4.6.1. Location-1

First approach was to determine the wind velocity both at the inlet and outlet. We have decided to measure velocity at the vertical centreline of both inlet and outlet of all models (**Figure-4.9**). Due to the fact that LDA probe volume need minimum 5 mm clearance away from wall (Chapter-3, Section-3.1.2), this measurement position was kept 5 mm away from ground and 5 mm away from both inlet and outlet plane of the models. Measurement grid had a progressive refinement as it reaches the vertical centreline. Height of the location-1 measuring point is same as the model height which is 0.15 m from the ground. There are 95 to 111 measuring grid points at location-1 with a varying resolution of maximum 0.003 m to 0.001 m.

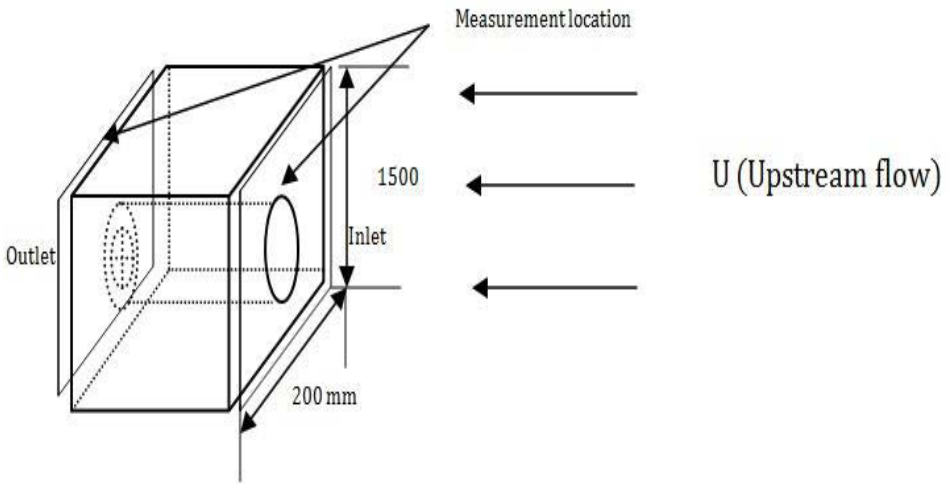

Figure-4.10. Schematic of measurement location-2 at the wind tunnel. Source: own representation.

4.6.2. Location-2

Second approach of measurement was to determine presence of turbulent velocity fluctuation and mean wind velocity distribution along the spanwise direction both at inlet and outlet face of M-1 and M-3. In order to obtain most accurate velocity profiles of these locations, a parallel plane which is 5 mm away from both the faces for M-1 and M-3 (dimension of the area- 0.2 m x 0.15 m : width x height) was decided to measure (**Figure-4.10**). To obtain high resolution of wind velocity data at these locations, progressive refining of the grid at the centre of the face was formulated. The measurement grid for inlet face and outlet face had 1020 and 342 measuring points respectively (**Figure-4.11** and **Figure-4.12**).

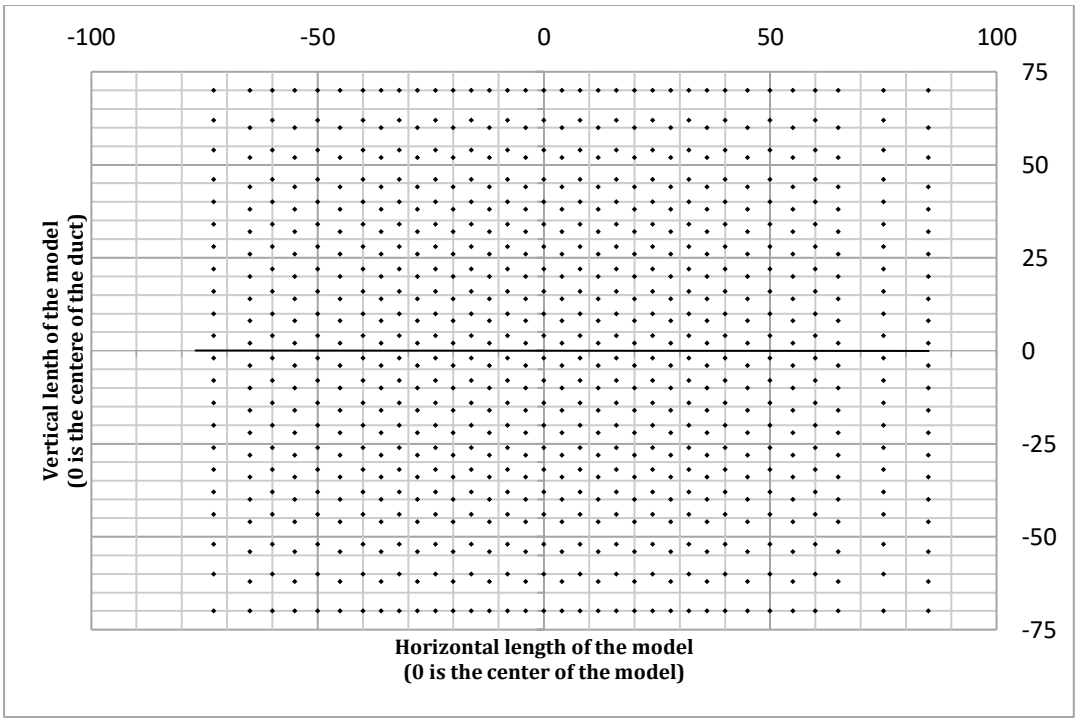

Figure-4.11. Grid of measurement points of location-2 at inlet. Source: own representation.

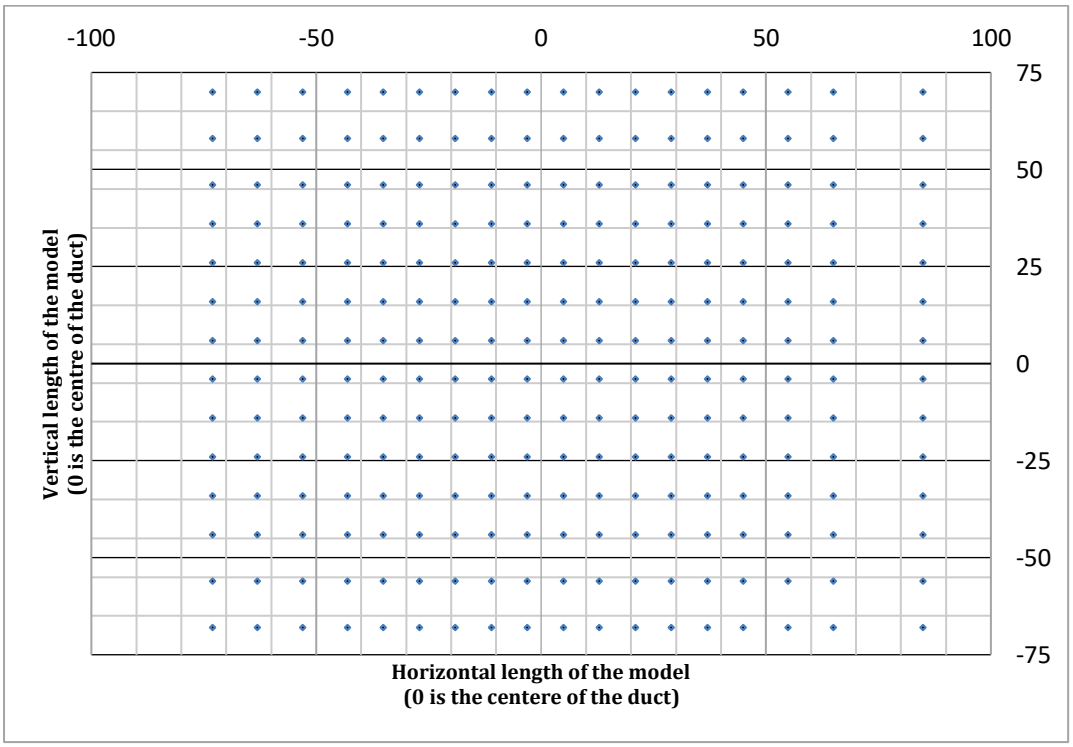

Figure-4.12. Grid of measurement points of location-2 at outlet. Source: own representation.

4.6.3. Location-3

In this case, the plane location was determined as such that the inlet and outlet velocity along with the velocity distribution over the top of the model can be predicted accurately as a contour (**Figure-4.13**). This 365 mm in length and 190 mm in height measuring grid was positioned at 120 mm away from the inlet face of the model and 120 mm after the outlet face. From the **Figure-4.13** the side view of the plane location can be apprehended. The plane consist a total of 3026 grid points out of which 1650 is located at upstream flow before the inlet face, 364 grid points are located over the top surface of the model and 1012 grid points are located at downstream after the outlet face. The grid had progressive refinement from free stream velocity towards near wall region of the model. This measurement will provide velocity information of the inlet and outlet jet.

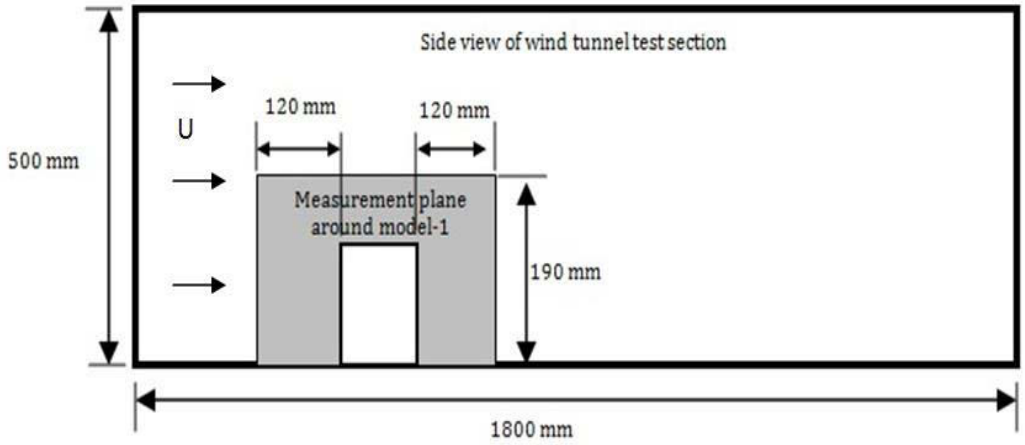

Figure-4.13. Schematic of measurement location-3 at the wind tunnel. Source: own representation.

4.7. Flow Visualization using laser light illumination technique

Flow visualization around the models in wind tunnel is required to predict certain fluid flow parameters such as aerodynamic roughness length (Z_0), boundary layer thickness (δ), flow separation points (usually at sharp edges), location of transition points between laminar to turbulent region [39], level of turbulence where the flow is effected by the model, etc. For this experiment, we have decided to visualize the flow pattern around the models placing at the same position in wind tunnel as the LDA measurement.

Figure-4.14. Photograph of laser lens mechanism. Source: own representation.

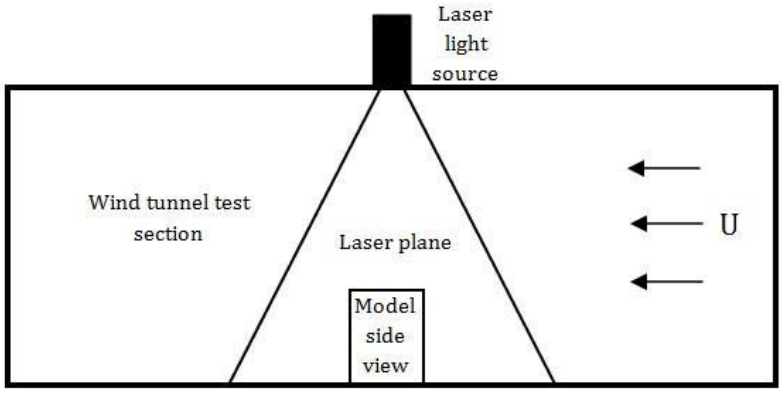

Figure-4.15. Schematic of flow visualization setup. Source: own representation.

A smoke generator was used to generate heavy smoke in upstream wind, which then passes over the model. The smoke generator generate particles of oil droplets of about 1 μm diameter which creates streamlines in the flow field. The flow passing through the model is then made visible with the help of a laser light sheet. This plane of illuminated streamlines are generated by a laser light source in conjunction with a lens mechanism (**Figure-4.14**) which consist of two diverging lens mechanism. This technique illuminate a perpendicular plane around models showing flow streamlines covering a part of inlet flow, outlet flow and the flow over the top surface of the model (**Figure-4.15**). For this experiment, flow pattern at inlet and outlet area is important from velocity and turbulence point of view. However, sharp edges are also important to identify the location for flow separation. Detecting corner vortices and turbulent region is also considered significant for localized suction as flow velocity can be increased as the streamlines converges in certain regions. Still pictures were taken for further study and analysis. Only one location of photography is considered for all models to record the side view of the test section. A video recording of the flow was done and when played at slow rate, it provides useful details of the flow over the roof and could be analyzed for further information about the flow phenomenon.

Flow visualization was conducted at 2.8 m/s velocity as such the Reynolds number of the flow was 10^5. Same Reynolds number was maintained through out the data recording for flow visualization.

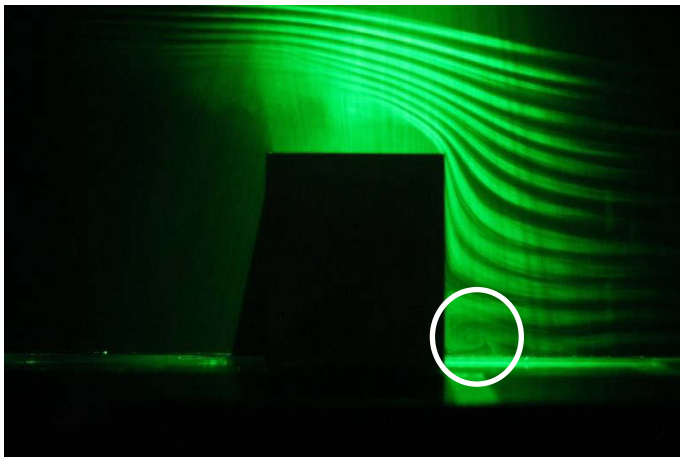

Figure-4.16. Flow visualization of M-0. (Layout of horse shoe vortex marked in circle). Source: own representation.

4.7.1. Flow visualization (M-0)

Figure-4.16 gives the streamlines of the flow in the region close to the wall. Initial informations about bluff body (In real case a full scale 30 storey building without duct for wind energy) can be revealed from this picture. Upstream flow is completely prevented at the front wall where a part of the streamline is distinctly creating a separation zone at the upstream corner of the model near the test section surface. This separation zone appears like a horse shoe vortex (**Figure-4.16**) [40]. Rest of the streamlines are contracted while passing the top surface of the model. According to Bernoulli equation, high density of streamlines over the top surface of the model indicates high local pressure and flow velocity and low static pressure. Flow is highly influenced over the top surface where the height of the influenced flow is approximately same height as the model. Frontal sharp edge creates a large bump of the streamlines. Formation of random vortex over the top surface indicates higher degree of turbulence. Several phenomenon can be assumed from the complete absence of the streamlines behind the model [40]. Large recirculation of an arch vortex can exist behind the model wall at the back. Blurry turbulent eddies being re-circulated over the top surface which does not reattach. Due to the limitation of the spread of the laser illuminated area behind the model, the reattachment line can not be seen despite re-attaching which is clearly visible in the video taken from the real time flow.

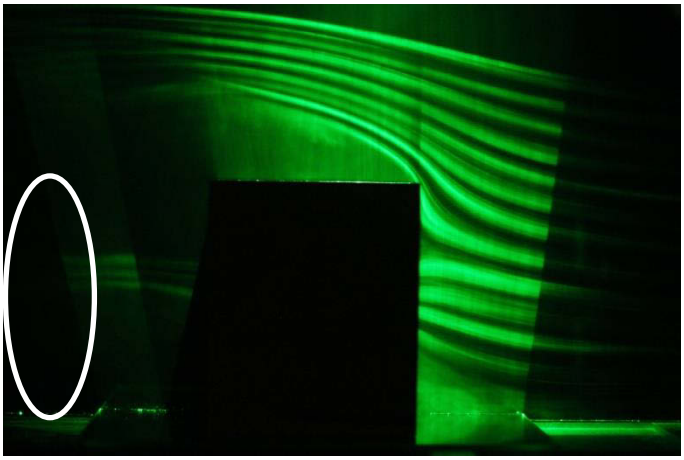

Figure-4.17. Flow visualization of M-1. (random horse shoe vortex marked in circle). Source: own representation.

4.7.2. Flow visualization (M-1)

Due to the similar exterior of all models, flow pattern around the outer walls of the model exhibits a similar flow pattern except the duct location. From **Figure-4.17**, there is a large diffusion below the inlet section of the duct of the model in upstream flow. This recirculated flow is the subsequent result of low pressure zone created by the model wall. Contraction of streamlines near duct inlet region indicates velocity increase and reduced pressure. Large amount of contraction exist at the front corner of the top surface due to sharp edges. The horse shoe vortex is created randomly at the end of the streamlines past outlet at the rear of the model. Visible streamlines passing the outlet shows less turbulence then M-2 and M-4. However, comparative flow visualization data for all models indicates less turbulence for uniform circular duct pattern.

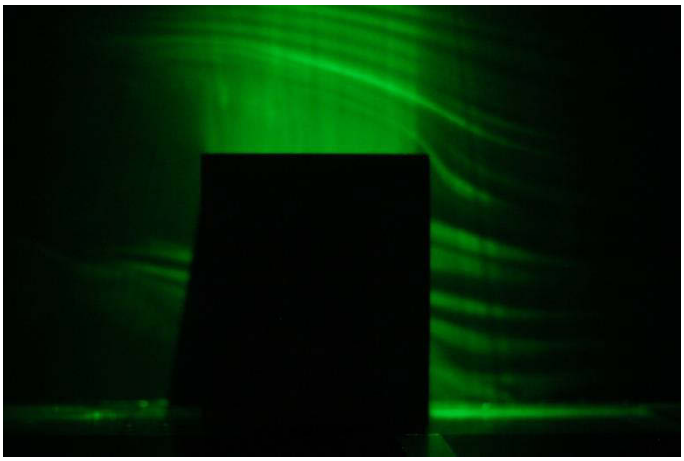

Figure-4.18. Flow visualization of M-2. Source: own representation.

4.7.3. Flow visualization (M-2)

Figure-4.18 exhibit the flow pattern for M-2. Larger inlet area of the duct reduces the contraction of streamlines at the duct inlet which obviously show less velocity and higher static pressure at the duct inlet. But higher degree of diffusion both at inlet and outlet also indicates high turbulence in the duct compared to M-1 and M-3. Random generation of vortices of different size indicates high level of flow mixing at the rear of the model.

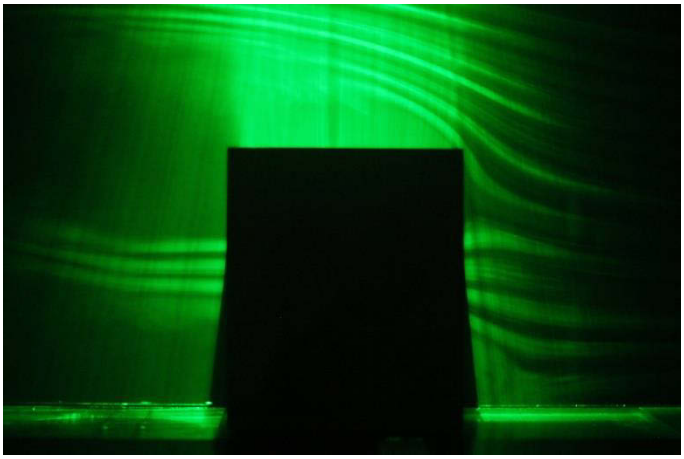

Figure-4.19. Flow visualization of M-3. Source: own representation.

4.7.4. Flow visualization (M-3)

From **Figure-4.19** it appears that the flow pattern is similar to the M-1. However, large bump over the top has much higher frequency of random eddy generation. Flow streamlines are much turbulent in nature then M-1 at inlet and outlet. Wake region of the flow through the duct is generated earlier then the M-1. Outlet jet has similar pattern to the M-1 but with high rate of diffusion then M-1.

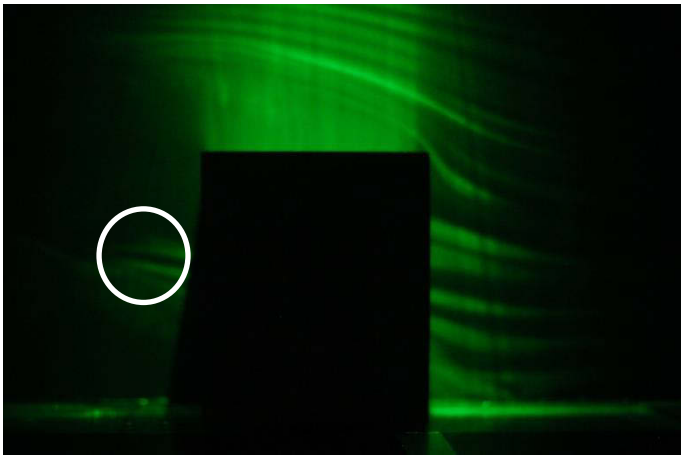

Figure-4.20. Flow visualization of M-4. (oblique flow). Source: own representation.

4.7.5. Flow visualization (M-4)

Figure-4.20 depicts high rate of diffusion of the streamlines at the inlet. This is also an indication of less inlet velocity then M-1 and M-3 due to the large intake area. Wake region behind the model is fully turbulent in nature. Outlet jet indicates an oblique flow (**Figure-4.20**) towards the suction created at the top of the model with very large and random eddies. Thus a certain conclusion can be made that the outlet jet is highly diffused with higher turbulence then any other model.

Certain conclusion can be made from flow visualization in terms of inlet and outlet velocity of M-1,2,3 and 4, rate of turbulence at the inlet and outlet, degree of suction and creation of random eddies at the wake region at the downstream flow past the models. However, for this experiment, velocity and level of turbulence is of particular interest. We can also determine the level of mixing in the duct from the flow pattern of the outlet jet. As stated above analysis, we can conclude that stretch of uniform diameter along the duct (example M-1 and M-3) is the prime factor obtaining lesser degree of turbulence then the duct shape with converged inlet and diverged outlet (example M-2 and M-4).

4.8. Calculation methodology

4.8.1. Velocity calcualtion

The mean velocity of the flow in these locations (location-1,2 and 3) are required for wind velocity analysis. LDA can measure only the longitudinal and vertical component of the instantaneous velocity in 3 axis cartesian co-ordinate of the recorded data. These components are expressed as $u_x(t)$ and $u_y(t)$ [39]. The mean velocity of these axis are marked as $\overline{u}_x$ and $\overline{u}_y$. The vector sum of $\overline{u}_x$ and $\overline{u}_y$ is expressed as $\overline{u}$ and can be defined as [39]:

$$\overline{u} = \sqrt{(\overline{u}_x + \overline{u}_y)} \qquad \text{[Eq-4.8]}$$

$\overline{u}_x = \frac{1}{T}\int u_x\,(t)\,dt$ and $\overline{u}_y = \frac{1}{T}\int u_y\,(t)\,dt$

4.8.2. Turbulence calculation

For turbulent velocity fluctuation analysis, LDA technique also measure longitudinal and vertical component of turbulent velocity fluctuation in 3 axis Cartesian co-ordinate, namely u_x' and u_y' which is obtained from the equations below:

$u_x(t)=\overline{u}_x+ u_x'(t)$ and $u_y(t)=\overline{u}_y+ u_y'(t)$ [Eq-4.8]

$u_x'(t)= u_x(t)- \overline{u}_x$ and $u_y'(t)= u_y(t)- \overline{u}_y$

Overall turbulence intensity (I) for the measurement position was calculated from the equation below

$$I \equiv \frac{\sqrt{u'_x{}^2+u'_y{}^2}}{\bar{u}} \qquad \text{[Eq-4.9]}$$

4.9. Flow quality and turbulence intensity profile in wind tunnel

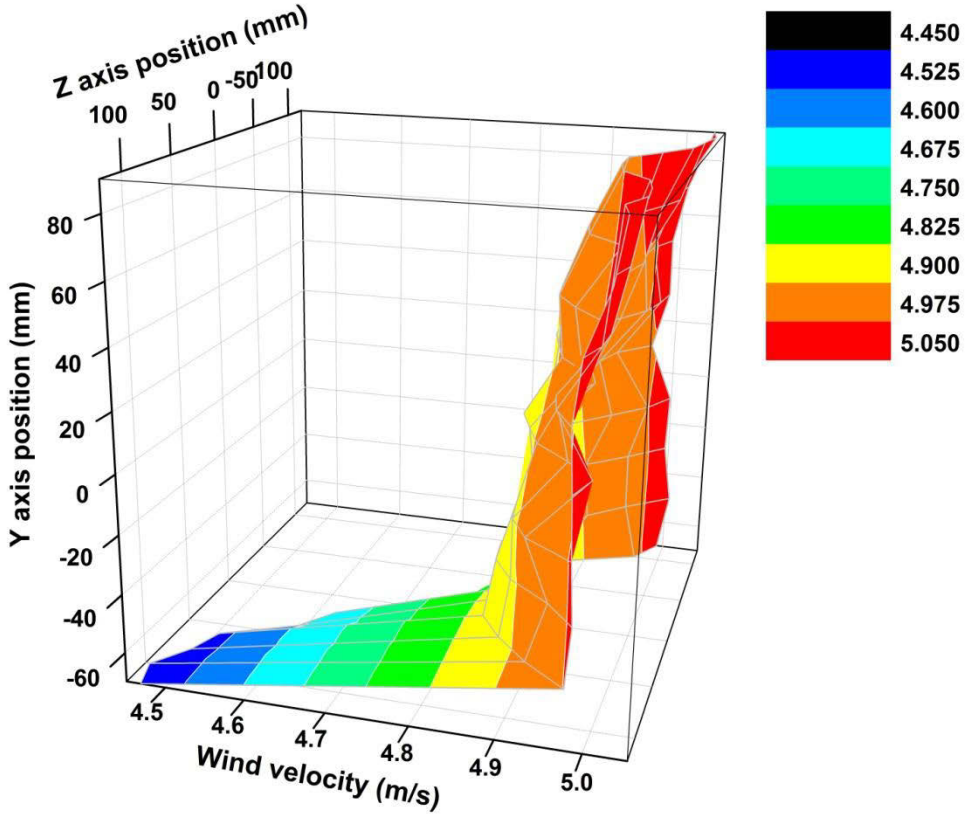

Figure-4.21.Velocity profile of free stream flow near the surface of wind tunnel. Source: own representation.

To asses the flow property, a LDA measurement was carried out at the lower surface of the test section keeping the flow completely uninfluenced (Without any obstacle present in the test section). A flow with 5 m/s velocity was applied and measured in a perpendicular plane along the span of the section (Location-2, Section-4.6.2). Plane dimension was 0.2 m in width and 0.16 m in height. 3D surface projection of the velocity profile along this plane is represented in the **Figure-4.21** . From this figure existence of a very thin boundary layer of approx 2.67 % of the total model height is observed (See **Figure-4.21**).

4.9.1. Deviation of real scale atmospheric boundary layer

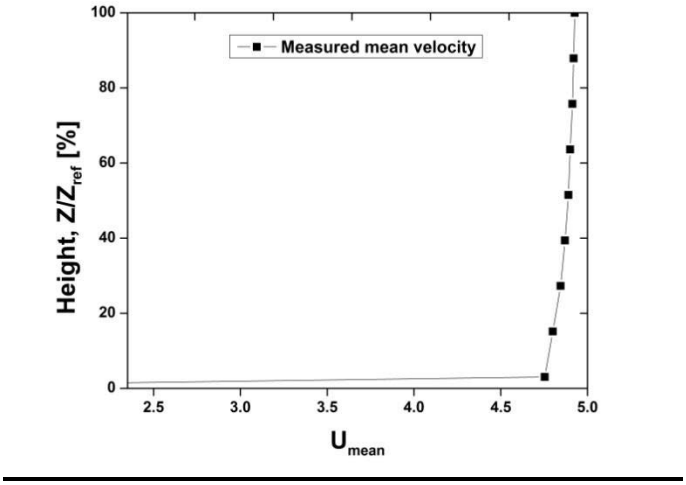

Figure-4.21. Mean velocity profile at wind tunnel (wind tunnel experiment). Source: own representation.

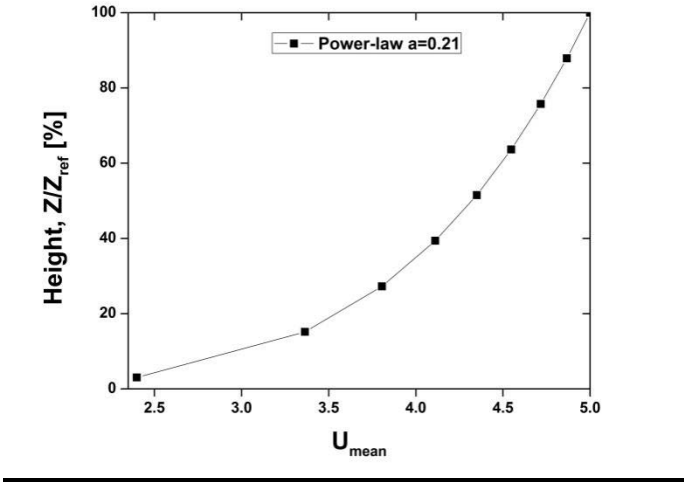

Figure-4.22. Atmospheric boundary layer profile (Power law) in real scale flow. Source: own representation.

As stated before, this is an aerodynamic wind tunnel where the boundary layer profile at location-1 (5 m/s) velocity appears as shown in **Figure-4.21**. This profile is a complete contrast to the real scale boundary layer for 30 m height for real scale buildings (**Figure-4.22**). For aerodynamic roughness length (Z_O) 0.6 m, where roughnesss class is below 3.5 (Figure-Chapter-2, section-2.4.1) the power law exponent should be between 0.20 to 0.23 [38]. Mean velocity profile upto model height for atmospheric bounday layer according to power law is represented in **Figure-4.22**. Comparing the mean velocity profile according to power law and actual mean velocity profile at this wind tunnel, it can be decided that the wind tunnel settiing does not represent the scaled atmospheric boundary layer. Reference height was set for the

building height [38]. According to power-law equation, the reference height (z_{ref}) and the mean wind velocity at this height ($\bar{u}_{ref}$) are set as building height (Eq-2.1,Chapter-2, Section-2.3.1).

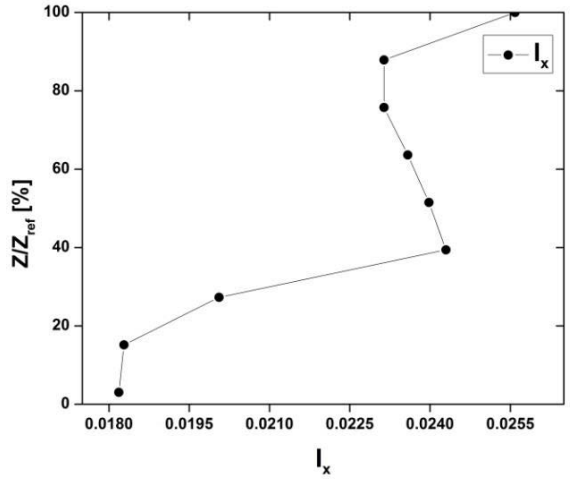

Figure-4.23. Profile of longitudinal turbulence intensity [%] in wind tunnel experiment. Source: own representation.

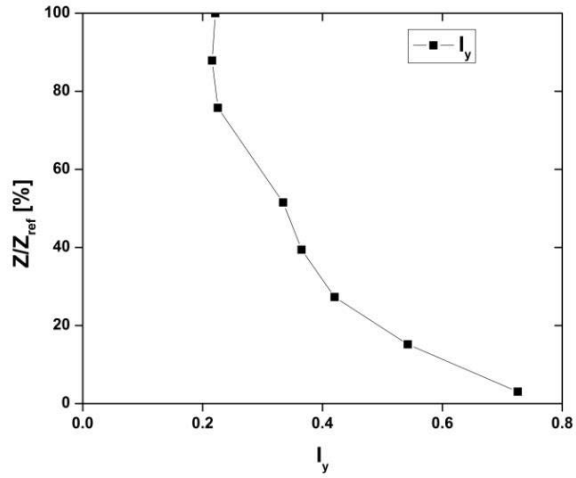

Figure-4.23. Profile of vertical turbulence intensity [%] in wind tunnel experiment. Source: own representation.

Turbulence intensity at the location-1 was also calculated without the model for turbulence analysis. The turbulence intensity profiles in wind tunnel experiment are checked before calculating the turbulence intensity at location-1 with the effect of the models present. **Figure-4.22** and **4.23** shows the profile of longitudinal and vertical turbulence intensity in wind tunnel experiment respectively. Longitudinal turbulence (I_x) ranges from 0.018% to 0.02% from the surface of the test section till a vertical distance of 0.16 m at the location-1. On the other hand, vertical turbulence intensity (I_y) exhibits a parabolic profile with decreasing magnitude as the

measurement location reaches 100% model height with a maximum value from 0.72% to 0.21%.

4.10. Velocity profiles at Location-1

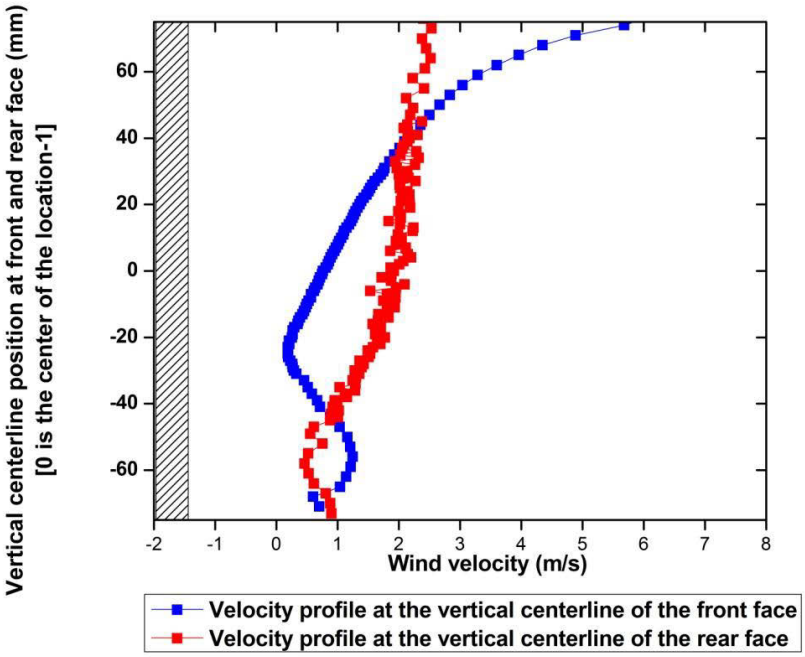

Figure-4.24. Velocity profile at the front and rear face vertical centreline (Location-1) of M-0. Source: own representation.

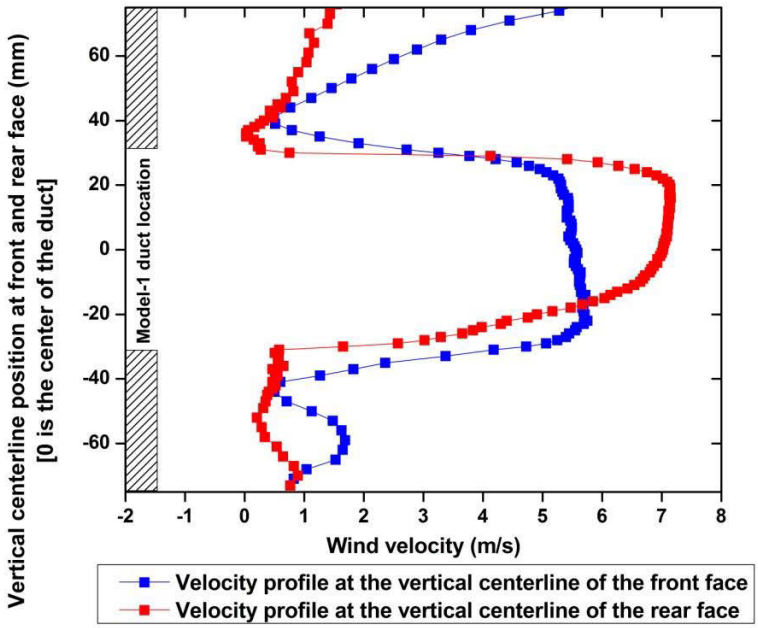

Figure-4.25. Velocity profile at the front and rear face vertical centreline of M-1. Source: own representation.

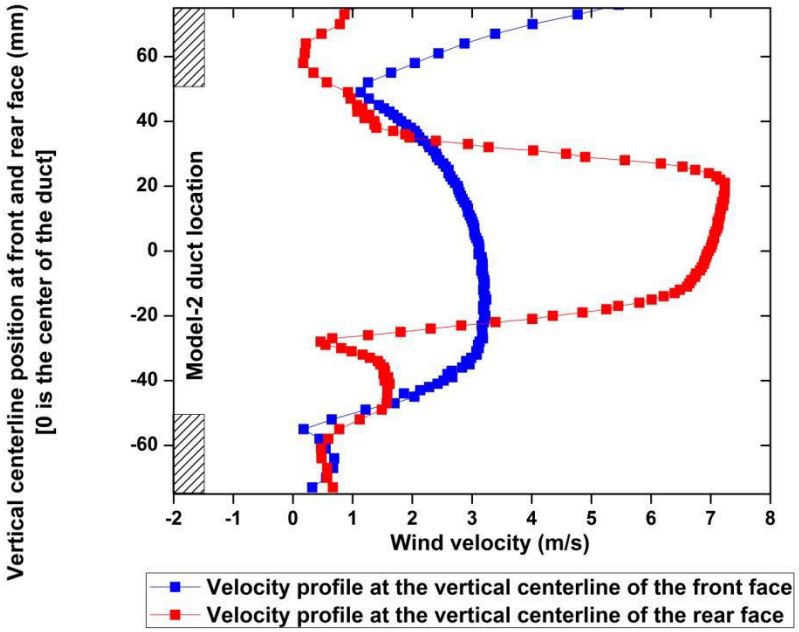

Figure-4.26. Velocity profile at the front and rear face vertical centreline of M-2. Source: own representation.

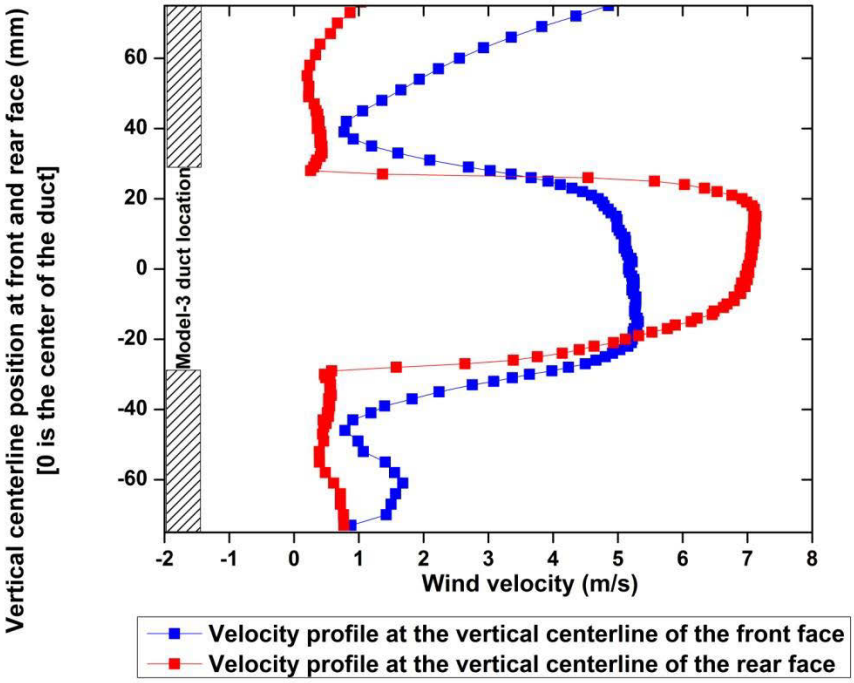

Figure-4.27. Velocity profile at the front and rear face vertical centreline of M-3. Source: own representation.

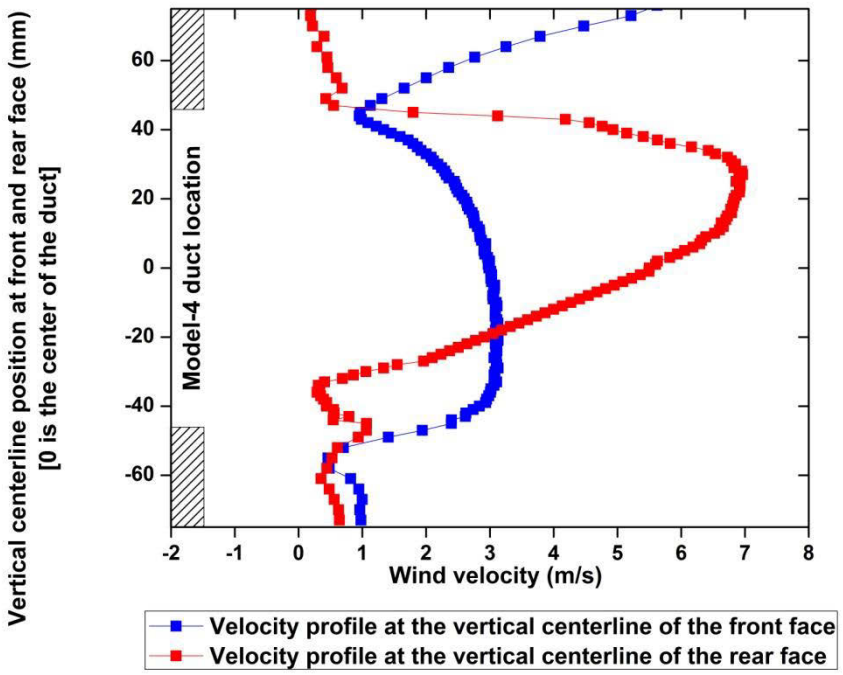

Figure-4.28. Velocity profile at the front and rear face vertical centreline of model-4. Source: own representation.

From **Figure-4.24**. it is visible that velocity profile at locatio-1 for M-0 remains within 0.19 m/s to 6.18 m/s. Velocity profile close to top surface of the M-0 at upstream location-1 have higher values than the downstream velocity profile as expected due to the contraction of the flow. Velocity profile at downstream location-1 have very high turbulent fluctuation (**Figure-4.24**). M-1 and M-3 has gradual increment and very uniform velocity profile at the inlet reaching maximum velocity 5.69 m/s and 5.31 m/s respectively (**Figure-4.25** and **4.27**). M-1 and 3 also have a very similar velocity profile at the outlet showing higher velocity at the upper half of the duct reaching maximum velocity of 7.15 m/s and 7.13 m/s respectively (**Figure-4.25** and **4.27**). M-2 and M-4 showed almost similar velocity profile at the inlet reaching a maximum velocity of 3.23 m/s and 3.13 m/s. M-2 has a uniform distribution of gradual increment of velocity at the outlet jet (**Figure-4.26**) where as model-4 has a very sharp changes of profile at the outlet jet (**Figure-4.28**). Maximum, minimum and mean velocity obtained from the location-1 for M-1, M-2, M-3 and M-4 are shown in Table-4.1. Mean velocity at the duct inlet and outlet is calculated from this data. Thus, theoretically available wind power at the duct is then obtained using **Equation-4.8**.

Model	Location	Max Velocity, U_{max} [m/s]	Min Velocity, U_{min} [m/s]	Mean Velocity, U_{mean} [m/s]
model-1	inlet	5.69	2.72	5.34
	outlet	7.15	0.27	5.95
model-2	inlet	3.23	1.14	2.61
	outlet	7.24	0.46	4.18
model-3	inlet	5.31	3.03	4.94
	outlet	7.13	0.26	6.12
model-4	inlet	3.13	0.95	2.66
	outlet	7.00	0.29	4.02

Table-4.1. Maximum, minimum and mean velocity obtained at the location-1 at the inlet and outlet for M-1,2,3 and 4. Source: own representation.

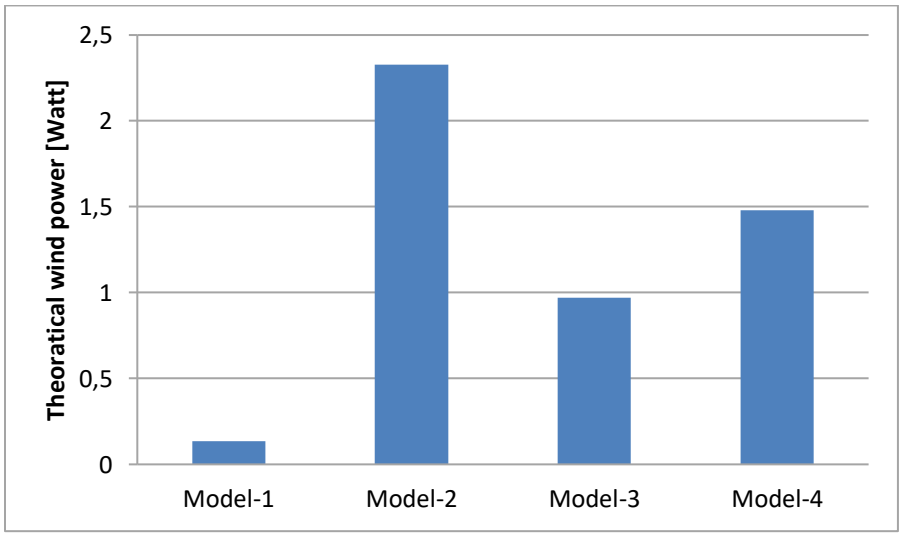

Figure-4.29. Comparison of theoretical wind power obtained at the duct for different models. Source: own representation.

From **Figure-4.29.** M-2 has the highest wind power yield from the experimental data of all models. However, M-4 has 67.76% higher intake area then model-3 but only 34.48% higher energy yield in terms of theoretical wind power available. We can conclude that M-2 geometry has better efficiency in terms of energy yield from building integrated duct out of all models. However, among the duct geometry between M-1 and M-3, both these models have almost same duct area where as the energy yield from M-3 is 0.9692 W which is 7.18 times higher then the energy yield from M-1 duct. Thus, we can conclude that among M-1 and 3 duct geometry,

rectangular duct geometry can obtain higher energy yield in terms of theoretically available wind power.

4.11. Turbulence result-Location-1

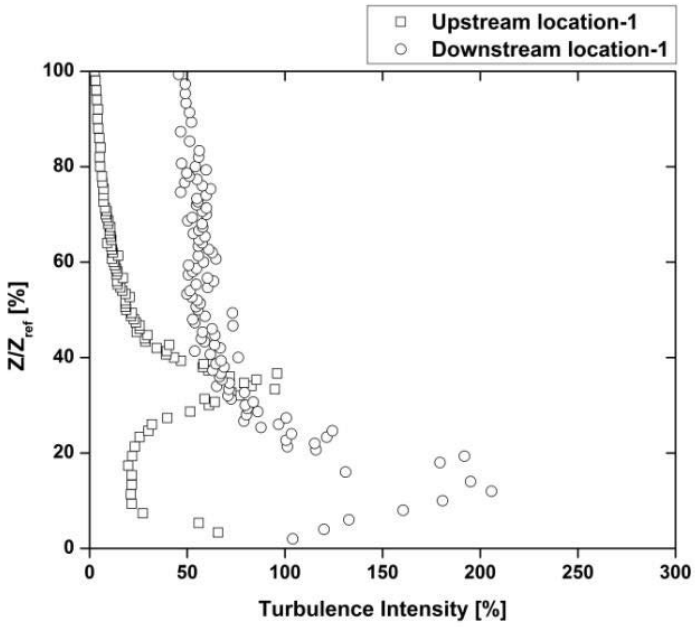

Figure-4.30. Turbulence Intensity [%] at location-1 of M-0. Source: own representation.

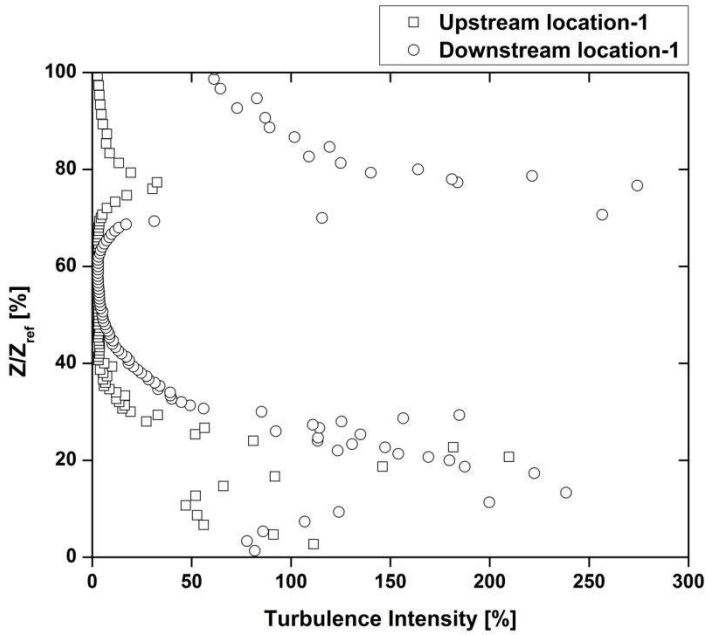

Figure-4.31.Turbulence Intensity [%] at location-1 of M-1. Source: own representation.

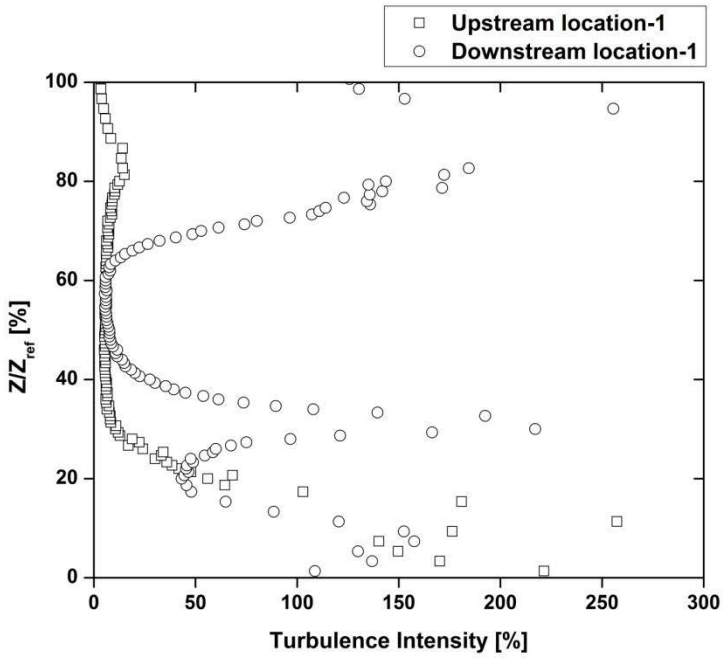

Figure-4.32. Turbulence Intensity [%] at location-1 of M-2. Source: own representation.

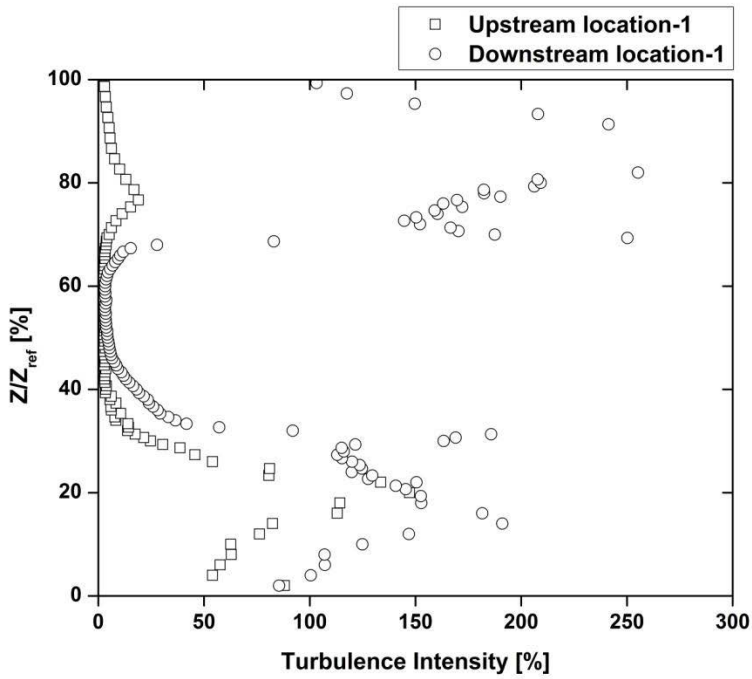

Figure-4.33.Turbulence Intensity [%] at location-1 of M-3. Source: own representation.

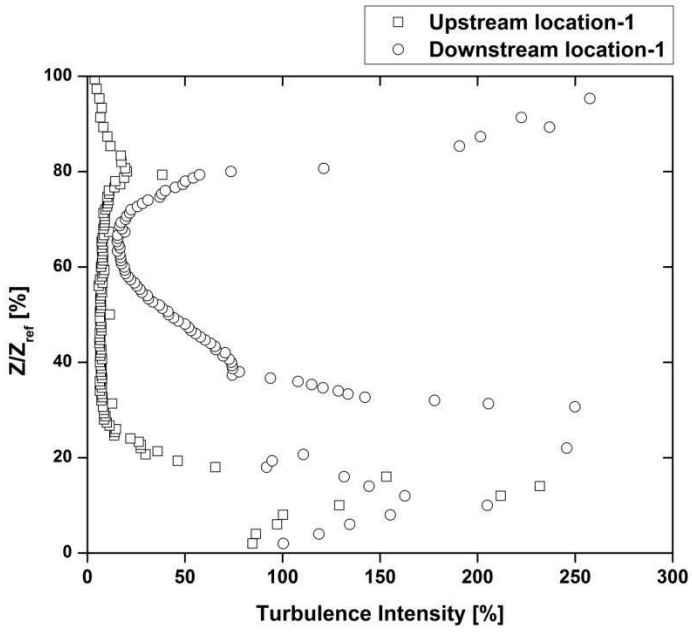

Figure-4.34.Turbulence Intensity [%] at location-1 of M-4. Source: own representation.

Change of surface orientation parallel to the free stream wind direction increases turbulence intensity. Analyzing the turbulence intensity from **Figure-4.31,4.32,4.33** and **4.34** (Turbulence intensity for the models with duct), it is evident that duct wall parallel to wind direction reduces turbulence at the inlet and outlet flow as it is evident from the Turbulence intensity values calculated for M-1 and M-3 (**Figure-4.31** and **4.33**). In both of these cases Turbulence intensity remains almost identical at the upstream and downstream measurement position. Converging inlet design for M-2 and M-4 exhibit almost no changes in Turbulence intensity values at location-1. But diverging outlet contributes significant increase in Turbulence intensity at downstream measurement point of location-2 (**Figure-4.32** and **4.34**). Upstream area below the duct location has random changes in turbulence intensity values as addressed in the flow visualization section (Section-4.7) due to the visible diffusion. From this analysis, we can conclude that uniform cross sectional area of the duct geometry can help reducing turbulent mixing of the flow inside the duct. This criteria is very important in terms of extracting energy in built environment through wind turbines as turbulent fluctuation reduces energy output and total life of the turbines.

4.12. Velocity profiles at location-2

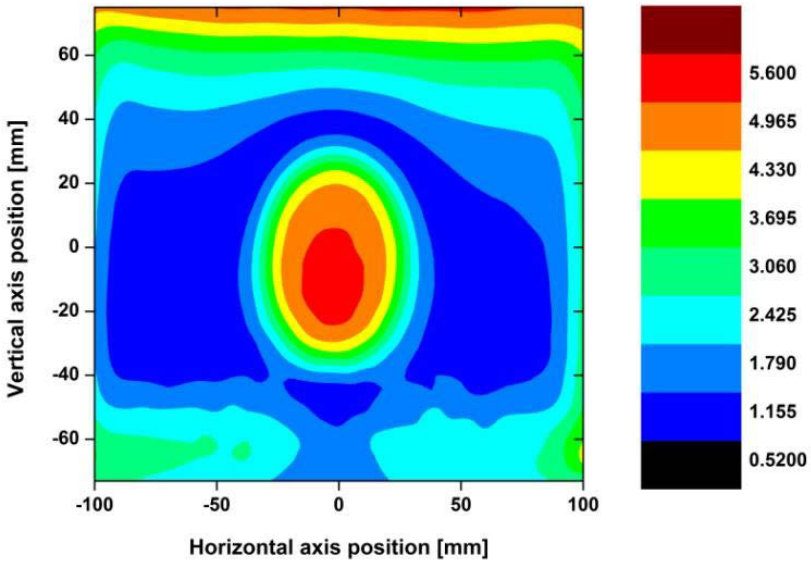

Figure-4.35. Mean velocity contour plot at front face of M-1.(Location-2). Source: own representation.

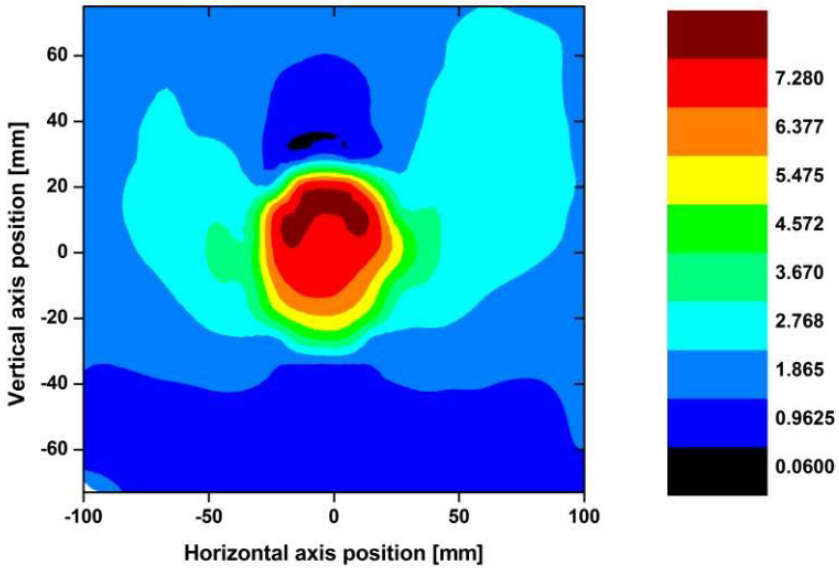

Figure-4.36. Mean velocity contour plot at rear face of M-1.(Location-2). Source: own representation.

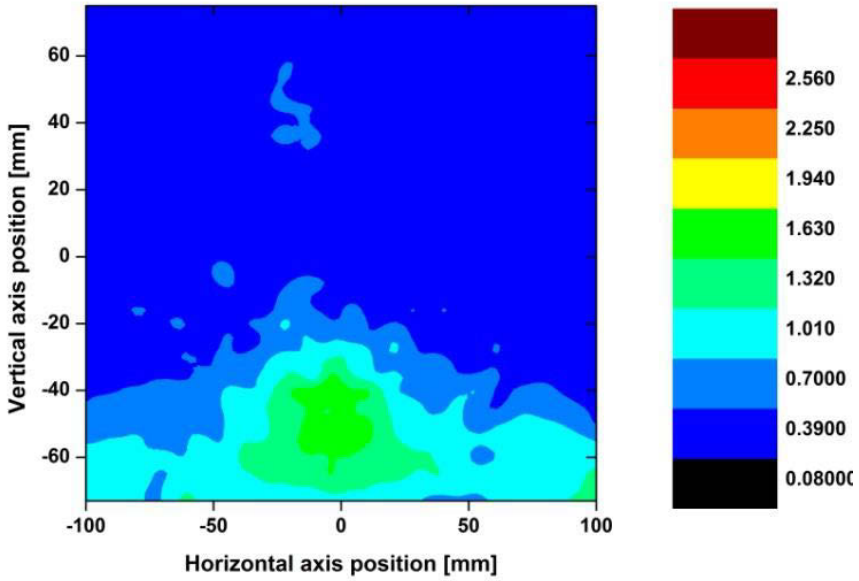

Figure-4.37. Turbulent velocity fluctuation contour plot at front face of M-1.(Location-2). Source: own representation.

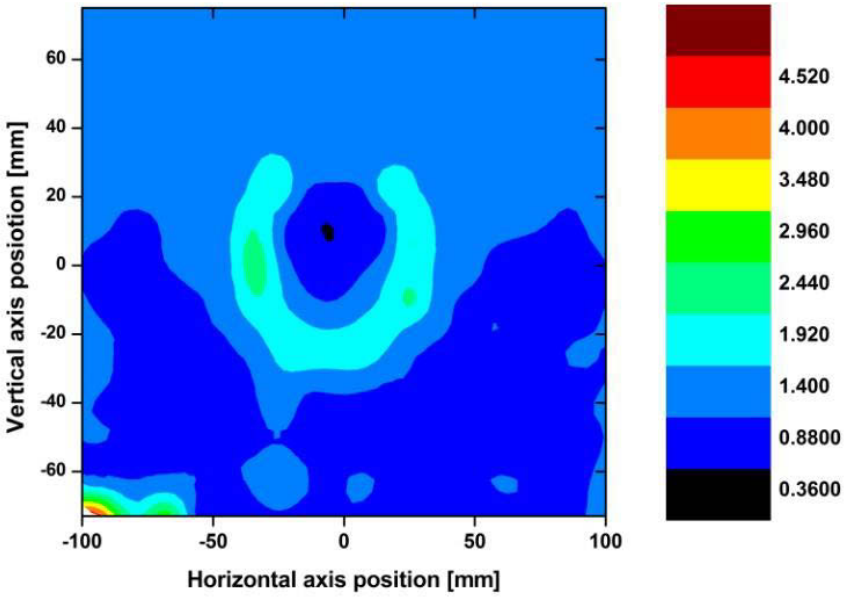

Figure-4.38. Turbulent velocity fluctuation contour plot at rear face of M-1.(Location-2). Source: own representation.

M-1 has of maximum velocity of 5.6 m/s and minimum velocity of 0.52 m/s at the location-2 of the inlet face. Highest velocity is distributed in the circular region of the inlet. On the other hand,

outlet jet reaches a maximum velocity of 7.28 m/s and a minimum of 0.06 m/s (**Figure-4.36**). M-1 has a maximum turbulent velocity fluctuation (U_{rms}) of 2.56 m/s and minimum of 0.08 m/s at the inlet face where as the outlet face has maximum turbulent velocity fluctuation (U_{rms}) of 4.52 m/s and minimum value of U_{rms} = 0.36 m/s (**Figure-4.28**). Most of the turbulent flow is located at the lower half of the inlet face. At the rear face, turbulent velocity fluctuation reaches its maximum in a horse shoe shape at the outlet location of the M-1, Which indicates an upward swirl of the flow (Flow visualization,**Figure-4.17**).

M-3 has achieved maximum and minimum inlet velocity of 4.98 m/s and 1.12 m/s respectively at the location-2 of the inlet face (**Figure-4.39**). Outlet jet obtain maximum and minimum velocity of 7.26 m/s and 1.56 m/s respectively. Higher flow velocity region is located at the duct outlet (**Figure-4.40**). Turbulence intensity distribution at the inlet face has maximum and minimum value of 1.51% and 0.02% respectively (**Figure-4.41**). Outlet face has a maximum and minimum turbulence intensity of 6.1% and 0.02and respectively (**Figure-4.42**). M-3 has higher turbulent region at the outlet face then the M-1.

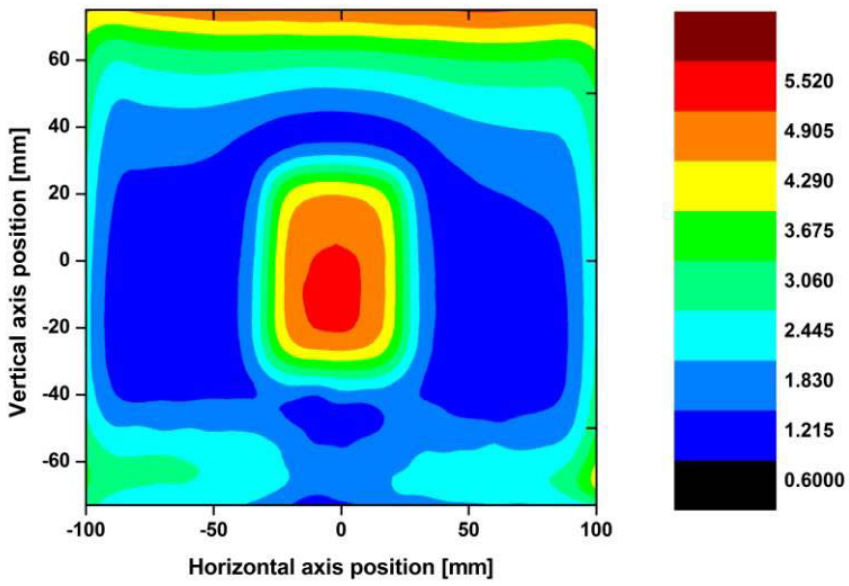

Figure-4.39. Mean velocity (U_{mean}) contour plot at front face of M-3.(Location-2). Source: own representation.

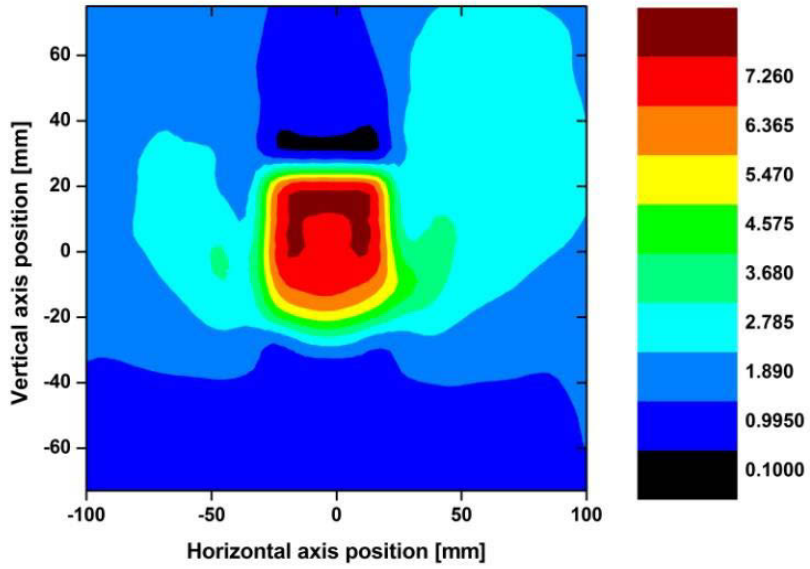

Figure-4.40. Mean velocity (U_{mean}) contour plot at rear face of M-3.(Location-2). Source: own representation.

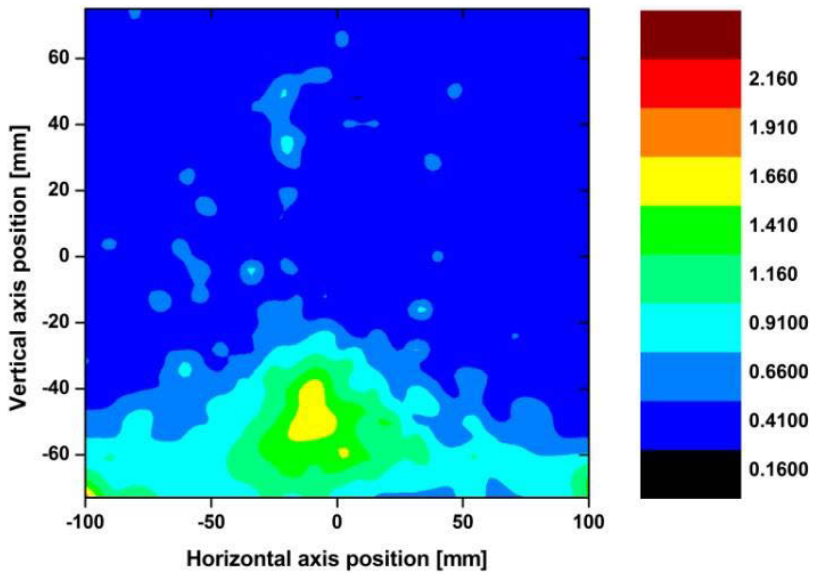

Figure-4.41. Turbulent velocity fluctuation contour plot at front face of M-3.(Location-2). Source: own representation.

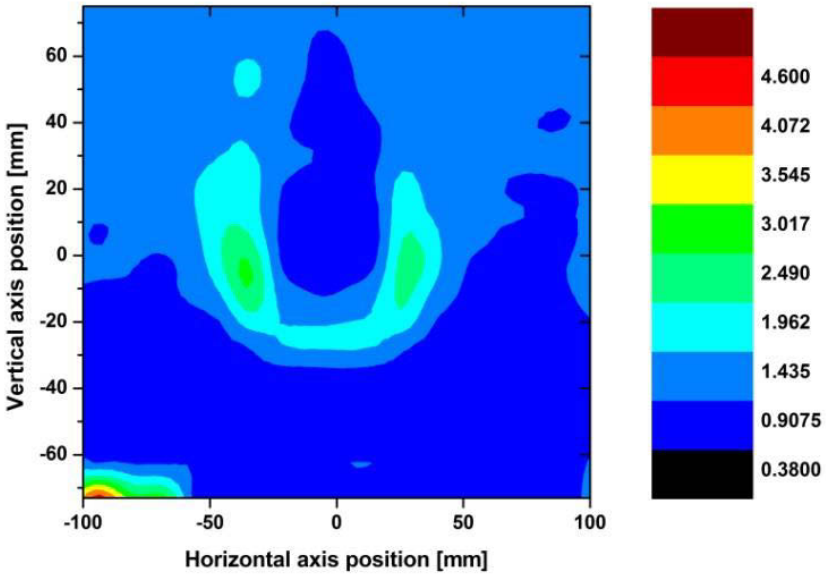

Figure-4.42. Turbulent velocity fluctuation contour plot at rear face of M-3.(Location-2). Source: own representation.

4.13. Velocity profiles at location-3

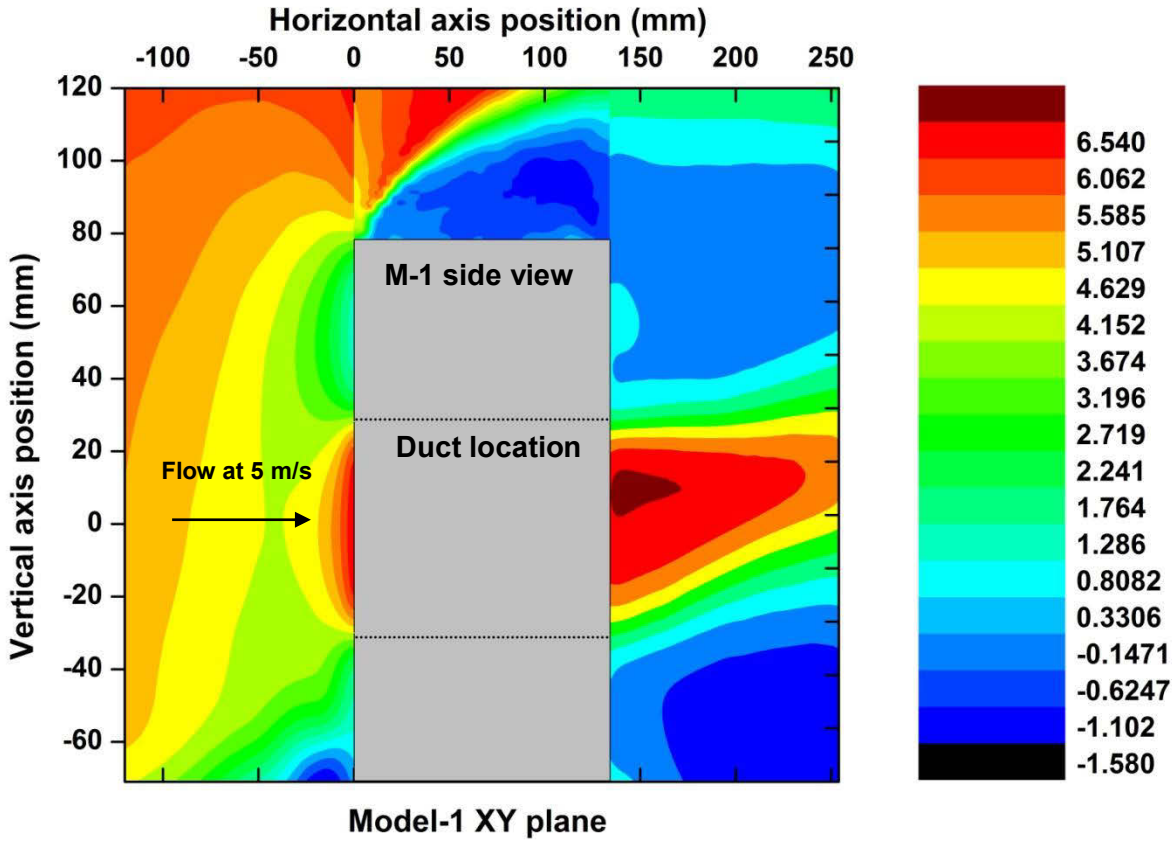

Figure-4.43. Mean velocity (U_{mean}) contour plot at rear face of M-3.(Location-3, side view). Source: own representation.

Figure-4.43 represent the M-1 velocity measured at location-3 at 5 m/s incident flow. Here, upstream flow at inlet has an accelerated velocity 6.54 m/s and downstream flow past outlet reaches a velocity of 7.15 m/s. Flow separation occurred at the upstream sharp edge near the roof of the model. From 0.055 m above the roof to 0.085 m there is a clear indication of a parabolic layer of the flow, containing an accelerated velocity of 6.15 m/s.

5. Computational Fluid Dynamics

5.1. Computational Fluid Dynamics

It is impossible to deny the importance of wind tunnel simulation and the accuracy of the result obtained from it. But in reality, it is quite impossible to obtain a detailed experimental data in the field of building aerodynamics. Thus, Computational Fluid Dynamics (CFD) performs an essential role to provide us the detailed information on the large domain of buildings and its associated flow. According to John D Anderson, Jr -"Computational Fluid Dynamics (CFD) is the art of replacing the integrals or the partial derivatives (as the case may be) in the Navier-Stokes equations by discretized algebraic forms, which in turn are solved to obtain numbers for the flow field values at discrete points in time and/or space" [41]. This is a tool which allows us to solve fluid flow problems that do not have known analytical solutions and can not be solved any other way. CFD has been very widely used in the field of wind energy. As a part of that legacy to visualize, analyze and estimate wind energy potential in urban environment, we have used CFD tool to predict flow behaviour in the experimental environment. Accepting the fact that measurement obtained from a real scale building integrated duct would be much more accurate and would give us better predictions in terms of real scenario and energy obtained, but which would be a hectic approach in reality considering the time constraints and financial aspects for this project. However, for an accurate prediction for appropriate designs of the duct, CFD can predict as much accurate result as better modelling we can perform. It is important to obtain an elaborate array of informations on the complete flow field for a decisive purpose to select an optimized duct geometry.

CFD is a viable option to obtain such data for following characteristics. It is comparatively inexpensive and require less time for data measurement then wind tunnel experiment. Through CFD we can get the complete flow field data i.e. all related parameters required to analyze the whole computational domain which would be very time consuming to obtain through wind tunnel simulation. This method can also overcome the limitations of similarity parameters (Chapter-4, subchapter-4.6) which is required for wind tunnel simulation. The problem is that many flows require several dimensionless parameters for their specification and it may be impossible to set up an experiment which correctly scales the actual flow [42]. As an example in reality it is quite impossible to obtain the real scale Reynolds number of the flow in wind tunnel which can be pretty much accurately simulated with CFD tool. Although having few limitations about accuracy and reliability of CFD data, on the contrary with better modelling and accurate approximation, which is possible to optimize. We have obtained data from wind tunnel simulation which was used for validation of CFD data. As a part of this experiment, 2D numerical simulation of the

wind tunnel flow field for a wider range of data was performed according to the best practice guidelines in simulating flow related to building aerodynamics [43].

There are several codes for CFD simulation but individual code was selected on the requirements of the type of the flow appropriate to describe the situation for this experiment [44]. However, the criteria for the CFD program to be complied with the experimental scenario is very case specific. Building aerodynamics is a very special situation in terms of turbulent flow and the complexity that prevails in the numerical simulation of large domain of urban environment where modelling holds a very significant role.

5.2. Limitation of 2D simulation

Validation of numerical simulation results are only possible through the wind tunnel test. For wind tunnel measurement we have used Laser Doppler Anemometry (LDA) technique which is a non intrusive measurement technique (See chapter-3). This method of measurement allows us to obtain the longitudinal and vertical component of the velocity and turbulence. Thus, an appropriate validation is only possible through the 2D numerical simulation which obtain longitudinal and vertical velocity components. The accuracy of three cartesian coordinate component is the most appropriate result for turbulence research. However, due to the limitation of the wind tunnel measurement technique has confined us within the boundary of 2D numerical simulation.

5.3. Theory of CFD modelling

The wind tunnel simulation of the building model was simulated numerically with the help of CFD tool which is, in this case commercial software ANSYS v15.0. As a part of the modelling package, all three requirements of a basic CFD operation namely pre processing, solution (solver) and post processing can be performed with this package. In this chapter, overall steps that had been followed to perform the numerical simulation of this experiment is described as follows [43].

Pre-processing

- Selection of target variable (In this experiment-velocity)
- Selection of the approximate equations describing the physics of the flow
- Selection of the model geometry
- Selection of the computational domain
- Selection of the boundary condition
- Discretization i.e. generation of computational grid

Solution

- Initialization of the flow field

- Selection of numerical approximations and solution algorithms
- Selection of the convergence criteria

Post processing

- Visualizing and analyzing data
- Verification and validation

5.4. Pre-processing

Pre-processing of CFD modelling consists of several phases. Selection of target variable are important in terms of result oriented approach of CFD modelling. For this research, velocity is the prime objective to measure from CFD simulation. As stated in Chapter-4, model layout and measurement location section, velocity is the prime determinant to asses the wind energy potential in the urban environment (See **Equation-4.7**).

Selection of the appropriate equations describing the physics of the flow depends on the type of flow to be simulated. We have obtained data from wind tunnel experiments from the target models which we can use to validate the data obtained from CFD simulation. It was required to check the whole flow field information of the wind tunnel from CFD data for better validation of the result. The most important measurements at the duct could not be carried out which is the most important data position to be measured in this experiment. The same Reynolds number flow that has been obtained in the wind tunnel was generated in the numerical simulation e.g. $1.8 \cdot 10^5$ (Chapter-4, Section-4.5.2). This high value of Reynolds number clearly indicates a turbulent flow to be simulated which require a very precise decision about an appropriate turbulence model.

Navier-Stokes equation: CFD can only solve the Navier-Stokes equation in a discretized flow field. As the equations can not be solved analytically, numerical method has to adopt solving the equations iteratively. The actual instantaneous Navier-Stokes equation for a confined, incompressible flow of a Newtonian fluid in cartesian coordinates is as follows [47]:

$$\frac{\partial u_i}{\partial x_i} = 0 \qquad \text{[Eq-5.1]}$$

$$\frac{\partial u_i}{\partial t} + u_j \frac{\partial u_i}{\partial t} = -\frac{1}{\rho}\frac{\partial p}{\partial x_i} + \frac{\partial}{\partial x_j}(2\upsilon S_{ij}) \qquad \text{[Eq-5.2]}$$

$$S_{ij} = \frac{1}{2}\left(\frac{\partial u_i}{\partial x_j} + \frac{\partial u_j}{\partial x_i}\right) \qquad \text{[Eq-5.3]}$$

$$\frac{\partial \theta}{\partial t} + u_j \frac{\partial \theta}{\partial x_j} = \frac{1}{\rho C_p}\frac{\partial}{\partial x_j}\left(k\frac{\partial \theta}{\partial x_j}\right) \qquad \text{[Eq-5.4]}$$

$$\frac{\partial C}{\partial t} + u_j \frac{\partial C}{\partial x_j} = \frac{\partial}{\partial x_j}\left(D\frac{\partial C}{\partial x_j}\right) \qquad \text{[Eq-5.5]}$$

Where, u_i is the instantaneous velocity, x_i is the instantaneous position, p is the instantaneous pressure, θ is the instantaneous temperature, t is the time, ρ is the density, ν is the molecular kinematic viscosity, C_p is the specific heat capacity, k is the thermal conductivity, S_{ij} is the strain rate tensor, C is the instantaneous concentration and D is the molecular diffusion co-efficient. Above mentioned equations have 6 components which indicates a closed system. These instantaneous components of **Equation-5.1, 5.2, 5.3** and especially **5.1** can be decomposed into mean and fluctuating components and time averaging of these equations give us the Reynolds averaged Navier-Stokes (RANS) equation. Then the equations can be expressed as follows.

$$\frac{\partial U_i}{\partial x_i} = 0 \qquad \text{[Eq-5.6]}$$

$$\frac{\partial U_i}{\partial t} + U_j \frac{\partial U_i}{\partial t} = -\frac{1}{\rho}\frac{\partial p}{\partial x_i} + \frac{\partial}{\partial x_j}\left(2\upsilon \frac{\partial U_i}{\partial t} s_{ij} - \overline{u_j' u_i'}\right) \qquad \text{[Eq-5.7]}$$

$$S_{ij} = \frac{1}{2}\left(\frac{\partial U_i}{\partial x_j} + \frac{\partial U_j}{\partial x_i}\right) \qquad \text{[Eq-5.8]}$$

$$\frac{\partial \Theta}{\partial t} + U_j \frac{\partial \Theta}{\partial x_j} = \frac{1}{\rho C_p}\frac{\partial}{\partial x_j}\left(k\frac{\partial \Theta}{\partial x_j} - \overline{u_j'\theta'}\right) \qquad \text{[Eq-5.9]}$$

$$\frac{\partial C}{\partial t} + U_j \frac{\partial C}{\partial x_j} = \frac{\partial}{\partial x_j}\left(D\frac{\partial C}{\partial x_j} - \overline{u_j' C'}\right) \qquad \text{[Eq-5.10]}$$

Equation-5.7, 5.9 and **5.10** represent Reynolds stresses, turbulent heat and turbulent mass fluxes subsequently which represent influence of turbulence on mean flow, heat and mass transfer .

Two main types of turbulence models can be distinguished, namely first-order closure model and second order closure model. First order closure model can be classified into Boussinesq eddy-viscosity hypothesis which relates the Reynolds stresses to the velocity gradient in the mean flow. Different components of the Boussinesq eddy-viscosity hypothesis are described as follows:

$$-\overline{u_i' u_j'} = 2\nu_t S_{ij} - \frac{2}{3}k\delta_{ij} \qquad \text{[Eq-5.11]}$$

$$S_{ij} = \frac{1}{2}\left(\frac{\partial U_i}{\partial x_j} + \frac{\partial U_j}{\partial x_i}\right) \qquad \text{[Eq-5.12]}$$

$$k = \frac{1}{2}\overline{u_i' u_j'} \qquad \text{[Eq-5.13]}$$

$$\delta_{ij} = \begin{cases} 1\ for & i = j \\ 0 for & i = j \end{cases} \qquad \text{[Eq-5.14]}$$

Here, $-\overline{u_i' u_j'}$ is the Reynolds stresses as function of velocity gradient in the mean flow, ν_t is turbulent viscosity, $S_{ij}$is the mean strain rate value of which is represented through **Equation-**

5.12. k is the turbulent kinetic energy value of which can be represented through **Equation-5.13**. $\delta_{ij}$is the Kronecker delta. Value of the Kronecker delta is given by the **Equation-5.14** [44].

There are number of turbulence models available as a derivatives of the Boussinesq eddy-viscosity hypothesis which are known as eddy viscosity models. Different eddy viscosity models are standard k-ε model, RNG k-ε model, realizable k-ε model, standard k-ω model and k-ω shear stress transport (SST) model [46]. k-ω shear stress transport (SST) model was selected for this experiment for the following reasons discussed below.

5.4.1. Physics of the k-ω shear stress transport (SST) model

"Which model is best for which kind of flows (none is expected to be good for all flows) is not yet quite clear, partly due to the fact that in many attempts to answer this question numerical errors played a too important role so clear conclusions were not possible In most workshops held so far on the subject of evaluation of turbulence models, the differences between solutions produced by different authors using supposedly the same model were as large if not larger than the differences between the results of the same author using different models" [42]. Selection of a specific turbulence model is quite difficult as "There is no turbulence model that is universally valid. Even minor changes in the geometry of the flow problem can change which turbulence model performs best. Turbulence model can only be evaluated after it has been shown that numerical errors are sufficiently small" [42]. "The shear-stress transport (SST) model was developed by Menter to effectively blend the robust and accurate formulation of the k-ω model in the near-wall region with the free-stream in dependence of the k-ω model in the far field. To achieve this, the k-ω model is converted into a k-ω formulation. The SST k-ω model is similar to the standard k-ε model, but includes the following refinements. These features make the SST k-ω model more accurate and reliable for a wider class of flows.(e.g. adverse pressure gradient flows, airfoils, transonic shock waves) than the standard k-ω model. These features make the SST k-ω model more accurate and reliable for a wider class of flows.(e.g. adverse pressure gradient flows, airfoils, transonic shock waves) than the standard k-ω model. The standard k-ω model and the transformed k-ε model are both multiplied by a blending function and both models are added together. The blending function is designed to be one in the near-wall region, which activates the standard k-ω model, and zero away from the surface, which activates the transformed k-ε model. The SST model incorporates a damped cross-diffusion derivative term in the ω equation. The definition of the turbulent viscosity is modified to account for the transport of the turbulent shear stress. The modelling constants are different." [46]

These features make the SST k-ω model more accurate and reliable for a wider class of flows (e.g. adverse pressure gradient flows, airfoils, transonic shock waves) than the standard k-ω model. Transport equations for SST k-ω turbulence models are as follows:

$$\frac{\partial}{\partial x}(\rho k)+\frac{\partial}{\partial x_i}(\rho k u_i)=\frac{\partial}{\partial x_i}(\Gamma_k \frac{\partial k}{\partial x_j}+ \widetilde{G_k} - Y_k + S_k) \quad \text{[Eq-5.15]}$$

$$\frac{\partial}{\partial x}(\rho\omega)+\frac{\partial}{\partial x_j}(\rho\omega u_j)=\frac{\partial}{\partial x_j}(\Gamma_\omega \frac{\partial \omega}{\partial x_j}) + G_\omega - Y_\omega + D_\omega + S_\omega \quad \text{[Eq-5.16]}$$

Near Wall modelling is an essential part of building aerodynamics. Turbulent flows are significantly affected by the presence of walls. The mean velocity field is affected through the no-slip condition that has to be satisfied at the wall. However, the turbulence is also changed by the presence of the wall in non-trivial ways. In near wall region, viscous damping reduces the tangential velocity fluctuations, while kinematic blocking reduces the normal fluctuations. Toward the outer part of the near-wall region, the turbulence is rapidly augmented by the production of turbulence kinetic energy due to the large gradients in mean velocity. The near-wall modelling significantly impacts the fidelity of numerical solutions, as walls are the main source of mean vorticity and turbulence. It is in the near-wall region that the solution variables have large gradients and the momentum and other scalar transports occur most vigorously. Therefore, accurate representation of the flow in the near-wall region determines successful predictions of wall-bounded turbulent flows [46].

The k-ω SST turbulence model is valid only for the turbulence core flow, not for the flow close to wall surfaces where no slip condition applies. Viscous effects are very significant close to the near wall region. There are two possible methods for modelling near wall flow in k-ω SST turbulence model namely wall function method and low Reynolds number modelling method. Low Reynolds number method was implemented for this experiment due to the fact that this method is highly accurate then wall function method for near wall turbulent flow. However, requirement for fine mesh in near wall region increases the requirement of higher computational power and computation time. In reality, low Reynolds number modelling has difficulty in obtaining accurate results for walls with higher surface roughness and for very high Reynolds number flow [46]. For higher degree of accuracy in numerical simulation flow near wall region has to be elaborated. According to numerous empirical result [46], The region very close to wall where viscous (molecular) effects dominate the flow are known as linear sublayer or viscous flow layer. Here the flow is almost laminar. Intermediate layer between the linear sub-layer and the log-law layer where viscous and turbulent effects are equally important is known as buffer layer. The last layer of the inner flow in the near wall region where inertial effects dominate over viscous forces is called the log-law layer(Figure-5.1.) [47].

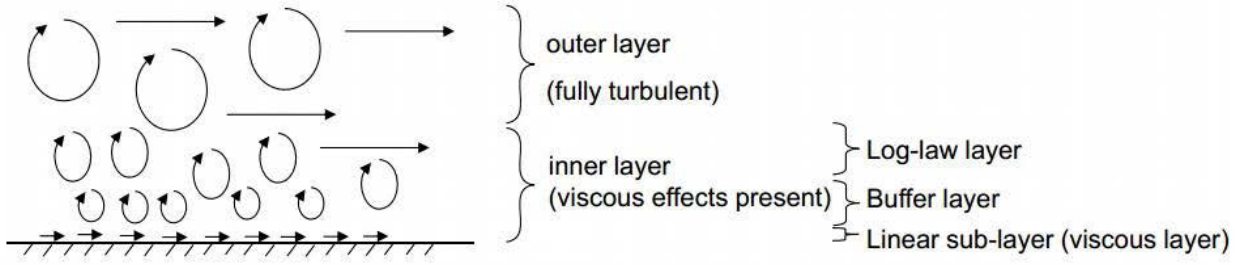

Figure-5.1. Structure of turbulent boundary layer in the near wall region. Source: [47].

Flow behaviour has different characteristics in these three different layers (**Figure-5.1**) in the near wall region which necessitates different modelling for these layers individually. Informations in terms of height and extent for each of these three layers are important in modelling low Reynolds number method. As such two dimensionless quantities are introduced. They are dimensionless wall unit (y^+) and dimensionless fluid speed (u^+) [47].

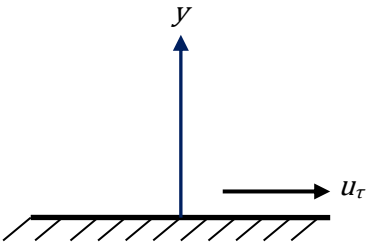

Figure-5.2. Wall unit (y)and friction velocity (u_τ). Source: based on [46]

Dimensionless wall unit, $y^+ = \frac{\rho y u_\tau}{\mu}$ [Eq-5.17]

Where, friction velocity (u_τ) is a variable that represent the magnitude of the velocity fluctuations in the wall bounded flow as a function of roughness, fluid speed and fluid density. Friction velocity (u_τ) can be expressed as the following equation (**Figure-5.2**) [47].

Friction velocity, $u_\tau = \sqrt{\frac{\tau_w}{\rho}}$, [Eq-5.18]

Where τ_w is the shear stress.

Dimensionless fluid speed, $u^+ = \frac{U_T}{u_\tau}$ [Eq-5.19]

Where U_T is the fluid speed tangential to wall.

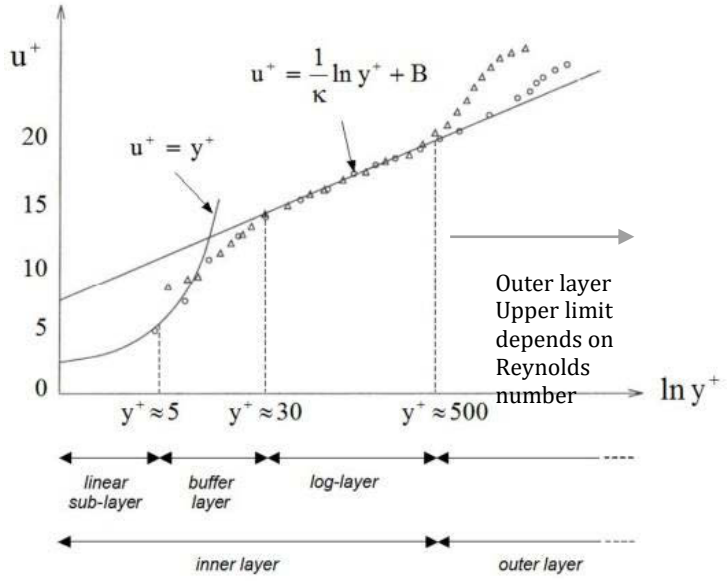

Figure-5.3. Sub-layers of near wall region and their corresponding $y^+$and u^+ values. Source: [46].

Low Reynolds number correction method damps the turbulent viscosity by co-efficient α^*. Damping of the $\alpha^*$is given by the equation [46].

$$\alpha^*=\alpha_\infty^*\left(\frac{\alpha_0^*+Re_t/R_k}{1+Re_t/R_k}\right) \quad \text{[Eq-5.20]}$$

Where,

$$Re_t=\frac{\rho k}{\mu\omega} \quad \text{[Eq-5.21]}$$

$$R_k=6 \quad \text{[Eq-5.22]}$$

$$\alpha_0^*=\frac{\beta_i}{3} \quad \text{[Eq-5.23]}$$

$$\beta_i=0.072 \quad \text{[Eq-5.24]}$$

$$\alpha^*=\alpha_\infty^*=1 \text{ (For high Reynolds number form of the k-ω model)} \quad \text{[Eq-5.25]}$$

According to some literature, it is preferable to obtain $y^+ \approx 1$. y^+ must be situated in linear sub-layer for a high accuracy of the numerical result [46][47]. y^+ value can only be determined after the simulation. Thus, determining y^+ is an iterative procedure [43][47]. y^+ value for all numerical simulations was obtained after whole iterative procedure. $y^+<1$ was found for each simulation. To obtain such minimal value of y^+ including high accuracy of numerical result for wall boundary layer, high resolution of grid normal to the wall is required for all near wall regions [46]. Minimum number of cells to determine a boundary layer (e.g. inner sub-layer) accurately is around ten to twelve are expected [46](**Figure-5.4**). In this experiment, 15 to 20 mesh refinement was followed in wall normal direction in all near wall region for all numerical simulation. Obtained y^+ value for all numerical simulation was found within the range of 0.95~1.

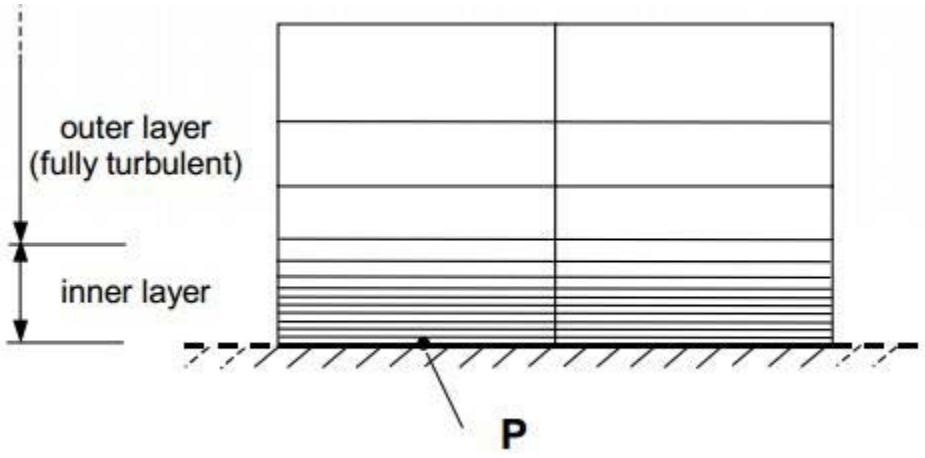

Figure-5.4. Mesh refinement in near wall region and preferable position of y^+ value. Source: [47]

5.4.2. Selection of the model geometry

Model geometry was kept according to the wind tunnel model scale. ANSYS has a built in design modeller which allowed us to design the 2D CAD models. To obtain an accurate flow field information, wind tunnel test section including the model dimension was used to design the flow field geometry with an scale of 1:1. There was two different approaches of flow domain modelling. The flow field in the wind tunnel with similar dimension was modelled in longitudinal side view and top view perspective (**Figure-5.5** and **5.6**). In this study 2D perspective of the wind tunnel test section was used as a computational domain. This was created with two approaches as mentioned above. For each model the computational domain should include 3 sections, upstream, central and downstream parts [48]. Inlet flow of a constant profile (aerodynamic flow) at 5 m/s is applied. Inlet flow profile and approach flow (flow travelling from the inlet plane to the building model) remain almost similar as observed in wind tunnel experiment. The incident flow (flow at the model location at computational domain) is influenced by the model wall and the change of flow is observed at the downstream part. It is recommended that inlet plane and outlet plane should have sufficient distance from the model [49]. It is such because inlet flow has to be developed completely before incident flow is influenced by the existence of the model and model integrated duct. Distance between the outlet plane and model has to be set according to the model height which is, in this case 0.15 m. Recommended distance between rear wall of the model and the outlet plane is 10 times the height of the model [50]. Appropriate distance in this case would be 1.5 m. However, actual distance between outlet plane and the model rear plane is 1.1375 m in the computational domain. It is because at 5 m/s flow remain quite undisturbed after 0.8 m at downstream part. To stretch the computational domain up to 10 times the model height would result in unnecessary utilization of computational resource and subsequent increase in computational time.

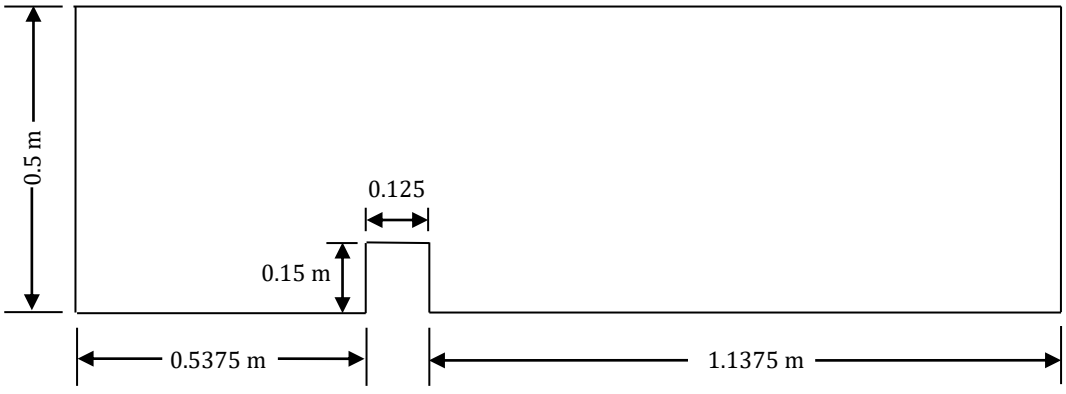

Figure-5.5. Geometry of computational domain for M-0 at side view approach. Source: own representation.

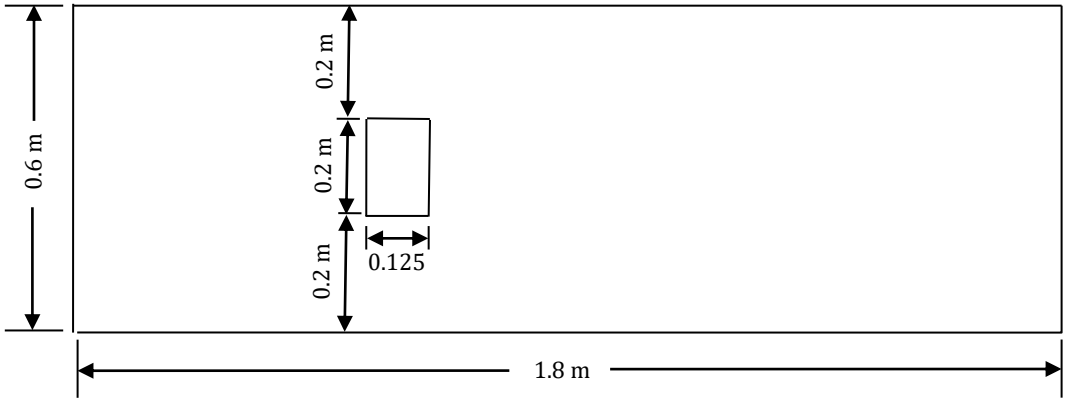

Figure-5.6. Geometry of computational domain for M-0 at top view approach. Source: own representation.

5.4.3. Selection of the boundary condition

The aim of this research is to simulate wind tunnel simulation in numerical domain. For exact modelling of the wind tunnel domain, similar wall impact present in the wind tunnel has to be simulated in numerical domain. In order to do so, height of the computational domain remain same as the wind tunnel test section, which is in this case, 0.5 m. In reality, a real scale building would be 30 m in height where the neutral space above has no limit. But numerical domain has computational limitation. Flow above the model has an computational height of 0.35 m. The ceiling and lower surface acts as a no slip wall with the inlet plane at the right and outlet plane at left (**Figure-5.7**).

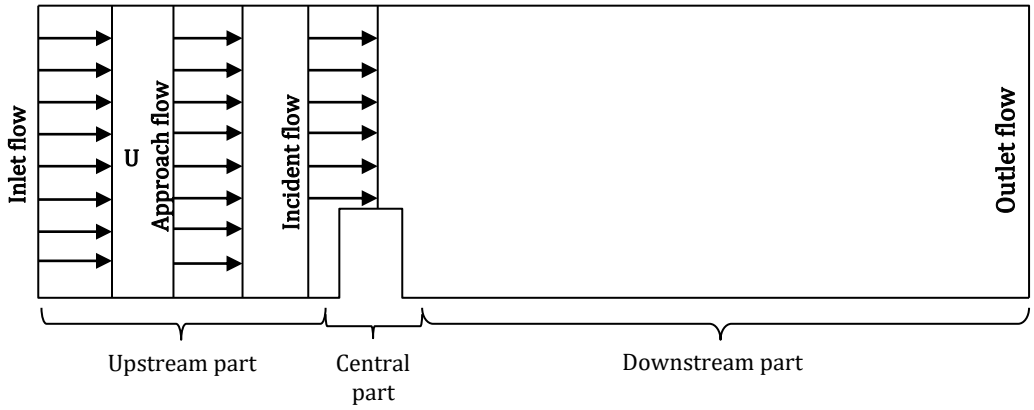

Figure-5.7. Flow and indication at different parts in the computational domain for numerical simulation (Side view approach). Source: own representation.

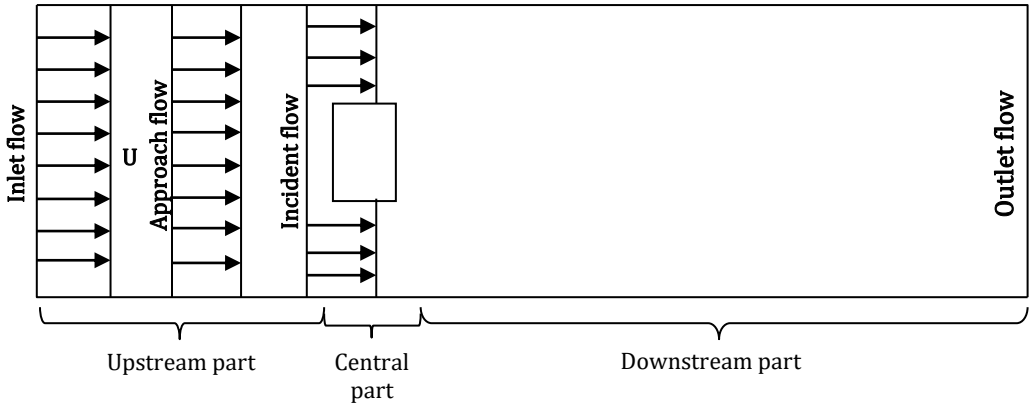

Figure-5.8. Flow and indication at different parts in the computational domain for numerical simulation (Top view approach). Source: own representation.

5.4.4. Selection of the boundary condition

The computational domain usually contains only a part of the urban or industrial area. Therefore the choice of the position of the boundaries of the computational domain influences the results. This influence definitely adds to the uncertainty of the simulation results but can also lead to errors if the choice is inadequate or inaccurate [51]. Similar boundary condition applied at the wind tunnel simulation was adopted in 2D numerical domain. But in reality, there is no limitation of two coordinate or 2D domain in the atmospheric flow. In this study, there is two different zones in the numerical domain, namely fluid zone and solid zone where no slip condition applies. There were also two kinds of inlet and outlet. Simulation for the models with duct has the constant velocity profile applied at the velocity inlet which is being influenced by the existence of the upstream wall of the model. There is also inlet at the upstream face of the models (models with duct) and outlet at the rear wall of the model. Lower surface and the ceiling has a criteria of solid wall. Model surfaces also have the criteria as solid wall where flow velocity is considered as zero i.e. these walls are used to define the boundary of fluid and solid. No fluid flow is present at the walls. There is no slip condition at all solid walls in the domain. Outlet was set as pressure outlet with zero pressure gradient [47]. From **Figure-5.9** and **5.10** Numerical domain for M-1 simulation, fluid flow zone is represented with ash coloured surface and solid walls with black.

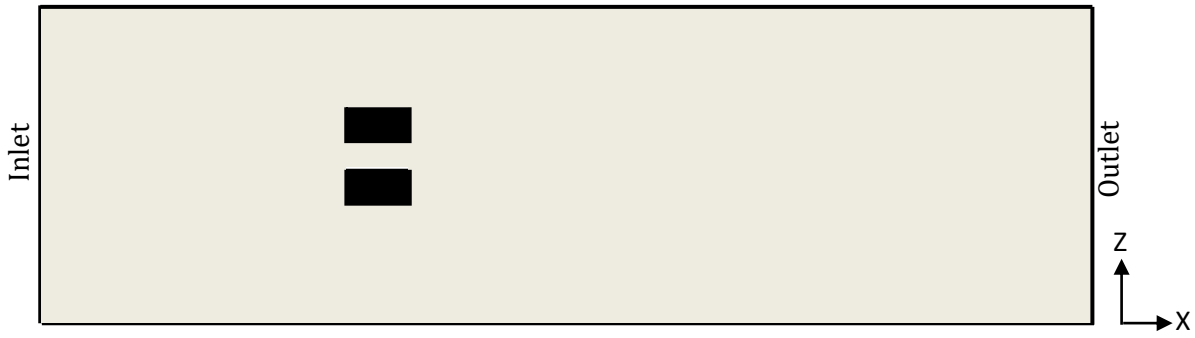

Figure-5.9. Fluid zone and solid walls at the numerical domain for M-1 side view (top)and top view (Bottom). Source: own representation.

5.4.5. Discretization

It is relevant to quote from Hirsch , "Grid generation and grid quality are essential elements of the whole discretization process. Not only is grid generation today a most critical element in the cost of running CFD simulations, but more importantly, the accuracy of the obtained numerical results is critically dependent on mesh quality" [43]. In this study, flow field is discretized in certain number of control volumes (Continuum space) which is then solved for the equations following numerical iterations in finite volume method (FVM). The characteristics of this method is that solution is represented in cell averaged values. Discretization of the integral form of the equations are applied to the continuum space which is comparatively simple then other numerical methods [47]. It is often possible to apply this method using arbitrary meshes i.e. FVM can accommodate any type of grid [42]. The FVM method uses the integral form of the conservation equations as its starting point [42]. The equation is as follows:

$$\int_S \rho\phi v.n\, dS = \int_S \Gamma\, grad\phi.n\, ds + \int_\Omega q_\phi\, d\Omega \qquad \text{[Eq-5.26]}$$

Where, ρ and v are the fluid properties (density and velocity), $\phi$is the rate of change of property within the control volume (control mass) S is the surface, $q_\phi$is the source or sink of ϕ and finally, ϕ is the unknown in the equation. $\rho\phi v.n$ and $\Gamma\, grad\phi.n$ are the convective and diffusive terms of flux vector in the direction normal to control volume respectively. "The solution domain is sub-divided into a finite number of small control volumes by a grid which defines the control volume boundaries. Then the conservation equation and the transport equations are applied to each CV. At the centre of the each node lies a computational node at which the variable values are calculated. Interpolation is used to express variable values at the CV surface in terms of the nodal values. Surface and volume integrals are aaproximated using suitable quadrature formulae. As a result one obtains an algebraic equation for each CV, in which a number of neighbour nodal values appear" [42]. Types of control volume used in this project is generated with ANSYS meshing where unstructured grid was used. Unstructured grid is a type of grid with irregular topology. Number of nodes and elements used for numerical simulation for different

models are given in the Table-5.1. In this experiment, quadrilateral cells were used for all numerical simulation (**Figure-5.10**). To validate the quality of meshing skewness factor between 0.88-0.95 were maintained for all grid generation [46] and [47].

Model number	Approach			
	Side view		Top view	
	Nodes	Elements	Nodes	Elements
Model-0	458162	225147	315364	154595
Model-1	458161	225147	-	
Model-2	459058	225515	-	
Model-3	-		511131	251167
Model-4	512332	252278	-	

Table-5.1. Number of nodes and elements used for numerical simulation in this experiment. Source: own representation.

Figure-5.10. Quadrilateral grid used for 2D grid generation. Source: based on [42]

Considering the errors and uncertainty it is very relevant to quote from Versteeg and Malalasekera that, “The consequences of inaccurate CFD results are at best wasted time, money and efforts, and at worst catastrophic failure of components, structures or machines” [44]. Presence of error and uncertainties in numerical simulation is a very usual phenomena which can us lead to erroneous result and futile effort. Error is defined as a recognizable deficiency in a CFD model that is not caused by the lack of knowledge. Different errors present in the CFD can be classified into three broad categories namely numerical errors, coding errors and user errors. Numerical error comprised of round off errors, convergence error and discretization errors. Coding error is caused due to the presence of bugs or malware present in the software and finally the user errors are caused from human errors due to the incorrect use of the software.

Uncertainty is defined as a potential deficiency in a CFD model that is caused by lack of knowledge. Main sources of uncertainty are input uncertainty and physical model uncertainty. Input uncertainty is defined as inaccuracies due to limited information or approximate

representation of geometry, boundary conditions, etc [44]. On the other hand, physical model uncertainty can be defined as discrepancies between real flows and CFD due to inadequate representation of physical processes (e.g. turbulence) or due to simplifying assumptions in the modelling process (e.g. steady flow) [44].

In this study, error and uncertainties were taken into consideration and to reduce the errors and uncertainties in modelling and approximating the flow field, best practice guidelines in urban aerodynamics were followed according to [45];[47] and [51].

5.5. Simulation

5.5.1. Initialization of the flow field

After setting the above mentioned accordingly, the mesh is ready for the solver calculation, which is in our case ANSYS Fluent. Fluid parameter was set as air with a density ρ=1.225 kg/m^3 and viscosity μ=1.7894E-5 kg/ms. Boundary condition set for the domain is shown in the Table-5.2.

Inlet	
Reference frame	Absolute
Velocity magnitude	5 m/s
Initial gauge pressure	0 Pa
Turbulence	
Specification method	k-ω
Turbulent kinetic energy (k)	0.047198 m^2/s^2
Specific dissipation rate (ω)	11.3 s^{-1}

Outlet	
Gauge pressure	0 Pa
Backflow direction specification method	Normal to boundary
Turbulence	
Model used	k-ω
Specification method	Intensity and viscosity ratio
Backflow turbulent intensity(%)	0.035
Backflow turbulent viscosity ratio	5

Solution method	
Pressure velocity coupling scheme	Simple
Special discretization	
Gradient	Least square cell based
Pressure	Second order
Momentum	Second order upwind
Turbulent kinetic energy	First order upwind
Specific dissipation rate	First order upwind

Monitors	
Convergence absolute criteria	
Continuity	10^{-6}
x-velocity	10^{-6}
y-velocity	10^{-6}
Turbulent kinetic energy (k)	10^{-6}
Specific dissipation rate (ω)	10^{-6}

Solve/Initialize	
Compute from	Inlet

Solve/Iterate	
Number of iteration	6000

Table-5.2. Solver settings for ANSYS Fluent. Source own representation.

5.5.2. Selection of numerical approximations

There are several turbulence parameters to be calculated before any numerical simulation to define boundary conditions when using a turbulence model for simulation (In this experiment k-ω SST turbulence model). The parameters to specify their values at different boundaries are

turbulent kinetic energy (k), specific dissipation rate (ω), turbulent intensity (TI), turbulent viscosity ratio. This is often difficult and a source of uncertainty since the incoming turbulence is rarely known exactly. Reynolds number (Re) for the flow is same as the wind tunnel flow which was calculated as Re ≈ $1.8 \cdot 10^5$ (Chapter-4, Section-4.5). Re no was used to calculate Turbulence intensity (I) at the inlet. Turbulence intensity (I) can be calculated from the equation below [54].

Turbulence intensity, $TI = 0 \cdot 16(Re)^{-1/8}$=0.035 % [Eq-5.27]

Using the value of *TI* obtained from **Equation-5.27**, Turbulent kinetic energy (k) can be computed from the Equation-5.28 below [53].

$k=\frac{3}{2}(\bar{u}\, I)^2$ =0.047198 m^2/s^2 [Eq-5.28]

Where, mean flow velocity, $\bar{u}$ =5 m/s, Inlet boundary layer thickness ($\bar{\delta}$) is necessary to determine the inlet specific dissipation rate (ω), boundary layer thickness ($\bar{\delta}$) at inlet surface is calculated from the **Equation-5.29**, which is as follows [54]:

$\frac{\bar{\delta}}{L} \approx \frac{1}{\sqrt{Re}}$ [Eq-5.29]

$\bar{\delta}$ = $4.25 \cdot 10^{-3}$ m

Where, Characteristic stream wise length of the body direction, *L* =1.8 m (length of the domain).

The turbulence length scale (ℓ) is a physical quantity describing the size of the large energy-containing eddies in a turbulent flow. For wall bounded flow using fluent as a solver, Turbulence length scale (ℓ) is calculated from the following equation [55]:

ℓ = 0.07 D_H = 0.035 m [Eq-5.30]

Where, Hydraulic diameter of the domain, D_H = 0.5 m (height of the wind tunnel). Inlet specific dissipation rate (ω) for fluent can be obtained from the following Equation-5.31[56]:

$\omega = \frac{\sqrt{k}}{\ell C_\mu^{1/2}}$=11.3 s^{-1} [Eq-5.31]

The initialization of the flow field sets the turbulence parameters according to certain approximations from the calculated value, experience and best practice guidelines [49]. The accuracy of the numerical simulation depends greatly on the appropriate approximation of these values [51][52].

5.5.3. Selection of the convergence criteria

In this experiment, the simulation started from the inlet. The monitor of residual values are mentioned in Table-5.2. This monitor setting is used to survey the calculating process. **Figure-5.11** shows the plot monitor of the residual for the calculation of the M-1, where residual values for continuity, x-velocity, y-velocity, k and ω is plotted against 6000 iterations.

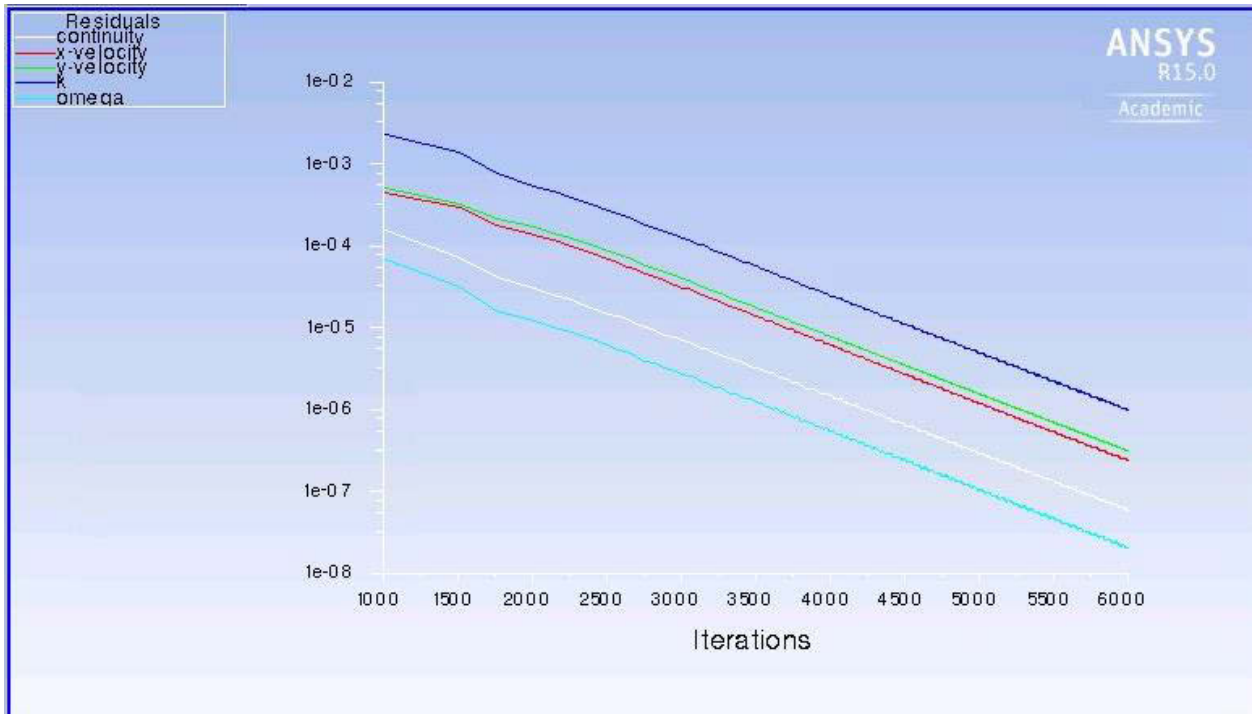

Figure-5.11. plot monitor of residual values (Simulation of M-1 side view). Source: own representation.

5.6. Post processing

5.6.1. Visualizing and analyzing data

Aerodynamic flow profile applied to the inlet of the CFD domain is quite similar to the velocity profile applied to the wind tunnel measurements. Mean velocity profile applied at wind tunnel test section and CFD domain from the surface of the domain till the model height can be apprehended from the **Figure-5.12** and **Figure-5.13** respectively. The deviation of the mean velocity profile at CFD domain and the wind tunnel measurement is negligible.

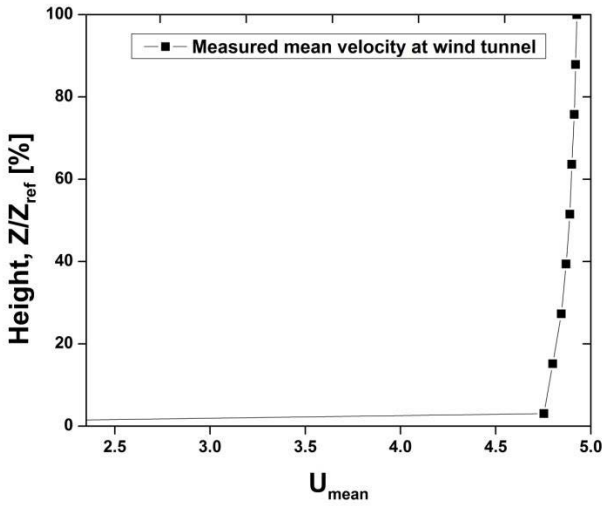

Figure-5.12 Mean velocity profile at wind tunnel. Source: own representation.

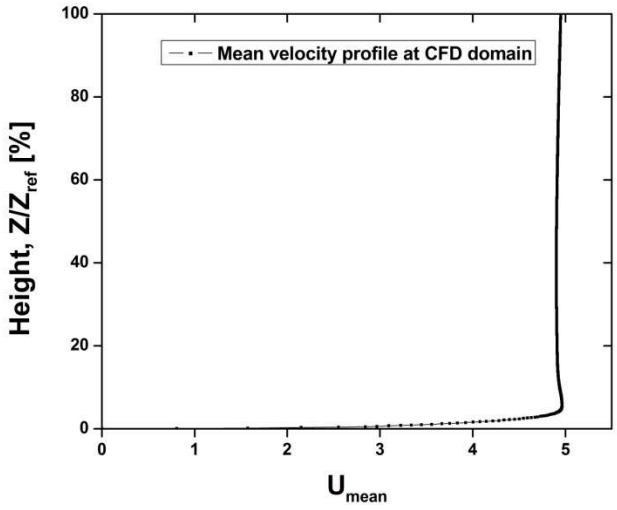

Figure-5.13 Mean velocity profile at CFD domain. Source: own representation.

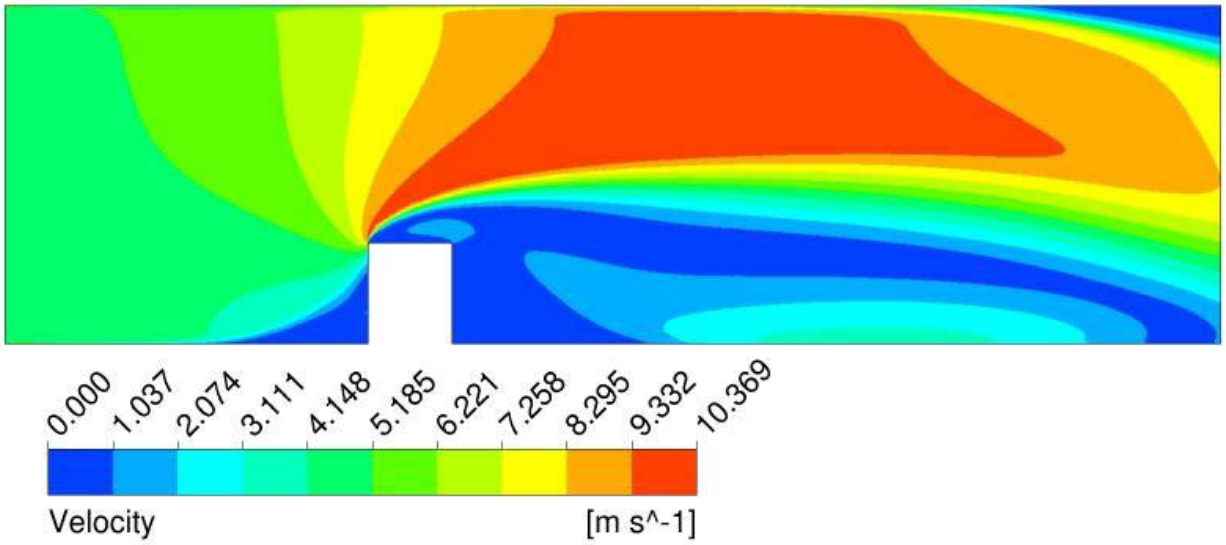

Figure-5.14. Velocity contour plot for M-0 in side view. Source: own representation.

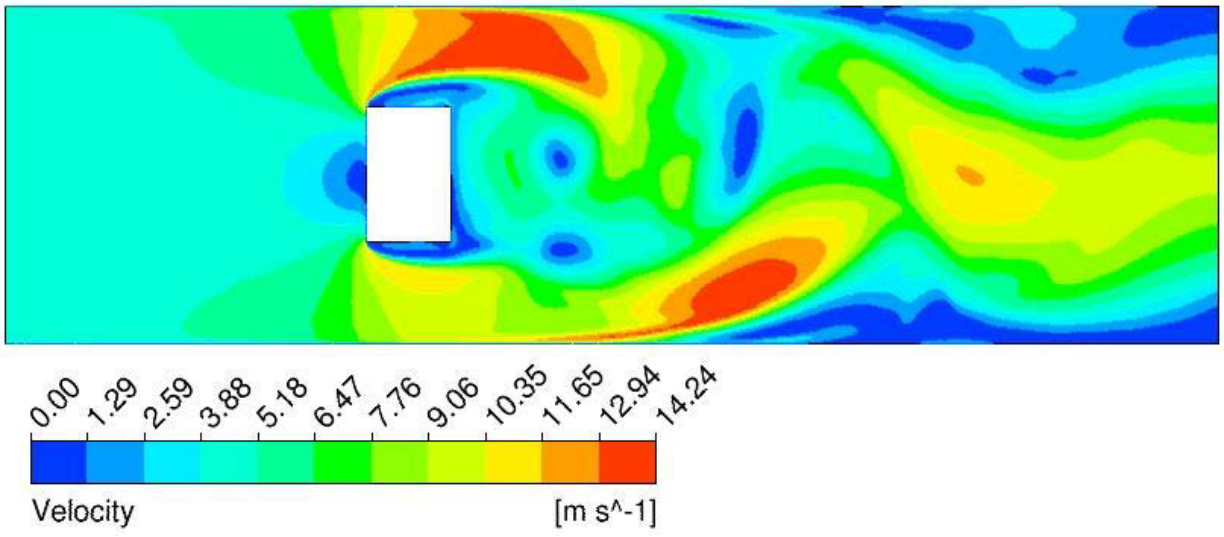

Figure-5.15. Velocity contour plot for M-0 in top view. Source: own representation.

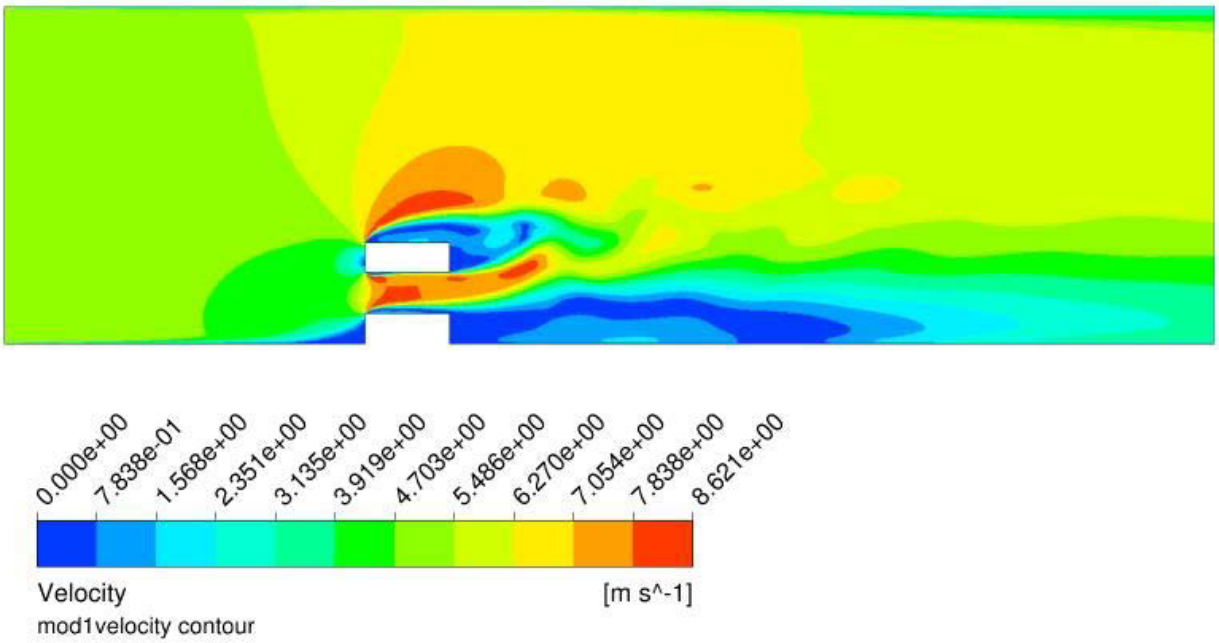

Figure-5.16. Velocity contour plot for M-1 in side view. Source: own representation.

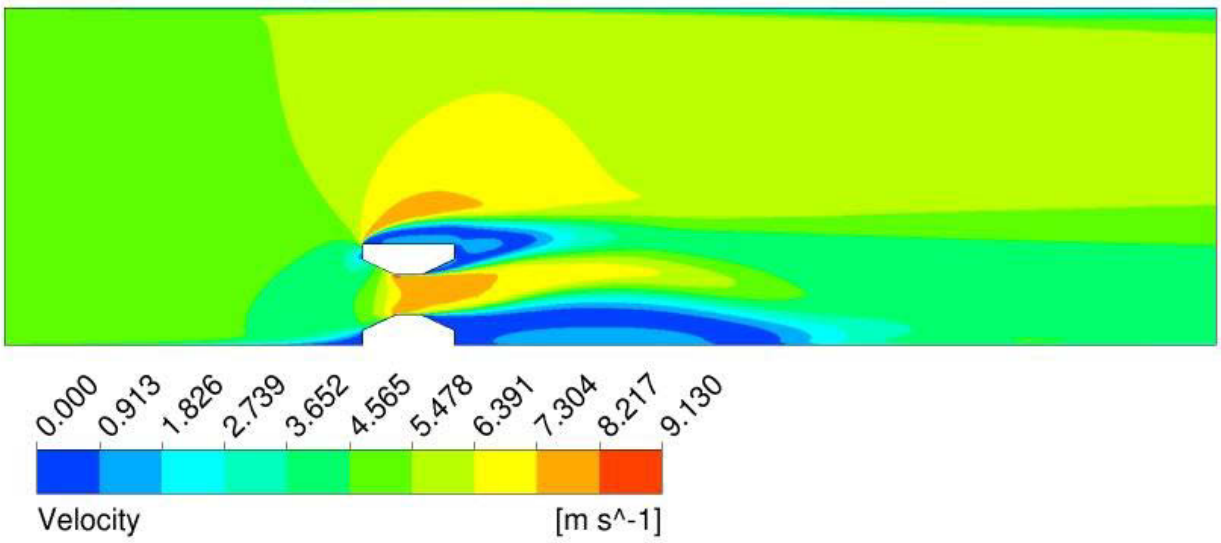

Figure-5.17. Velocity contour plot for M-2 in side view. Source: own representation.

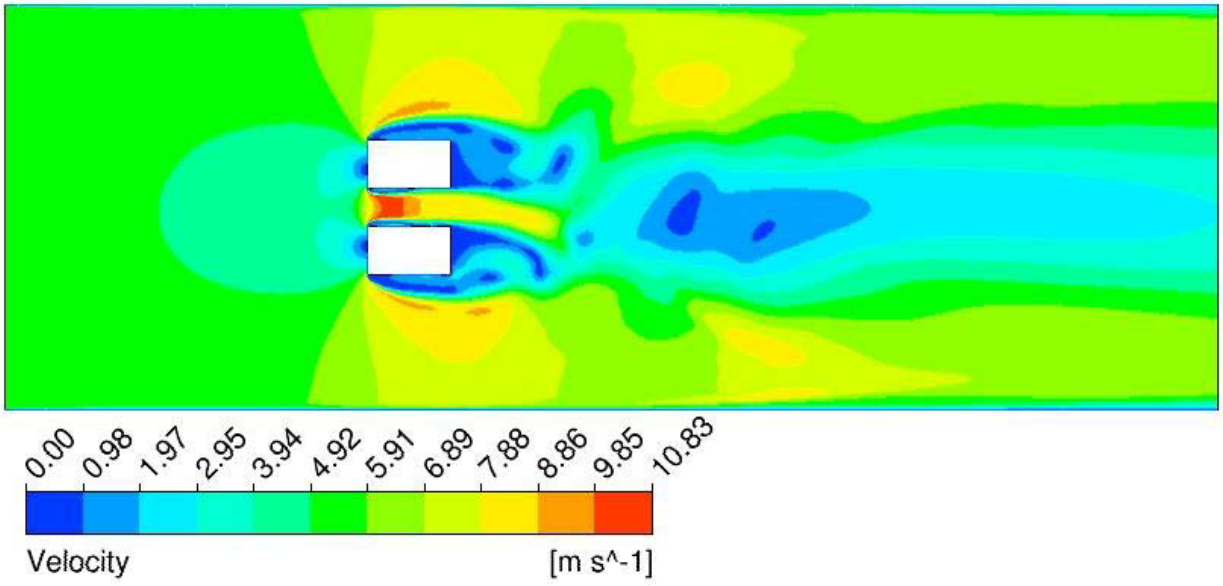

Figure-5.18. Velocity contour plot for M-3 in top view. Source: own representation.

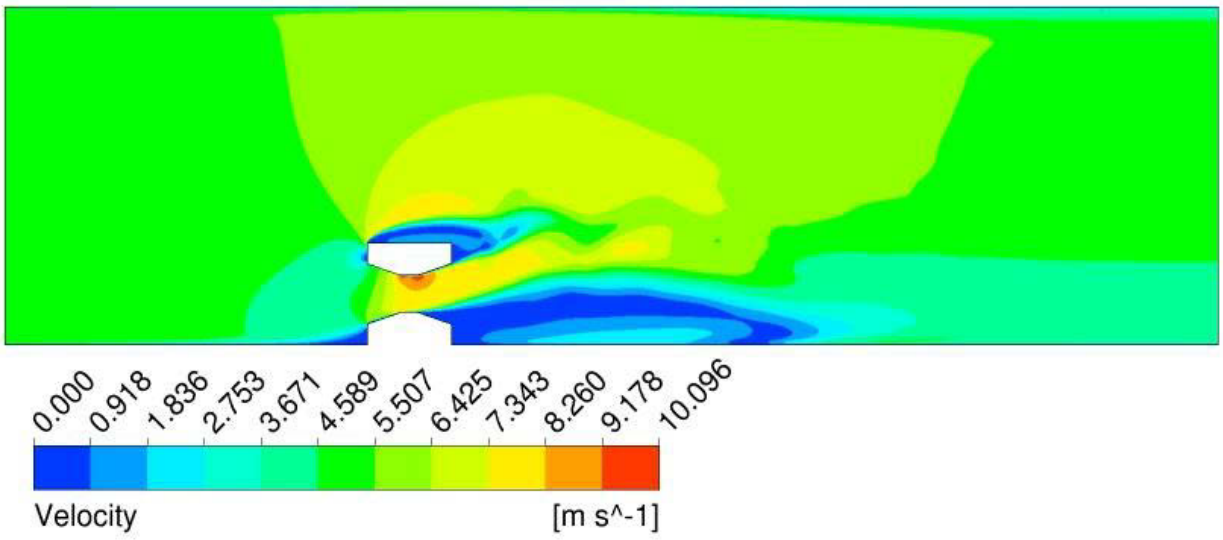

Figure-5.19. Velocity contour plot for M-4 in side view. Source: own representation.

Velocity contour plot represent the time-averaged velocity of the whole computational domain. It can reveal various data as velocity difference at various locations of the duct and around the models. Previously described in the Section-5.3.1.2, the computational domain represent the complete test section of the wind tunnel simulation. The model in the domain emulate the building model. The time averaged mean velocity is represented by different colour scheme. Target variable for this experiment is velocity (Section-5.3.1.1). All ducts of each model has an orientation of 0˚ angle of attack (AOA) with the incident flow. The influence of the duct geometry to obtain the maximum mean velocity at the duct is explicitly visible from these contour plots. M-1, M-2, M-3 and M-4 has the maximum velocity obtained at the duct 8.62 m/s, 8.21 m/s, 10.83 m/s and 8.20 m/s (**Figures-5.16, 5.17, 5.18** and **5.19**). It can be concluded that incident flow at 5 m/s and at 0˚ AOA, Model-3 has the most efficient duct geometry with $3.025 \cdot 10^{-3}$ m^2 duct area (Chapter-4, Section-4.5) obtaining maximum velocity in the duct.

5.6.2. Verification and validation

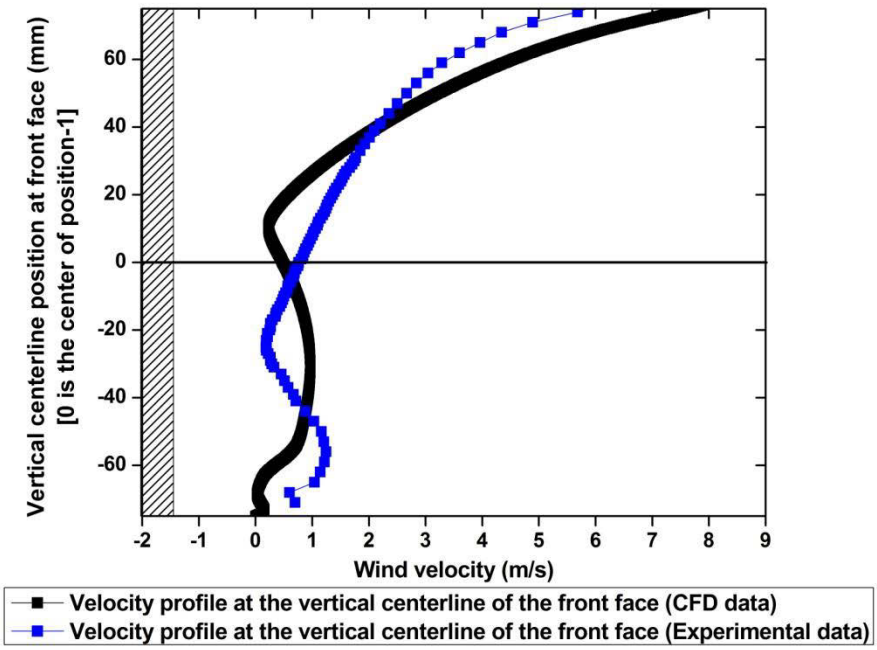

Figure-5.20. Comparison between velocity profile at upstream location-1 of M-0 from wind tunnel data and CFD data. Source: own representation.

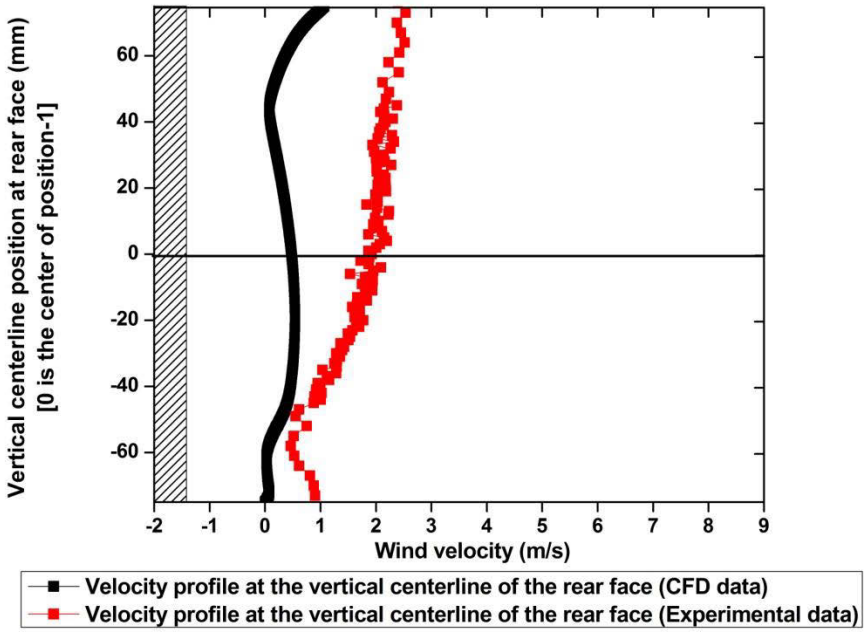

Figure-5.21. Comparison between velocity profile at downstream location-1 of M-0 from wind tunnel data and CFD data. Source: own representation.

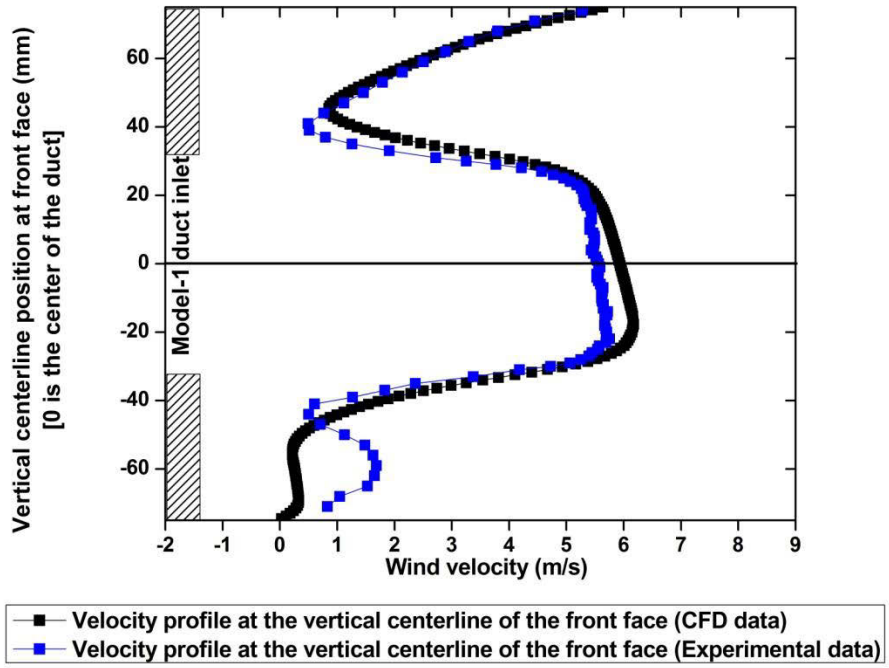

Figure-5.22. Comparison between velocity profile at upstream location-1 of M-1 from wind tunnel data and CFD data. Source: own representation.

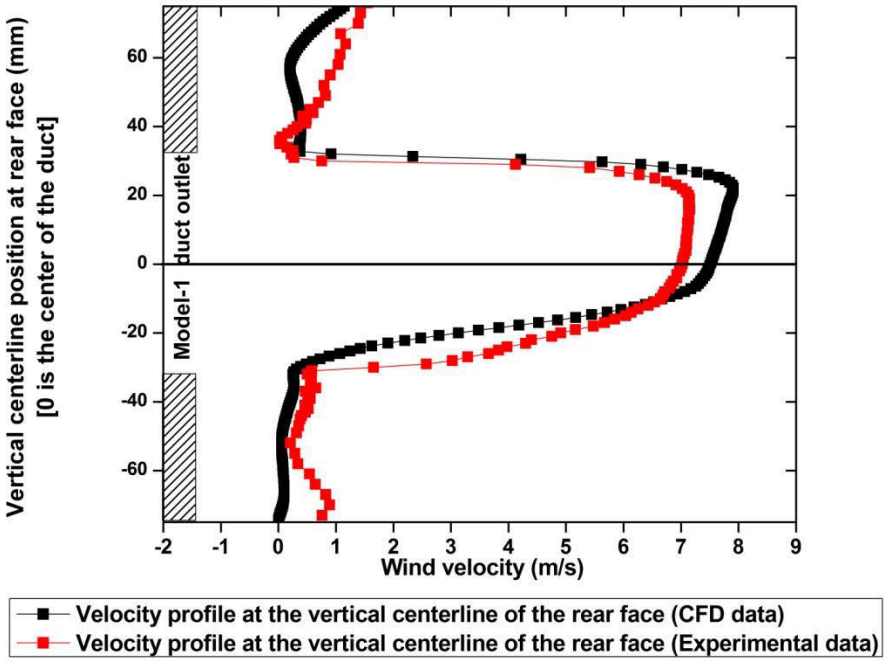

Figure-5.23. Comparison between velocity profile at downstream location-1 of M-1 from wind tunnel data and CFD data. Source: own representation.

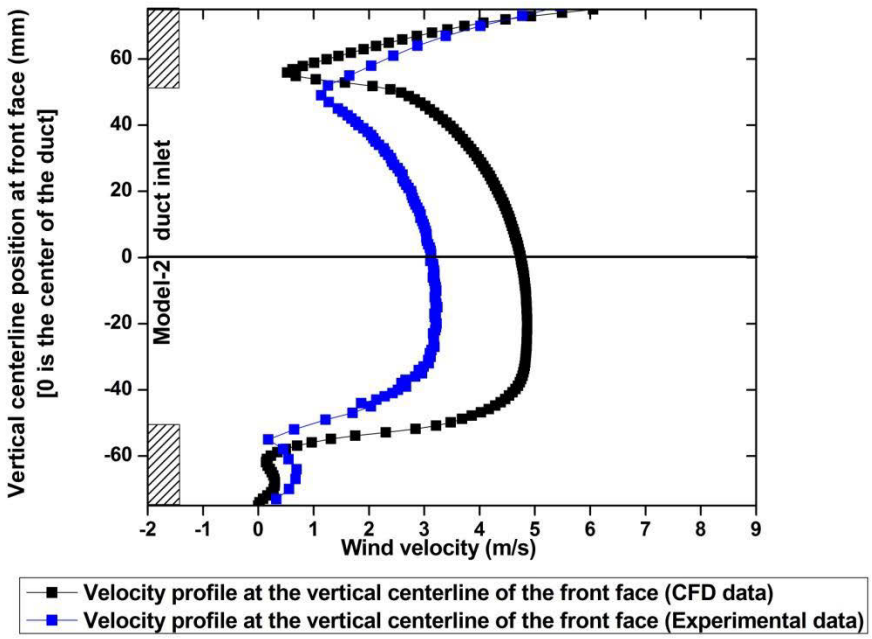

Figure-5.24. Comparison between velocity profile at upstream location-1 of M-2 from wind tunnel data and CFD data. Source: own representation.

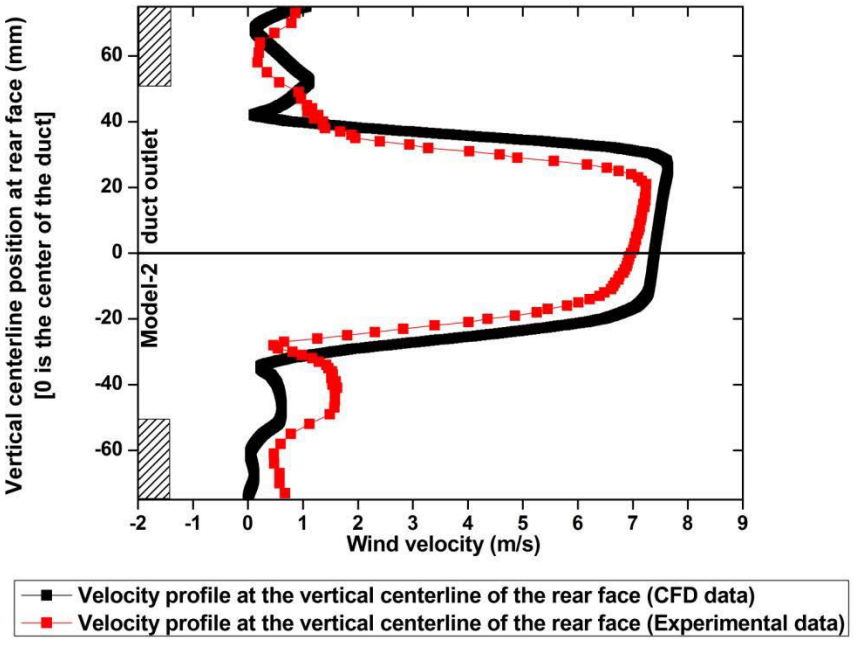

Figure-5.25. Comparison between velocity profile at downstream location-1 of M-2 from wind tunnel data and CFD data. Source: own representation.

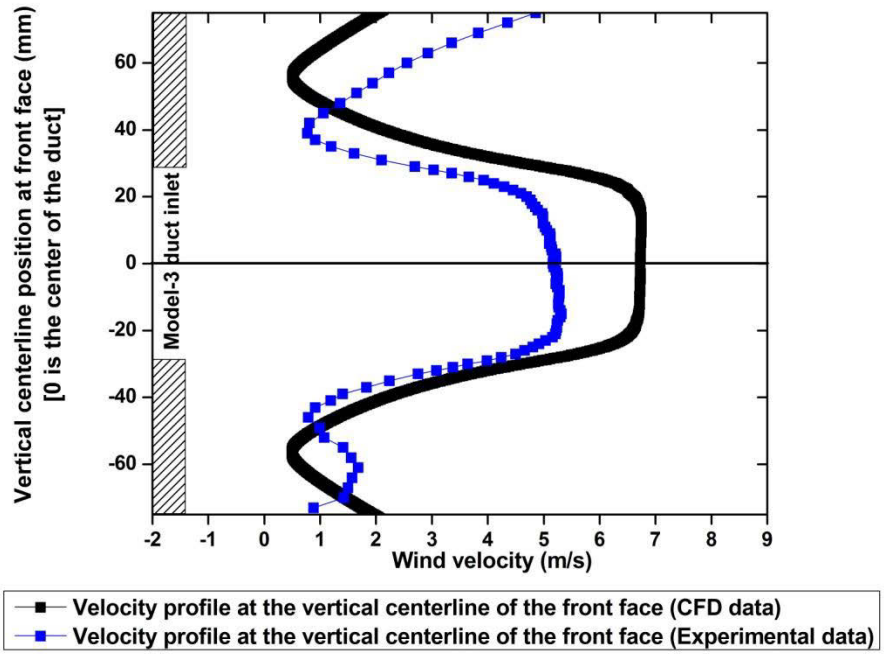

Figure-5.26. Comparison between velocity profile at upstream location-1 of M-3 from wind tunnel data and CFD data. Source: own representation.

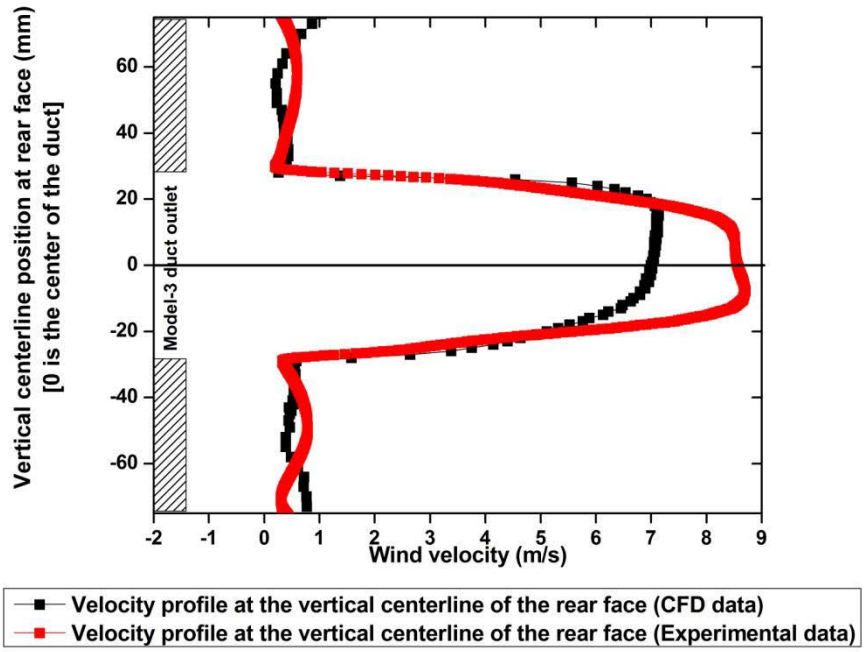

Figure-5.27. Comparison between velocity profile at downstream location-1 of M-2 from wind tunnel data and CFD data. Source: own representation.

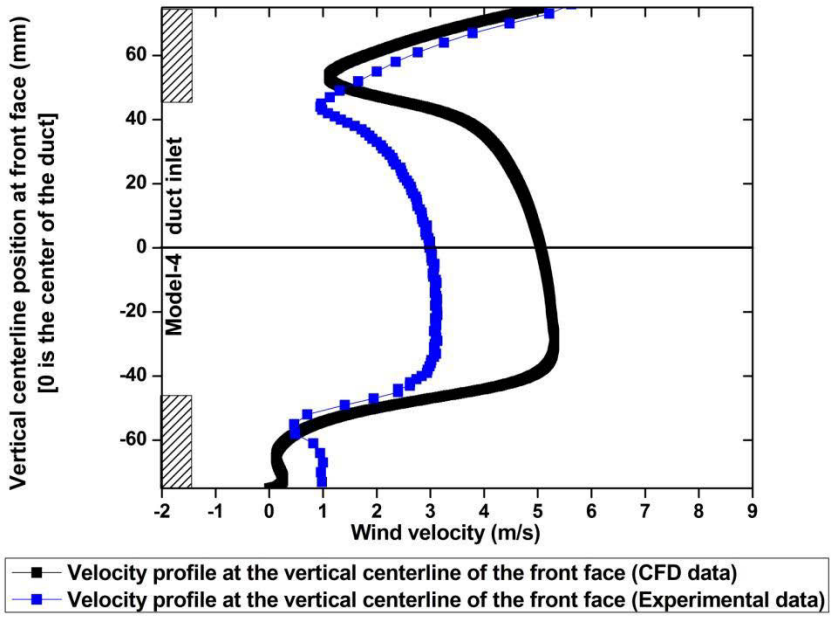

Figure-5.28. Comparison between velocity profile at upstream location-1 of M-4 from wind tunnel data and CFD data. Source: own representation.

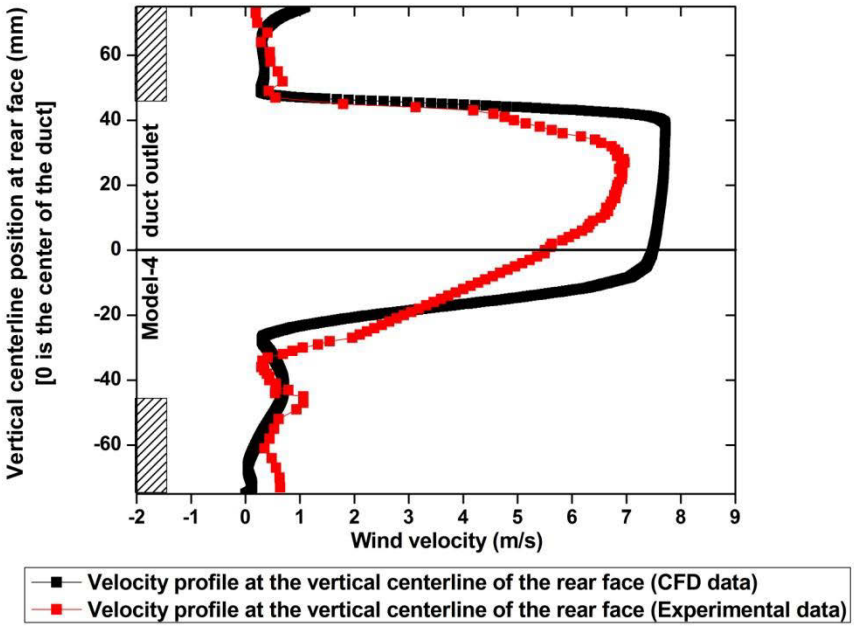

Figure-5.29. Comparison between velocity profile at downstream location-1 of M-4 from wind tunnel data and CFD data. Source: own representation.

Model	Location	Max Velocity, U_{max} [m/s]	Min Velocity, U_{min} [m/s]	Mean Velocity, U_{mean} [m/s]
M-1	inlet	7.91	0.12	4.95
	outlet	8.10	3.1	5.7
M-2	inlet	4.93	1.75	3.1
	outlet	7.80	0.59	4.46
M-3	inlet	7.00	5.31	5.56
	outlet	8.80	1.08	7.03
M-4	inlet	5.30	2.07	3.62
	outlet	7.90	0.69	4.62

Table-5.3. Maximum, minimum and mean velocity obtained at the location-1 for M-1,2,3 and 4 (CFD data). Source: own representation.

It is an essential part of numerical simulation to validate the result with experimental values. Certainly, numerical simulation can provide a large amount of data at locations which is less expected to be obtained through experimental measurements. Building aerodynamics is a vast area where the experimental domain is quite large to be measured. On the other hand, with appropriate modelling of the computational domain and accurate verification of the data obtained from CFD simulation with experimental result is a common practice. Table-5.3 represent the value of maximum, minimum and mean velocity at the duct of M-1,2,3 and 4. This data is obtained at the location-1 (see Chapter-4, Section-4.6) from numerical simulation. Mean velocity was calculated following the **Equation-4.7**(see Chapter-4, Section-4.8). Mean velocity profile obtained from CFD data is quite identical with data obtained from wind tunnel experiment. Except M-0 profile at location-1and M-1 profile at upstream location-1, CFD has provide us with higher mean velocity values at location-1except the values of M-1. But in all cases, time averaged mean velocity profile follows a similar pattern with the experimental data.

6. Conclusion and Recommendation

This research was focused on the possibility to extract wind energy from existing building infrastructure and analyzing related aerodynamics. Within that focus, the aerodynamics of the flow around buildings and aerodynamics of the interaction of that flow in building integrated duct without the wind turbine were analysed. In this regard, existing rectangular building group of 30 m height was taken as a model (See Chapter-4, Section-4.3) and wind flow was characterized for the city of Cottbus. Recorded wind data in this region was analyzed to determine the flow pattern in terms of wind speed, wind direction and wind speed frequency. The existing research facility from the Brandenburg University of Technology (BTU) was used both for wind tunnel experiment and numerical simulation of the flow. Wind tunnel measurement was taken to determine the target variable e.g. wind velocity in limited locations around the model and numerical simulation has provided complete flow field data. Data from wind tunnel measurement was used to calculate the extractable wind energy from a specific flow (in this case 5 m/s and at zero degree angle of attack). Moreover, turbulence results for the locations were also represented. Later, accuracy of the numerical data was validated with the help of data obtained from wind tunnel measurement. Numerical modelling is a process where getting an accurate result is subjected to trial and error from the validation of the result. However, results and their application obtained from the experiment is discussed in the later part of this chapter including possible future development scope for wind tunnel measurement and CFD modelling. Present achievement from this thesis can be implemented for wind engineering for wind load, ventilation, pedestrian wind comfort and wind energy analysis.

6.1. Limitation of the building

Urban environment has several limitation for wind energy exploitation. Some of them are associated with noise emission, vibration and shadow flickering. Moreover, in reality, atmospheric boundary layer (ABL) flow in urban areas is highly turbulent then the typical wind energy site (e.g. plain land, water surface etc). Understanding of such flow in built terrain is subjected to more extensive measurement and analysis. Space constraint of the building integrated duct requires higher optimization then the open terrain wind analysis. However, building integrated ducts are easier to implement with the existing structure saving the cost of building expensive tower. Electricity generation at the user end can minimize transmission capacity problem. Considering the future possibilities of building integrated wind turbines, this thesis has given a basic outline of wind data calculation and measurement process. Most useful information for this thesis was found from the scientific sources concerning wind energy, wind engineering, meteorology and building aerodynamics. Achievement of this thesis is as follows.

6.2. Wind data analysis

In this study, wind data record for one year was used for wind data analysis. Ten minute and monthly average wind speed (**Figure-2.7** and **Figure-2.8**), wind speed frequency distribution (Weibull distribution, **Figure-2.12**), wind direction (Rose diagram, **Figure-2.13**) was obtained for this length of the data obtaining period mentioned (Chapter-2). Data record at 10 m height was converted to 30 m height using power law (**Equation-2.1**, Section-2.3.1). Power law with a coefficient (α) value of 0.14 is sufficient at the plain terrain wind assessment. Considering urban topography with a higher value of roughness class (in this case 3.488), log-law should be used to determine the converted wind speed as log-law formula keeps the roughness length **(**z_0) into consideration. Log-law of the atmospheric boundary layer can be expressed as **Equation-6.1**.

$$v_2\,(z_2) = v_1(z_1)\frac{\ln\frac{z_2}{z_0}}{\ln\frac{z_1}{z_0}} \qquad \text{[Eq-6.1]}$$

Where, $v_2\,(z_2)$ is the average wind velocity at z_2, $v_1(z_1)$is the reference velocity in reference height at $z_1$and $z_0$is the roughness length which is in this case 0.55 m (Section-2.4.1). Equation-6.1 should be used to convert the wind speed data to determine an accurate prediction of atmospheric boundary layer flow characteristics at the site (in case of sites located in the city of Cottbus). For further research in this field, a better prediction should be made in determining the historical wind data characteristics using a data record for longer period (> 5 years) and above mentioned corrections. Wind data analysis is tend to be more accurate as the length of the data recording period increases [13]. Additionally, new measurements in the wind tunnel is required with boundary layer profile. Validity of using log-law profile over power law for urban aerodynamics is possible to prove with further experimental analysis in ABL wind tunnel. Concerning fundamental research in building integrated wind energy, this analysis has provided the knowledge and guidelines for wind data modelling and site specification. Details of the wind tunnel flow profile will be discussed later in this chapter.

6.3. Wind tunnel measurement

There are three different possibilities to extract wind energy from building augmented flow e.g. wind turbines installed at roof and side walls of the building, accelerated wind flow between aerodynamically efficient buildings and building integrated duct. In this thesis third category was analyzed with different duct geometry (Chapter-4, Section-4.4). The measurement of the models has given a brief idea of velocity and turbulence intensity at inlet and outlet of duct. Based on the experimental result from wind tunnel measurement, M-2 duct geometry was found to provide maximum energy yield out of all five models. This elliptical wall duct has a very high energy yield (theoretical wind power) as much as 2.3261 W (Model scale 1:200) at a flow of 5 m/s velocity (Chapter-4, Section-4.10). However, M-3 has 61.5 % less area then M-2 but only 58.34 % less energy output then M-2. In reality, it would be close to impossible to build a wind concentrator duct like M-2 for real scale building. But considering optimized and realistic design

along with a proportionate energy yield, M-3 duct design is the best possible design out of all models experimented in this research for building integrated wind turbine (BIWT) purpose. However, determination of the duct design for wind energy concentration is a massive task of exhaustive experimental investigation. Several modification of the experimental approach is required for further investigation. Recommended development for wind tunnel measurement is discussed in Section-6.3.1 to Section-6.3.5.

6.3.1. Atmospheric boundary layer (ABL) flow

Measurement for this experiment was conducted in aerodynamic flow profile. It is possible to obtain a overview of the performance of the model but in reality applying ABL flow in the wind tunnel is essential for assessing accurate influence on the model. Thus, measurement from ABL flow in wind tunnel is unavoidable. For the present model scale (Chapter-4, Section-4.3), profile of ABL is represented in **Figure-6.1.** This figure illustrate the ABL profile according to power law and log-law. Vertical axis indicates the height above the ground in percentile, velocity data was calculated for 150 m above ground. As the target building group is 30 m high, ABL should be 5 times the height of the building [15]. Horizontal axis shows the velocity calculated for the reference velocity, $v_1(z_1) = v_1(15m) = 5\ m/s$ and at a roughness of $z_0 = 0.55\ m$. Duct centre at 15 m height should be considered as the effected reference velocity for the building groups of 30 m at present scale.

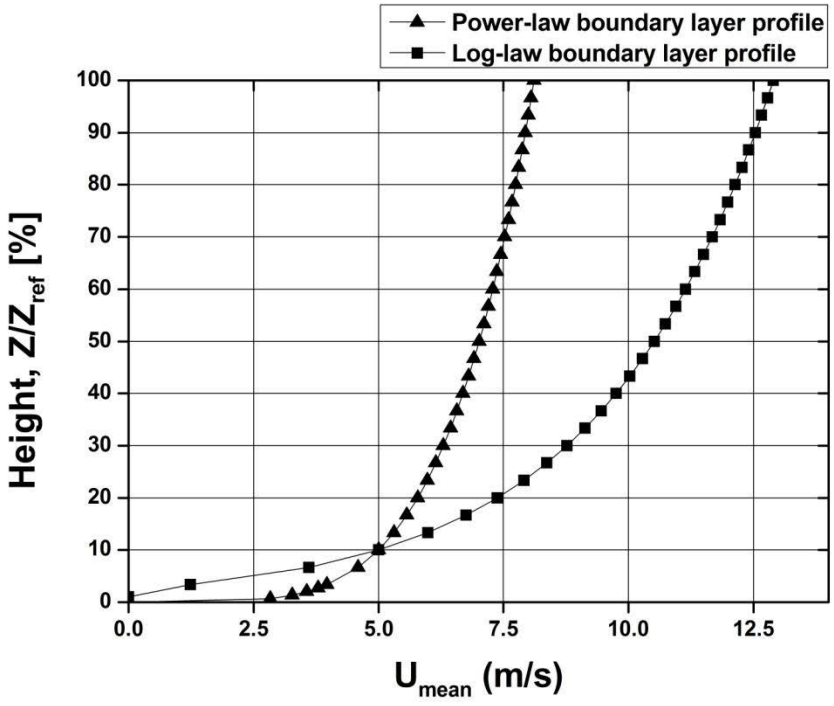

Figure-6.1. ABL profile for log-law and power law. Source: own representation.

To simulate the ABL flow from figure above, two possible recommendation is made. Similar model can be used to measure data in a ABL wind tunnel of minimum 0.75 m (test section

height) at present length scale ($\lambda_L = 1:200$). In another way, model scale can be reduced to lower values to use the same wind tunnel used for this experiment with certain modification to generate ABL flow (log-law). Modifications can be made with the help of turbulence grid, trip wall and roughness blocks to modify the aerodynamic flow to ABL flow. The turbulence grid is required to create turbulence similar in ABL and roughness block, trip wall is required to simulate ABL profile for certain roughness class. Finally, it is recommended to measure in log-law ABL profile as log-law equation (**Equation-6.1**) include the roughness length in calculation which is essential in generating urban ABL.

6.3.2. Site selection and model modification

Sites with low roughness class is preferred for exploring wind energy. Due to expansion of wind power capacity, low roughness sites are gradually decreasing. Sites of low roughness are preferred for wind turbines because of their high wind speeds and low turbulence level compared to sites with a high roughness. Most wind turbines are therefore found at sites with a low roughness. But the number of onshore sites with low roughness for wind energy decreases because of increasing population and wind turbines have already occupied consumable number of sites. For onshore sitting in the future, it is consequently unavoidable to look for sites with a higher roughness [58]. Apart from individual model measurement, it is necessary to adapt models of collective building groups to simulate accurate flow for a specific region and roughness class. In order to gather necessary information of different urban topography, scaled models can be used to measure. Examples of such topography can be industrial areas, high rise buildings, bridges, dikes and large building complex with possible wind concentrator effect. For building integrated duct, location of the duct centre, dimension and duct geometry can be modified. As an alternative, duct at the locations near the roof can be a very good opportunity using building augmented flow.

Blockage ratio is an important parameter in wind tunnel measurement. For measurements with ABL flow, it is better to keep the blockage ratio between 3-5% (Chapter-4, Section-4.3) [37]. It is advised to maintain the above mentioned blockage ratio while wind tunnel flow modelling to avoid the tunnel wall effect over the flow.

6.3.3. Measurement technique

Measurement technique used for building aerodynamics is very important. LDA measurement technique used in this experiment is only capable of measuring vertical and horizontal components of velocity respectively. Turbulence is an important parameter concerning research in building aerodynamics or ABL flow. For future measurement in this field, velocity components and related turbulence in three cartesian coordinate should be measured. Appropriate measurement technique for ABL and related turbulence, is Constant Temperature Anemometry (CTA) [49].

6.3.4. Measurement location

Duct is the centre of focus in analyzing models in this study. The accuracy of the measurement to determine the flow velocity inside ducts depends on the choice of measurement location. Non intrusive character of LDA was a possible option in assessing flow velocity at the inlet and outlet of the ducts, locations around models but measurement inside the duct is necessary to asses the exact location of the maximum velocity yield. Considering accuracy of the measurement, capability in measurement of velocity with three components and nature of the measurement location, future measurements can be obtained at the locations inside the duct with CTA technique. However, measurements from this thesis is also very useful to predict bluff body aerodynamics, incompressible ventilation, aerodynamic load calculation on buildings and to avoid wind hindrance on pedestrian level.

Augmented flow around the model and over the model roof has shown a very prospective opportunity to explore wind energy from roof mounted and wall mounted small wind turbines. From **Figure-4.43,** accelerated flow over the roof has possibility to extract wind turbine. The energy yield depends on the area of the turbine and wind speed distribution. At present this thesis has provided us with the accelerated flow velocity at 5 m/s incident flow, but an optimized positioning of the hub height range over the roof require additional velocity information at different applied wind velocity and angle of attack. From the analysis based on presently available data, the turbine can be installed at a hub height range of 14-20 m above the roof of the real scale building (30 m height). **Figure-4.16, 4.43** and **Figure-5.14** clearly indicates an accelerated velocity region ranges between 6.221-10.369 m/s with very low turbulence. Possible location of the wind turbine over the roof of the building is represented with **Figure-6.2**.

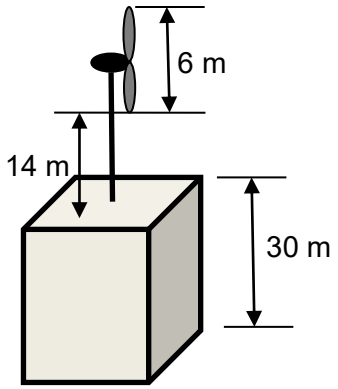

Figure-6.2. Possible roof mounted wind turbine location. Source own representation.

However, several researches has been concluded about the aerodynamic prospect of energy yield from roof top wind turbines [13][58]. But in reality residents of the building will be exposed to the negative impact of acoustic, vibration, yawed flow fatigue and shadow flickering of such

configuration. Moreover, urban building code has imposed limitation of the maximum building height for the specific region which can not be extended with roof top towers.

6.3.5. New building model

New building models with efficient aerodynamic exterior can be tested in wind tunnel with appropriate ABL flow (**Figure-1.4**). Contemporary researches have shown very good prospect of wind energy from aerodynamic building design [7][58]. Existing building complex sometimes have a very good wind concentration effect. Building models of such topography can be tested in wind tunnel to determine possible accelerated velocity and required calculation for wind energy yield. These kind of experiment is very effective for building designers and wind engineers to calculate wind load on the building, wind energy and pedestrian wind hindrance.

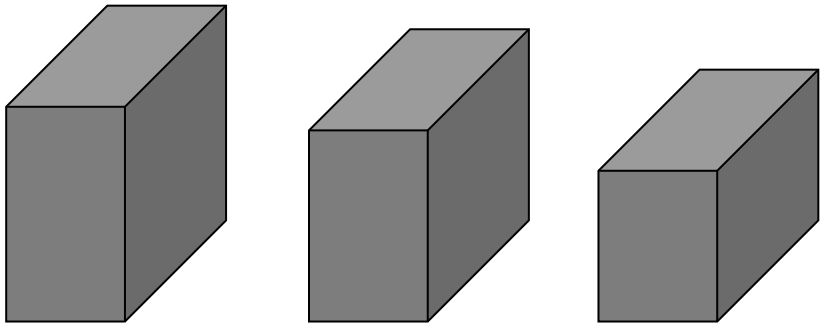

Figure-6.3. Designers view of building complex for future measurement. Source: own representation

6.4. CFD result

CFD simulation was used to acquire informations on locations where wind tunnel measurement will be a hectic task. The complete flow field data in terms of pressure, velocity and turbulence can be obtained. Objective of CFD in this regard was to numerically simulate the wind tunnel flow with similar flow profile. Validation of CFD data with wind tunnel measurement was represented in Chapter-5 (Section-5.6.1). Comparison between CFD data and wind tunnel measurement in terms of mean wind velocity is represented in **Figure-6.4**. Data represented in the **Figure-6.4** was measured for location-1 (Chapter-2, Section-4.6.1) using **Equation-4.8**. Difference of CFD data and wind tunnel data lies between 4.2-12.9 %. Recommendation to improve CFD modelling is discussed later in this chapter.

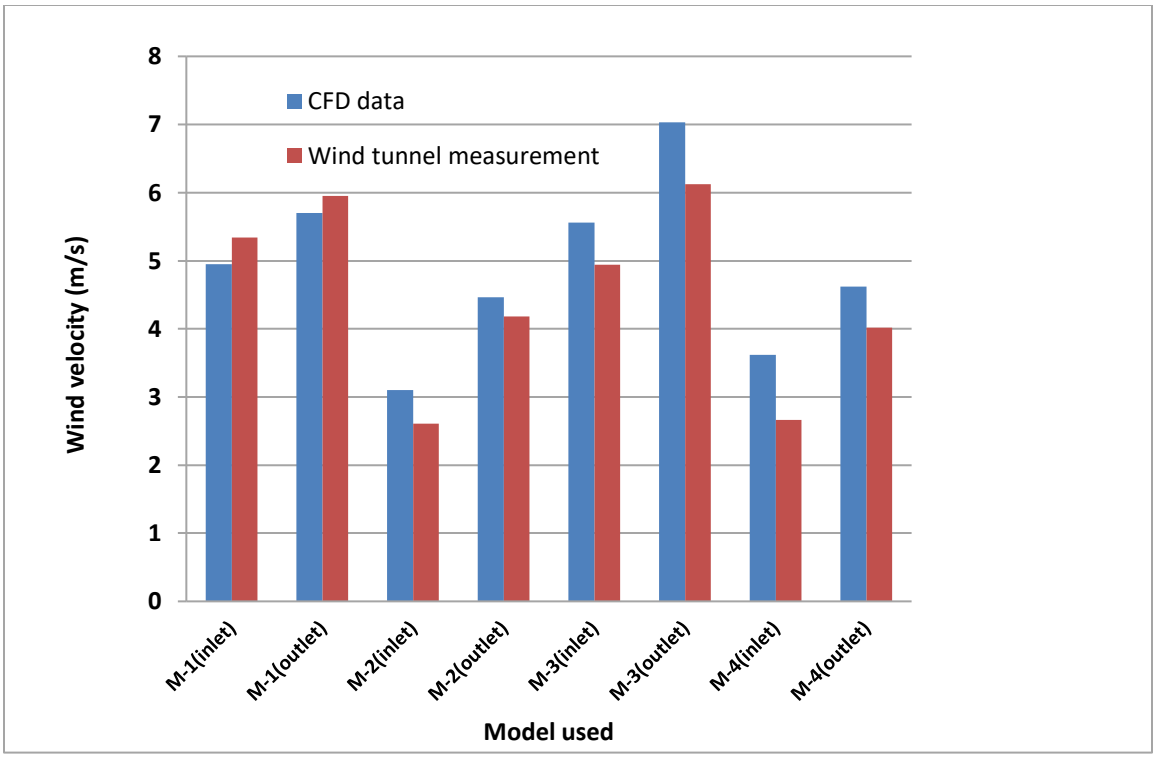

Figure-6.4. Comparison of mean wind velocity between CFD data and wind tunnel data.
Source: own representation

Model (Location-1)	CFD data Mean velocity (m/s)	Wind tunnel data Mean velocity (m/s)
M-1(inlet)	4.95	5.34
M-1(outlet)	5.7	5.95
M-2(inlet)	3.1	2.61
M-2(outlet)	4.46	4.18
M-3(inlet)	5.56	4.94
M-3(outlet)	7.03	6.12
M-4(inlet)	3.62	2.66
M-4(outlet)	4.62	4.02

Table-6.1. Comparison of mean velocity at duct from CFD and wind tunnel data.
Source: own representation

6.4.1. CFD domain

In this study 2D numerical domain was used (Chapter-5, Section-5.2). In 2D domain, the solver can only consider the vertical and horizontal component of the target variables. On the contrary, real scale ABL flow is a 3D phenomena. Results obtained in this experiment has very good accuracy when compared with wind tunnel data. This is because measurement technique used in LDA was also measuring the vertical and horizontal component of wind velocity. Similar to Section-6.3.4 (**Figure-6.2**), roof of the model has shown a very good prospect for possible wind turbine location. At 5 m/s of wind velocity, suitable wind turbine hub height is between 14-20 m height above the building with 30 m height (**Figure-6.5**).

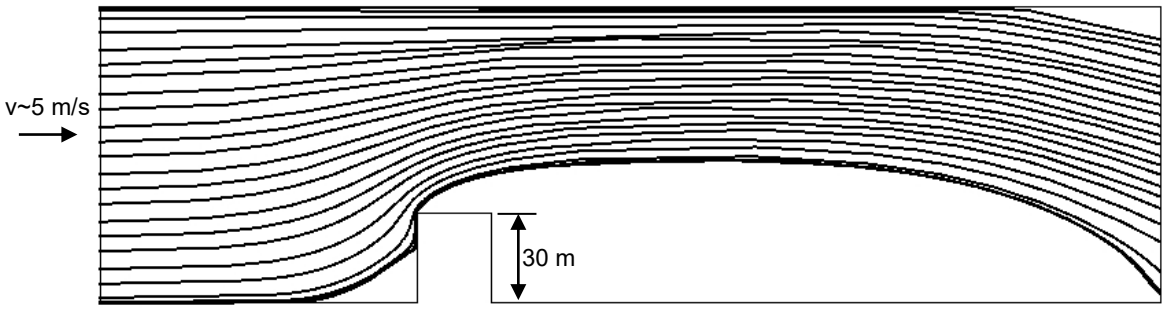

Figure-6.5. Flow streamlines in for M-0. Source: own representation.

6.4.2. CFD domain modification

Due to very high blockage ratio of the CFD domain, the influence of the domain ceiling over the flow can not be ignored. Accelerated flow is the result of insufficient domain height. Further analysis of the building aerodynamics with the help of CFD tool require 3D computational domain considering three Cartesian coordinate data of target variables. Domain settings require full scale flow modelling with appropriate dimension.

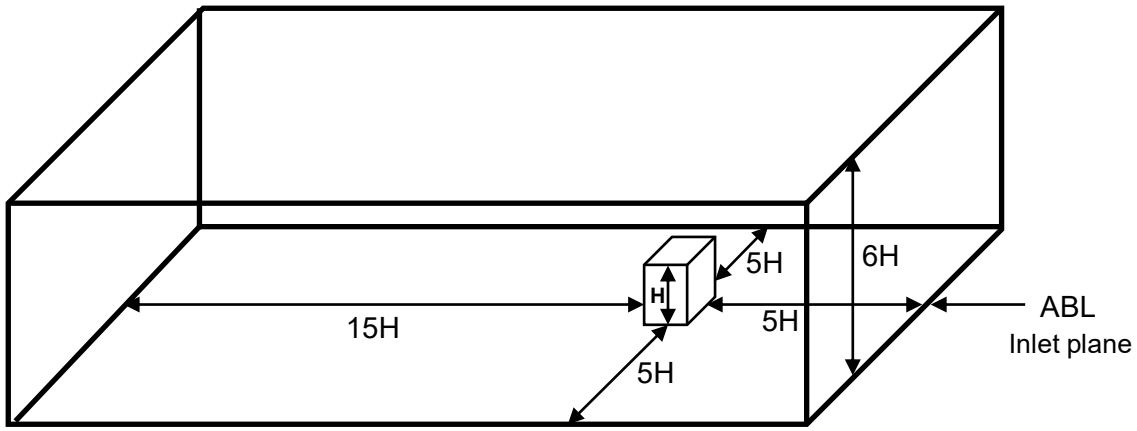

Figure-6.6. Computational domain of building aerodynamics. Source: based on [59].

Figure-6.6 represent the optimum dimension of CFD domain for ABL flow simulation [59]. This figure indicates the optimum distance of the domain boundary from the building model. Building height is expressed as H and comparative minimal distance from the building to the computational boundary is expressed relative to building height (H).

6.4.3. Directional blockage ratio

Directional blockage ratio is an important modelling factor in CFD modelling of buildings in ABL. Directional blockage ratio has two different scale to follow such as blockage ratio for length (BR_L) and blockage ratio for height (BL_H). These parameters can be defined as the ratio of building height or length to the domain height or length ($BR_H=H_{building}/H_{domain}$ and $BR_L=L_{building}/L_{domain}$) (**Figure-6.7**). According to best practice guideline for CFD modelling, value for both these ratio should be maintained below 17-22% [60].

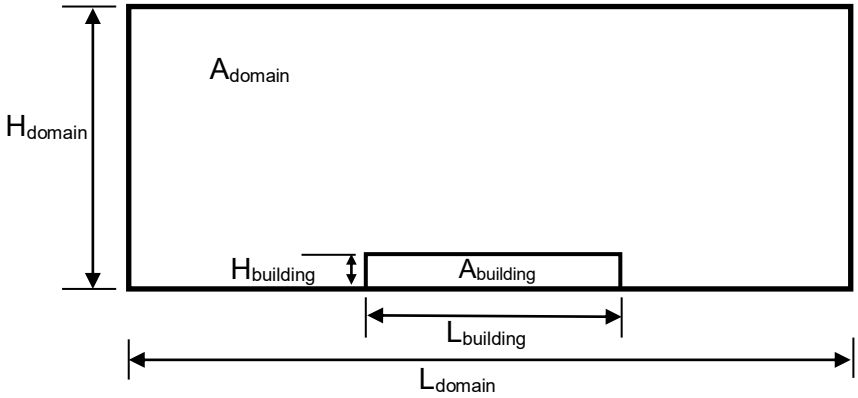

Figure-6.7. Directional blockage ratio. Source: based on [60]

6.4.4. ABL profile in CFD domain

Influence of the ABL flow on real scale building can be predicted with appropriate ABL flow modelling in CFD. At present model scale, ABL height should be 150 m for 30 m buildings. Log-law flow profile at different location of the computational domain is represented in **Figure-6.8.** Different phases of the ABL flow in different region of the domain is shown in different colour. Necessary input modification is required in solver physics to generate an accurate flow profile as represented in **Figure-6.1**.

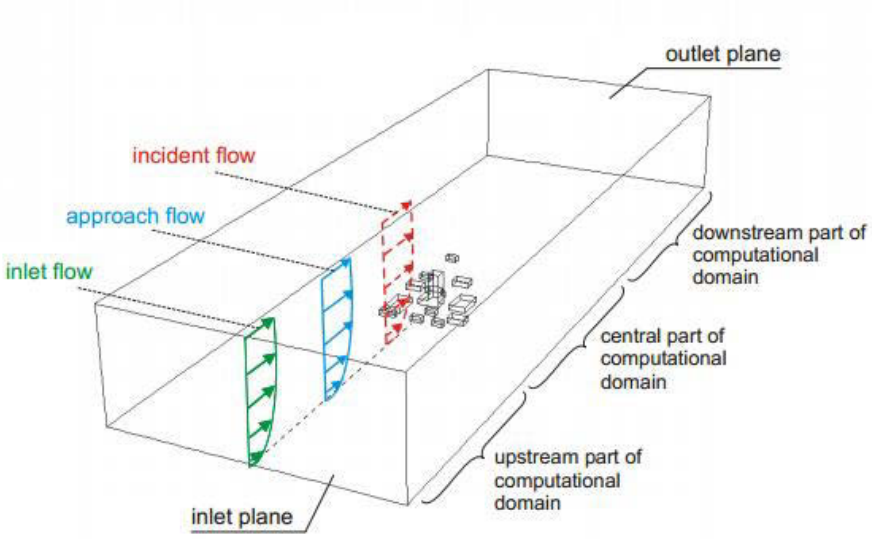

Figure-6.8. Computational domain with building models for CFD simulation of ABL flow: definition of inlet flow, approach flow and incident flow and indication of different parts in the domain for roughness modelling [61].

6.4.5. Actuator disc model

Extractable energy from the building integrated duct can be better predicted with the help of actuator disc modelling in numerical domain. The basic idea of the actuator method is to represent the influence of the flow in the duct for kinetic energy production, fluid as source terms in the governing Navier-Stokes equations [62]. As such energy calculation from the duct is much easier using actuator disc model for numerical analysis. In this regard application of the rotating mesh in the optimized wind turbine location inside the duct is required. The task to perform this method is to pre-calculate the axial and tangential induction as a function of radial position of the mesh, To calculate the forces as a function of radial position based on the induction and grid (rotating mesh) speed, To define the force containing domain in the solver using predefined step functions of the solver expression language and finally, to divide the total force at a given radial position by the corresponding rotor disc volume [62].

Wind energy from urban resources is a very promising research window. There is always scope to develop the existing experimental approach for better assessment in the future. Some of these aspects have been discussed in the former part of this chapter. This study has outlined an introductory experimental methodology with the expectation for an elaborate investigation for the later researchers.

References

[1] Moomaw, W., F. Yamba, M. Kamimoto, L. Maurice, J. Nyboer, K. Urama, T. Weir (2011). Introduction in IPCC special report on renewable energy sources and climate change mitigation [O. Edenhofer, R. Pichs-Madruga, Y. Sokona, K. Seyboth, P. Matschoss, S. Kadner, T. Zwickel, P. Eickemeier, G. Hansen, S. Schlömer, C.von Stechow (eds)], Cambridge University Press, Cambridge, United Kingdom and New York, NY, USA, p-04

[2] Mazur, K (2014): Nuclear power in Germany, www.world-nuclear.org, URL: http://www.world-nuclear.org/info/Country-Profiles/Countries-G-N/Germany/, (21.12.2014).

[3] Ender, C (2014). Wind energy use in Germany-Status 31.12.2013. in: DEWI MAGAZIN, Number-44, p. 37

[4] Dondi, P., Bayoumi, D., Haederli, C., Julian, D., Suter, M., (2002). Network integration of distributed power generation. Journal of Power Sources 106, pp. 1–9.

[5] Energy consumption from buildings (2014), German federal ministry for economic affairs and energy,URL:http://www.efficiency-from-germany.info/ENEFF/Navigation/EN/Energyefficiency/energyefficiency.html, (21.12.2014)

[6] Martens, S (2006). Wind energy in built environment. In: Multi-science, UK, ISBN 0906522358. p 28-60

[7] Cho, K, Jeong, S, Perwita Sari, D (2011). Harvesting wind energy from aerodynamic design for building integrated wind turbines. In: International Journal of Technology, vol-3: 189-198 ,ISSN 2086-9614, p 02.

[8] Cottbus, wikipedia.org, URL: http://en.wikipedia.org/wiki/Cottbus. (25.12.2014)

[9] Cottbus, dateandtime.com, URL:http://dateandtime.info/citycoordinates.php?id=2939811 (24.12.2014)

[10] https://www.google.de/maps/place/BTU+Cottbus+Lehrstuhl+Automatisierungstechnik/@51.6884621,15.4953136,6z/data=!4m3!3m2!1s0x0:0xcf43efb09cd2fbc8!4b1.

[11] Personal discussion with Dr-Ing Shaoqing Ying; CEBRA Research, Email: shaoqing.ying@tu-cottbus.de, (date: 15.05.2014)

[12] Allnoch,N (1993). WKA-Marktanalyse; Tendenzen und Entwicklungen. In: Tagungsband zum Kongreßprogramm der Husumer Windenergietage, p. 33 - 39.

[13] Wang, J (2013). Building integrated wind energy, Doctoral thesis, Faculty of Engineering and Physical science, University of Manchester. p.35-160

[14] Thomas C (2001). Integral turbulence characteristics and their parameterization, Diploma thesis, University of Bayreuth, Department of Micrometeorology, Bayreuth, p.101.

[15] Janet F. B (2014). Progress in observing and modelling urban boundary layer, Department of Meteorology, University of Reading, Earley Gate, PO Box 243, Reading RG6 6BB, UK, p.3-12

[16] Richards. P.J, Hoxey. R.P (1993). Appropriate boundary conditions for computational wind engineering models using the k-ε turbulence model; Journal of Wind Engineering and Industrial Aerodynamics 46&47; p.145-153;.

[17] Ote. T.R. (1978). Boundary layer Climates; Methuen Ltd.; p.372.

[18] ESDU 72026 (1972); Characteristics of wind velocity in the lower layer of the atmosphere near the ground: strong winds (neutral atmosphere); ESDU.

[19] Cooks. N.J (1985). The designers guide to wind loading of building structures, Butterworths, ISBN: 0408008709, 9780408008709.p.34-49
[20] Simiu, E, Scanlan, R.H, (1996). Wind effects on structures: Fundamentals and applications to design. 3rd Edition, John Wiley & Sons, New York, N.Y.p.9-17
[21] Beaufort scale, www.wikipedia.org, URL: http://en.wikipedia.org/wiki/Beaufort_scale, (11.12.2014)
[22] Beaufort scale, billboyheritagesurvey.wordpress.com, URL: https://billboyheritagesurvey.wordpress.com/2012/01/13/beaufort-scale/ (12.12.2014)
[23] Petersen T.I, E.L. (1989). European wind atlas; Riso National Laboratory, Roskilde, Denmark;; ISBN: 9780115155277. p.34
[24] Turbine wind class, www.vestas.com, URL: http://cvi.se/uploads/pdf/Master%20Literature/Wind%20Turbine%20Technology/Turbine_wind_class.pdf (19.07.2014)
[25] IEC wind turbine class, www.wind-works.org, URL: http://www.wind-works.org/cms/index.php?id=85&tx_ttnews%5Btt_news%5D=289&cHash=bfc12bcfc85c00e8d32a3f7efa725743
[26] Burton. T , Jenkins. N, Sharpe. D, Bossanyi. E. (2012); Wind Energy Handbook, 2nd Edition; ISBN: 978-0-470-69975-1. p.13-68
[27] Terrain roughness, www.middlebury.edu,
URL: http://cr.middlebury.edu/es/wind_group/terrain.htm (20.12.2014)
[28] Roughness and Wind Shear, www.windpower.org, URL: http://xn--drmstrre-64ad.dk/wp-content/wind/miller/windpower%20web/en/stat/unitsw.htm#roughness (22.09.2014)
[29] Perera. M.D (1981). Shelter behind two-dimensional solid and porous fences, And Industrial Aerodyn. 8, Wind engine, J. p.93-104.
[30] Taylor. P.A. and Teunissen. H.W. (1987). The Askervein Hill project: Overview and background data, Boundary layer Meteorol, 26, p.169-189.
[31] Weibull. W (1951). A statistical distribution function of wide applicability. J.Appl.Mesh, 18, p.293-297
[32] Weibull calculation, www.wind-data.ch, URL: http://wind-data.ch/tools/weibull.php (18.11.2014)
[33] Wind rose, www.windpower.com, URL: http://xn--drmstrre-64ad.dk/wp-content/wind/miller/windpower%20web/en/tour/wres/rose.htm (7.12.2014)
[34] Dantec Dynamics (2014): Measurement principle of LDA, www.dantecdynamics.com, URL: http://www.dantecdynamics.com/measurement-principles-of-lda (24.12.2014)
[35] Integrated solutions in laser Doppler anemometry (2014): www.dantecdynamics.com, URL: http://www.dantecdynamics.com/docs/products-and-services/general-literature/Laser_Doppler_Anemometry_318.pdf (24.12.2014)
[36] Windkanal Göttinger Bauart (2014), www.tu-cottbus.de, URL: https://www.tu-cottbus.de/einrichtungen/cftm2/dienstleistungen/messungen/windkanaele.html (21.06.2014)
[37] Holmes John, D. (2007). Wind Loading of Structures (2nd ed). New York, USA: Taylor and Francis; ISBN 0-203-96428.
[38] Plate, E.J., Cermak J.E. (1963). Micrometeorological Wind Tunnel Facilities: Description and Characteristics. Final Report, Contract No. DA-36-039-SC-80371 with U.S. Army Electronic Research and Development Activity, Fort Huachuca, Arizona, February 1963, CER63EJP-JEC9Characteristics of wind

velocity in the lower layer of the atmosphere near the ground: strong winds (Neutral atmosphere);ESDU,1972.
[39] Cermak, J.E (1977); Wind tunnel Testing of structures; Journal of Engineering mechanics division, ASCE, 103(6), pp 1125-1140.
[40] Stathopolous, T, Baniotopoulos, C.C (2007). Wind effect on buildings and design of wind sensitive structures; CISM courses and lectures,vol493, p.31-65,2007,DOI:10.1007/978-3-211-73076-8_2.
[41] John D. A. J (1995). Computational Fluid Dynamics, 2nd ed, McGraw-Hill education.
[42] Ferziger, J .H, Peric (1999), M. Computational Methods for fluid dynamics, 2nd edition, Springler.
[43] Hirsch, C, (2007). Numerical computation of internal & external flows. The fundamentals of computational fluid dynamics. Second Edition. Elsevier.
[44] Versteeg, H.K., Malalasekera, W, (2007). An introduction to computational fluid dynamics. The finite volume method. Second Edition. Prentice Hall.
[45] Roache, P.J., (1997). Quantification of uncertainty in computational fluid dynamics. Annu Rev Fluid Mech 29, p.123-160.
[46] Turbulence modelling (2012), Physics of shear-stress transport (SST) model, ANSYS fluent theory guide, ANSYS Inc.
[47] Blocken,B, (2014). Sports and building aerodynamics,Week-3,Lecture-5;www.cursera.com.
[48] Blocken, B, Stathopolous,T, Carmeliet, J, (2007); CFD simulation of the atmospheric boundary layer: wall function problems; Elsevier; Atmospheric Environment 41, p.238-252.
[49] Wang, J (2013). Building integrated wind energy, Doctoral thesis, Faculty of Engineering and Physical science, University of Manchester.
[50] Cebei. T, Cousteix. J (2005). Modelling and computation of boundary-layer flows: laminar, turbulent and transitional boundary layers in incompressible and compressible flows; Berlin: Springer, ISBN: 354024459X.
[51] Franke. J, Hellsten. A, Schuelzen. H, Carissimo. B (2007). Best practice guideline for the CFD simulation of flows in the urban environment, COST action 732.
[52] Shaughnessy Jr, E, Katz, I.M, Schaffer, J.P (2004). Introduction to fluid mechanics, Oxford press, ISBN: 9780195154511.
[53] Turbulent length scale, www.cfd-online.com, URL: http://www.cfd-online.com/Wiki/Turbulent_length_scale.(05.06.2014)
[54] Eddy viscosity ratio, www.cfd-online.com, URL:http://www.cfd-online.com/Wiki/Eddy_viscosity_ratio
[55] Turbulence length scale, www.cfd-online.com, URL: http://www.cfd-online.com/Wiki/Turbulence_length_scale. (05.06.2014)
[56] Hydraulic diameter, www.cfd-online.com, URL:http://www.cfd-online.com/Wiki/Hydraulic_diameter. (05.06.2014)
[57] Counihan. J (1975). Adiabatic atmospheric boundary layers: a review and analysis of data from the period 1880-1972. In: Atmos environ, 9, p.871-905.
[58] Martens. S (2006). Wind energy in the built environment: concentrator effects of buildings. In: Multi-science, 5, ISBN 0906522 35 8, p-149.
[59] Franke. J, Hirsch. C, Jensen. A.G, Krüs H.W, Schatzmann. M, Westbury. P, Miles. S.D, Wisse. J.A and Wright. N.G. Recommendations on the Use of CFD in Wind Engineering. In J.P.A.J van Beeck,

editor, Proceedings of the International Conference on Urban Wind Engineering and Building Aerodynamics: COST Action C14 - Impact of Wind and Storm on City Life and Built Environment, May 5 - 7, pages C.1.1 - C.1.11, Rhode-Saint-Genèse, Belgium, 2004. ISBN 2-930389-11-7.

[60] Blocken, B, Carmeliet J. 2004. Pedestrian wind environment around buildings: Literature review and practical examples. *Journal of Thermal Envelope and Building Science* 28(2): 107-159. p.12

[61] Blocken, B, Stathopoulos T, Carmeliet ,J (2007). CFD simulation of the Atmospheric Boundary Layer – wall function problems. Atmospheric Environment 41(2): 238-252. p.13

[62] Keck, R, E (2012). A numerical investigation of nacelle anemometry for a HAWT using actuator disc and line models in CFX, ScienceDirect, Renewable Energy 48 (2012) 72e84, p.4